Dipl.-Ing. Markus Bödenler, BSc

Nuclear Magnetic Relaxation Dispersion Contrast for MRI at 3T

DOCTORAL THESIS

to achieve the university degree of
Doktor der technischen Wissenschaften

submitted to

Graz University of Technology

Supervisor

Ao.Univ.-Prof. Dipl.-Ing. Dr.techn. Hermann Scharfetter
Institute of Medical Engineering

Graz, Austria, January 2020

Abstract

Molecular imaging plays a key role in answering clinical needs for personalized medicine. It gives insight into complex biochemical processes at the molecular and cellular level associated with a wide range of disease. While magnetic resonance imaging (MRI) is a renowned modality for clinical diagnosis based on anatomical and/or physiological images, molecular MRI is limited by moderate sensitivity. Thus, in certain cases, contrast agents are administered to enhance the MRI signal. Contrast agents with a strong magnetic field dependence, i.e. a strong nuclear magnetic relaxation dispersion, have been shown to be effective in generating target-specific contrast in MRI. The utilization of this relaxation dispersion requires the adaptation of an MRI scanner to allow for a modulation of the main magnetic field during the imaging sequence, also regarded to as fast field-cycling (FFC). This thesis is devoted to investigate, how to generate novel MRI contrast based on variations in the nuclear magnetic relaxation dispersion around a clinical field strength of 3 T. Such features would be otherwise hidden for conventional MRI. We report the first adaptation of a clinical 3 T MRI system for field-cycling. The presented FFC-MRI system is validated by means of dispersive contrast agents. It can potentially add value to the detection of various biomarkers, as is shown here for the specific case of zinc detection. Moreover, we introduce quadrupole relaxation enhancement as a mechanism of action for a fundamentally new class of reversibly activatable contrast agents with frequency-selective nuclear magnetic relaxation dispersion.

Keywords: molecular imaging, magnetic resonance imaging, fast field-cycling, nuclear magnetic relaxation dispersion, quadrupole relaxation enhancement, contrast agent

Kurzfassung

Die molekulare Bildgebung spielt eine Schlüsselrolle auf dem Weg hin zu einer personalisierten Medizin. Sie liefert Einblicke in komplexe biochemische Prozesse auf molekularer und zellulärer Ebene, die mit einem breiten Spektrum an Krankheiten korreliert sind. Die Magnetresonanztomographie (MRT) ist eine der führenden Bildgebungsmodalitäten in der klinischen Diagnostik, unter Einbezug von morphologischer Strukturen und/oder physiologischen Prozessen. Die molekulare MRT Diagnostik hingegen, ist durch ihre inhärent moderate Sensitivität limitiert. In bestimmten Fällen werden deswegen Kontrastmittel appliziert, um das MRT-Signal zu verstärken. Gewisse Kontrastmittel, mit einer starken Magnetfeldabhängigkeit der longitudinalen Relaxationsrate, auch bekannt als Relaxationsdispersion, haben sich bei der Erzeugung von zielgerichteten Bildkontrasten als wirksam erwiesen. Die Nutzung dieser Relaxationsdispersion erfordert die Adaption eines MRT-Systems, um eine Modulation des Hauptmagnetfeldes während der Pulssequenz, auch bekannt als fast field-cycling (FFC), zu ermöglichen. Diese Arbeit widmet sich der Untersuchung von neuartigen MRT-Kontrasten, basierend auf der Relaxationsdispersion im Bereich einer klinischen Feldstärke von 3 T. Solche Charakteristika würden sonst in der konventionellen MRT verborgen bleiben. Wir berichten über die weltweit erste Adaptierung eines klinischen 3 T MRT-Systems für field-cycling. Das vorgestellte FFC-MRT-System wird mit Hilfe von speziellen dispersiven Kontrastmitteln validiert. Solch ein System bietet großes Potential für die Detektion unterschiedlichster Biomarker, wie hier am speziellen Anwendungsfall der Zink-Detektion gezeigt wird. Darüber hinaus stellen wir die Quadrupol Relaxation als Wirkungsmechanismus für eine grundlegend neue Klasse von reversibel aktivierbaren Kontrastmitteln mit frequenzselektiver Relaxationsdispersion vor.

Keywords: molekulare Bildgebung, Magnetresonanztomographie, fast field-cycling, Relaxationsdispersion, Quadrupolrelaxation, Kontrastmittel

Affidavit

I declare that I have authored this thesis independently, that I have not used other than the declared sources/resources, and that I have explicitly indicated all material which has been quoted either literally or by content from the sources used.

The text document uploaded to TUGRAZonline is identical to the present doctoral thesis.

Date	Signature

Acknowledgments

Danke, Mama und Papa
Danke, Anna

Danke, Nidi und Chris

Danke, Prof. Hermann Scharfetter
Danke, Christian und dem ganzen CONQUER Team
Danke, allen Kooperationspartnern der COST Action EURELAX

Danke, Prof. Rudolf Stollberger
Danke, meinen derzeitigen und ehemaligen Kollegen am Institut für Medizintechnik
Danke, der gesamten MRI Community in Graz

Contents

List of Figures

List of Tables

1 Introduction

> *Whenever we proceed from the known into the unknown we may hope to understand, but we may have to learn at the same time a new meaning of the word 'understanding'.*

Werner Karl Heisenberg, *1901-1976*

The need for a better understanding of fundamental molecular or cellular processes in the human body is omnipresent in medical diagnosis. Over the last centuries, molecular imaging has emerged as a research field with enormous potential to make visible what otherwise would be invisible. Molecular imaging may be defined as the "non-invasive visualization of biochemical events at the cellular and molecular level ..."[1]. It provides an important means for a vast amount of applications ranging from early diagnosis of disease, pharmaceutical developments, theranostics and personalized medicine [2].

Amongst all medical imaging modalities, magnetic resonance imaging (MRI) is known for its superior endogenous soft tissue contrast and delivers high-resolution morphological images all without harmful ionizing radiation. Contrast in MRI is essentially altered by differences in local water proton density and spatially varying longitudinal and transverse relaxation times in the tissue of interest. Extensive research is devoted to extend MR imaging beyond the anatomical and physiological level, towards the spatially and temporally resolved detection of biomarkers associated with molecular and cellular processes [3]. Compared to other modalities like optical or nuclear imaging, molecular MRI is limited by its moderate sensitivity and requires sophisticated signal enhancement strategies such as the use of contrast agents [4]. In addition to increasing sensitivity, the use of biochemically targeted imaging probes is crucial to provide sufficient specificity by enhancing the MRI signal of the molecular target. Besides targeted accumulation on a specific site, it is even

possible to render a contrast agent responsive to the presence (activation) or absence (inactivation) of a biomarker of interest [5–7]. Although there exist a variety of endogenous imaging probes [8], when referring to the term "contrast agent" one usually associates the administration of an exogenous substance with it. Contrast agent detection may involve direct methods, such as spectroscopy imaging or detection of non-proton nuclei (e.g. ^{13}C, ^{19}F, ^{31}P or ^{23}Na), or indirect methods observing their effect on bulk water molecules. This effect can be induced by chemical exchange, magnetization transfer and/or by altering different relaxation pathways, and depends on the underlying magnetic field [9, 10].

The magnetic field dependency of the relaxation rates, also termed as nuclear magnetic relaxation dispersion (NMRD), can provide relevant information about the dynamics and structural order of a wide range of molecular complexes [11]. The relaxation rate as a function of the magnetic field, so-called NMRD profiles, can be measured with fast field-cycling nuclear magnetic resonance (FFC-NMR) relaxometry. While the acquisition of NMRD profiles is an established means in contrast agent design to determine the efficiency for a target magnetic field, in recent years NMRD profiles have gained interest for the characterization of biomarkers related to several disease [12–15]. The latter may be achieved either by exploiting the endogenous proton NMRD profile itself or its alteration induced by an exogenous contrast agent. In traditional MRI, nuclear magnetic relaxation dispersion plays only a minor role. Clinical MRI employs a fixed main magnetic field and therefore has no access to field-dependent information within one system. Fast field-cycling magnetic resonance imaging (FFC-MRI) enables a modulation of the main magnetic field within MRI pulse sequences. This adds an additional dimension to MRI giving access to field-dependent contrast mechanisms, which would be otherwise invisible to traditional MRI. Dedicated hardware is required for FFC-MRI to vary the magnetic field within a defined range. While low-field FFC-MRI systems have access to NMRD characteristics of endogenous biomarkers [16], systems for the clinical field range benefit from the strong magnetic field dependence of particular contrast agents [17, 18]. Notably, the class of slowly tumbling targeted or responsive probes features auspicious NMRD characteristics for the detection of biomarkers with increased specificity and sensitivity.

There exist only a handful of clinical MRI systems worldwide that have been adapted to enable field-cycling within a certain range around 1.5 T. However, the capabilities of field-cycling for higher fields such as 3 T are completely unexplored. The primary research question on that this thesis is build upon is, how variations in the nuclear magnetic relaxation dispersion may be utilized as a contrast mechanism for the detection of biomarkers at a clinical field strength of 3 T. To this end, the work in this thesis is devoted to adapt a 3 T MRI system for field-cycling without compromising image quality. The implemented hardware setup is validated by in-vitro experiments using dispersive contrast agents, and the applicability to detect biomarkers, in particular that of zinc, is shown. Furthermore, the prospects of quadrupole relaxation enhancement as a completely new mechanism for the design of contrast agents with frequency-selective NMRD characteristics are explored.

1.1 Outline of the Thesis

The work conducted and summarized in the following chapters contributes to the field of molecular MR imaging, and, to a certain extent, to the field of MRI contrast agent design. The structure is as follows. **Chapter 2** revises the current state-of-the-art in fast field-cycling MRI. It contains an overview of different approaches to conflate field-cycling with imaging capabilities from MRI and lists hardware systems currently available to research sites. Challenges involved in the implementation and corresponding error correction strategies are discussed. It also reports about potential applications specific for the respective field-cycling ranges. This chapter is based on the journal publication *"Comparison of fast field-cycling magnetic resonance imaging methods and future perspectives"* and represents joint work within the framework of COST Action CA15209. **Chapter 3** involves the implementation and validation of the first FFC-MRI hardware system for a clinical field strength of 3 T. A conventional MRI system was equipped with an additional insert coil dedicated to varying the main magnetic field during an imaging sequence. It is based on the journal publication *"R_1 dispersion contrast at high field with fast field-cycling MRI"*. **Chapter 4** proposes the application of FFC-MRI as a means for zinc detection. It shows that by exploiting field-dependent information it is possible to detect a zinc responsive contrast agent, whereas this probe would be undetectable by accessing only the absolute difference in R_1 with traditional MRI. This chapter is based on the journal publication *"High-Field Detection of Biomarkers with Fast Field-Cycling MRI: The Example of Zinc Sensing"*. **Chapter 5** introduces quadrupole relaxation as a frequency-selective relaxation pathway for the enhancement of water proton relaxation. It proposes the quadrupole nucleus ^{209}Bi as the basis for the design of chemically responsive contrast agents. Proof-of-principle FFC-NMR relaxometry studies show that quadrupole relaxation enhancement leads to frequency-selective NMRD characteristics that may be exploited by FFC-MRI. This chapter is based upon work conducted in the frame of the FET-open project *CONQUER* (European Commission H2020 Programme). The final conclusion of this thesis and outlook of future applications are given in **chapter 6**.

2

Comparison of Fast Field-Cycling Magnetic Resonance Imaging Methods and Future Perspectives

Markus Bödenler[1,†], Ludovic de Rochefort[2,†], P. James Ross[3], Nicolas Chanet[4], Geneviève Guillot[4], Gareth R. Davies[3], Christian Gösweiner[1], Hermann Scharfetter[1], David J. Lurie[4], and Lionel M. Broche[4,†]

[1] Institute of Medical Engineering, Graz University of Technology, Austria
[2] CNRS, CRMBM UMR 7339,Aix Marseille Univ, France
[3] Aberdeen Biomedical Imaging Centre, University of Aberdeen, UK
[4] IR4M UMR 8081, Université Paris Saclay, France
[†]These authors have equally contributed to this work.

Published in:
Molecular Physics 117:7-8 (2019) 832-848
https://doi.org/10.1080/00268976.2018.1557349

Abstract

Fast field-cycling (FFC) nuclear magnetic resonance relaxometry is a well-established method to determine the relaxation rates as a function of magnetic field strength. This so-called nuclear magnetic relaxation dispersion gives insight into the underlying molecular dynamics of a wide range of complex systems and has gained interest especially in the characterisation of biological tissues and diseases. The combination of FFC techniques with magnetic resonance imaging (MRI) offers a high potential for new types of image contrast more specific to pathological molecular dynamics. This article reviews the progress in FFC-MRI over the last decade and gives an overview of the hardware systems currently in operation. We discuss limitations and error correction strategies specific to FFC-MRI such as field stability and homogeneity, signal-to-noise ratio, eddy currents and acquisition time. We also report potential applications with impact in biology and medicine. Finally, we discuss the challenges and future applications in transferring the underlying molecular dynamics into novel types of image contrast by exploiting dispersive properties of biological tissue or MRI contrast agents.

2.1 Introduction

Magnetic resonance imaging (MRI) has emerged as one of the most versatile imaging modalities in clinical diagnosis, providing a wealth of contrast mechanisms. In this respect, human (clinical) and animal (pre-clinical) MRI scans typically exploit differences in local proton (^{1}H) density (mostly tissue water content) and spatially varying longitudinal (T_1) and transverse (T_2 and T_{2^*}) relaxation times or equivalently of their inverse, referred to as the relaxation rates R_1 and R_2 (and R_{2*}) respectively, measured at the fixed imaging magnetic field B_0 of the scanner. Differences in the underlying relaxation behaviour at B_0, and therefore changes in image contrast, can be used to distinguish between healthy and pathological tissues for many diseases [19]. However, contrast mechanisms may change dramatically with the applied magnetic field strength, and these changes can be exploited to obtain new information for medical diagnosis. One way to access field-dependent information is by using fast field-cycling (FFC) methods.

Fast field-cycling nuclear magnetic resonance (FFC-NMR) relaxometry is an established method to measure the changes of relaxation times with the field strength B_0, referred to as nuclear magnetic relaxation dispersion (NMRD) profiles. The magnetic field strength is typically rapidly cycled during the FFC-NMR experiment, allowing relaxation to occur at a wide range of field strengths but always returning to the same magnetic field for detection of nuclear magnetic resonance (NMR) signals [20]. As an example Figure 2.1 shows a FFC-NMR pulse sequence. B_0 varies over time to form three plateaus: the first one is for polarisation and increases the amplitude of the signal response, the second plateau leaves the spin system to evolve at the field of interest with its corresponding T_1 value and the last plateau serves for detection of the ^{1}H NMR signal.

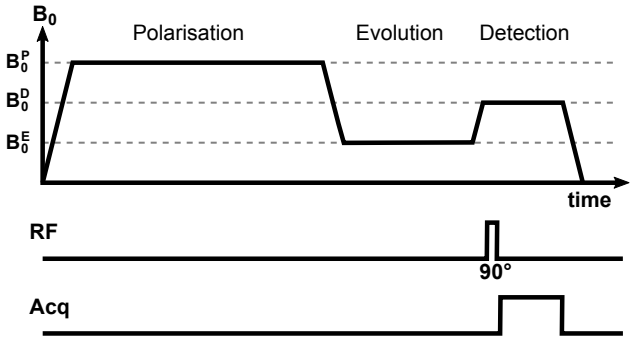

Figure 2.1: Example of a typical pulse sequence for FFC-NMR. The top line represents the main magnetic field, switching from 0 to polarisation B_0^P and evolution B_0^E followed by a transition to the detection field B_0^D. At the bottom the radiofrequency pulse and signal acquisition timing. Note that the transitions between the plateaus are much shorter than the typical T_1 values, a necessary condition for FFC-NMR.

Repeating this sequence with different evolution times allows finding T_1 at the evolution field, so that repeating the overall method for different evolution fields provides a measurement of the dispersion of R_1 (an example of a ^{1}H R_1 NMRD profile is shown on Figure 2.2). As R_1 relaxation mostly depends on characteristic times of microscopic motions (such as translation and rotation) and possible energy dissipation through matching energy levels of some molecular structures (such as interactions with quadrupole nuclei), R_1 NMRD profiles give insight into the molecular dynamics and structural order of a wide range of complex systems such as organic solids, metals, polymers, liquid crystals, porous media, exogenous contrasts agents or biological systems [21–24]. While used for a long time as a tool in the development phases of MRI contrast agents, over the last decade FFC-NMR has gained interest in the characterization of biological tissues and diseases [13, 25–27] by either exploiting the endogenous ^{1}H R_1 NMRD profile itself, or its modifications produced by exogenous contrast agents. These results demonstrate that FFC methods have a great potential in medicine if combined with MRI and much efforts are dedicated to create fast field-cycling magnetic resonance imaging (FFC-MRI) scanners [18, 28–31].

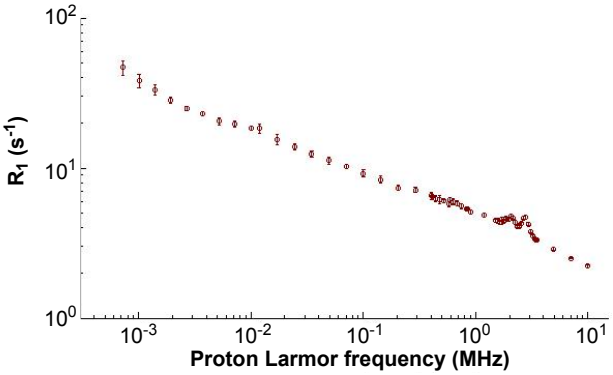

Figure 2.2: ^{1}H R_1 NMRD profile of healthy human cartilage obtained from the Aberdeen FFC-MRI research group [13]. Cartilage shows a marked dispersion over several decades of field strength, or equivalently proton Larmor frequency. Quadrupole peaks can also be observed around 2.5 MHz that inform on water-protein interactions.

Fast field-cycling adds an extra dimension to MRI by allowing the B_0 field to be changed during the pulse sequence and an optimal magnetic field can be selected for each of the main phases of an MRI pulse sequence (polarisation, relaxation and acquisition). This allows the generation of images displaying the variation of R_1 with respect to the magnetic field in ex vivo and in vivo biological tissues, non-invasively, with a high potential to generate new types of image contrast specific to pathological molecular dynamics and thus useful for disease characterisation and diagnosis.

Compared with conventional MRI, FFC-MRI requires dedicated hardware to vary the magnetic field B_0 rapidly compared to the relaxation times. Implementation poses strong constraints on magnet design, power supplies, control electronics, pulse sequences, scan

time and image quality. These constraints require compromises and add serious difficulties to the construction of FFC-MRI scanners so that at present FFC-MRI system developments are limited only to a small number of research groups worldwide exploring different approaches ranging from completely home-built human-scale systems at low field to B_0 insert coils for commercial MRI systems at clinical fields of 1.5 T and 3 T.

The purpose of this article is to provide an overview of the recent advances in the field of FFC-MRI and to review different approaches as well as to present their advantages and drawbacks. First we present an overview of FFC-MRI hardware designs, their limitations and the error correction strategies being employed. Then we present the acquisition strategies currently developed to tackle image reconstruction problems that are specific to FFC-MRI. Finally, we discuss the challenges and the potential applications that can arise by exploiting the dispersive properties of biological tissues and selected MRI contrast agents, transferring the underlying molecular dynamics into new types of image contrast on biological tissues, including living materials.

2.2 FFC-MRI technologies

Various systems exist that allow changing the magnetic field during a pulse sequence in an FFC-MRI system. Each technology presents its strengths and weaknesses. An overview of the early developments and history of FFC-MRI hardware systems can be found in references [28, 32] and a summary of the latest hardware systems is presented in Table 2.1 and detailed below. Performing FFC-MRI systems are expected: (i) to switch the main magnetic field in a time shorter than the sample T_1 at these fields, (ii) to access a large range of magnetic field strength in order to provide a large overview of the R_1 NMRD profile, both at the high and low end of the Larmor frequency spectrum and (iii) to be large enough to accommodate relevant objects for imaging. The practical implementation of these requirements necessitates to make various compromises and several designs exist that suit different purposes. FFC-MRI bears resemblance with ultra-low field MRI [33], which is not covered here, that similarly relies on electromagnets to produce a pre-polarizing field but signal detection is performed with superconducting quantum interference devices (SQUIDs) at ultra-low field. Below is a description of the magnet technologies currently used for FFC-MRI.

2.2.1 Dual resistive and permanent whole-body magnets

This technology combines the stability of a permanent magnet with the reactivity of a resistive one, both of whole-body sizes. This approach has been developed in Aberdeen, UK [34, 37] and can reach magnetic fields from 5 mT to 120 mT with an acquisition field of 59 mT. It consists of a vertical-field ferrite magnet using a Halbach configuration and a vertical resistive insert magnet that adds to or subtracts from the permanent field. The overall system has a bore size of 52 cm, which is enough for whole-body human scans.

Table 2.1: Overview of current FFC-MRI systems and their characteristics.

FFC-MRI system	Type	Acquisition field	FFC range	Bore size
Bödenler et al. [31]	insert coil	2.89 T	2.79 - 2.99 T	small animal
de Rochefort et al. [30]	insert coil	1.5 T	1 - 2 T	small animal
Harris et al. [29]	insert coil	1.5 T	1.28 - 1.72 T	small animal
Hoelscher et al. [18]	insert coil	1.5 T	1.41 - 1.59 T	small animal
Lurie et al. [34]	dual resistive and permanent	59 mT	5 - 120 mT	whole-body
Ross et al. [35]	resistive	0.2 T	0.1 mT - 0.2 T	whole-body
Pine et al. [36]	insert coil	59 mT	3 - 115 mT	forearm

A key element of the dual-magnet approach is that signal acquisition takes place only in the field of the permanent magnet, with the insert magnet inactivated, and the scanner exploits the short-term stability of the permanent magnet to avoid artefacts in the image, while the resistive magnet varies the relaxation field over a relatively large Larmor frequency range during the spin preparation stage. One drawback of this design is that the field inhomogeneities of the two magnets add up when reaching very low B_0 so that the lowest field attainable is about 1 mT when scanning an object the size of a head. Moreover, the use of ferrite magnets restricts the imaging field to relatively weak B_0, which limits polarisation (120 mT in the Aberdeen dual-magnet system) and increases the scan time required to obtain exploitable images. Additionally, the magnetic field generated by permanent magnets is temperature-dependant (on the order of 0.2 % per degree for ferrite [34]), requiring either to control the room air temperature or to monitor the variations of the magnetic field.

2.2.2 Single resistive magnet

FFC-MRI designs based on a single resistive magnet present two main advantages: they can produce relatively strong magnetic fields per weight compared with a permanent magnet and the homogeneity of the magnet scales with the current so that it is not the dominant limitation when reaching very low magnetic fields. Current developments focus on a completely resistive whole-body FFC-MRI device [35] in an effort to reach even lower B_0 fields for relaxation on the one hand and to increase the imaging field strength on the other hand. This scanner has a bore of 50 cm, which is quite narrow but does permit whole-body scans of slim people (see Figure 2.3a). It is capable of reaching field strengths up to 0.2 T and down to 100 μT but work is currently in progress to extend its lower limit to 5 μT to extend the range of the NMRD profile. The use of a purely resistive magnet makes it easier to explore low magnetic fields because the magnet inhomogeneities scale down with the field strength so that the limitations in the ultra-low field regime mainly come from the Earth's field (typically 40 μT depending on the location) and from magnetic fluctuations from the environment, such as moving elevators, nearby traffic, mains electricity supply or ferromagnetic structures within the building. The latter may generate local fields signifi-

cantly stronger than Earth's as well as field gradients (10 to 50 μT/m is not uncommon). However, FFC experimentation imposes fast current variations in the magnet so that its inductance must be kept to a minimum. Low inductance makes it more difficult to drive the magnet consistently and limits the field stability so that particularly stable and fast current amplifiers are required for this scanner.

2.2.3 Superconducting magnet with resistive insert coil

Alternatively, FFC-MRI can be implemented by inserting a resistive B_0 insert coil into an otherwise conventional clinical MRI system (see Figure 2.3b). The resistive B_0 insert coil provides the B_0 field modulations necessary for field-cycling experiments while images can be acquired by the MRI system as usual. This combines the advantage of a stable acquisition field, provided by the permanent or superconducting primary magnet of a conventional MRI system, with the fast-switching capability of a resistive coil with low inductance. The offset coil can be mounted on the patient table and positioned at the isocenter of the main magnet. The insertion coil is designed for an easy installation and removal, and provides a flexible utilisation of the FFC technology, while maintaining the basic operation mode of the MRI system. A schematic of a typical on-site integration can be found in Figure 2.3c.

Several research groups worldwide have realized this approach, employing magnetic field strengths used in current clinical routine such as 1.5 T and 3 T, in order to implement a method known as delta relaxation enhanced magnetic resonance (dreMR) imaging, aimed at exploiting the detection of molecules (including contrast agents) with particular dispersion characteristics. Alford et al. [38] at the University of Western Ontario were the first to describe the use of an insert coil, capable of modest field shifts of $\pm$70 mT, within a clinical MRI system with a nominal field strength of 1.5 T. Later on, this first prototype insert coil design was improved by Harris et al. [29] leading to B_0 offset fields of $\pm$ 0.22 T. Other systems at 1.5 T were implemented by Hoelscher et al. [18] and de Rochefort et al. [30], the latter reporting the currently highest ΔB_0 of $\pm$0.5 T. Although the majority of available hardware setups are based on 1.5 T MRI systems, recently, Bödenler et al. [31] proposed an implementation centred at a nominal B_0 field strength of 2.89 T. Table 2.2 compares hardware specifications like ΔB_0, inductance, resistance, field efficiency, imaging region and physical dimensions of B_0 insert coils currently used for dreMR.

Despite the use of a clinical MRI system for signal detection, the bore sizes of all these insert coils are small (ranging from 40 - 100 mm in diameter). The limitation mostly comes from the inductive coupling between the resistive insert and the superconducting magnet: large currents are used in the resistive coil to generate large magnetic fields that are switched quickly, so the large variations of the insert stray field induce electric currents in the conductive parts of the permanent magnet. These currents may quench it during the B_0 field ramps. One way to mitigate this problem is to use an active shield to minimize

Table 2.2: Comparison of B_0 insert coil specifications.

dreMR coil	ΔB_0 (mT)	L (mH)	R (mΩ)	field efficiency (mT/A)	imaging region		physical dimensions			theoretical power at max. field
					⌀ (mm)	length (mm)	bore ⌀ (mm)	outer ⌀ (mm)	length (mm)	
Hoelscher et al. [18]	±90	4.90	60	2.54	34	50	52	242	340	75 W
Harris et al. [29]	±220	1.46	95	0.87	25	50	80	320	420	6.1 kW
de Rochefort et al. [30]	±500	0.30	100	1.57	28	40	40	170	300	10 kW
Bödenler et al. [31]	±100	1.69	64	0.67	40	40	100	345	514	1.4 kW

the interaction with the host system. Another way is to reduce the size of the insert coil: the stray field decreases with the cube of the diameter to distance ratio so that smaller inserts produce a weaker stray field in the scanner structure and allow maintaining fast ramps. However, they offer a small imaging volume (ranging from 25 - 40 mm in diameter) that limits the use of such systems to pre-clinical small animal experiments. Yet feasibility studies by Harris et al. [39, 40] have investigated B_0 insert coil designs suitable for human head and prostate imaging, which is an important step for transferring the dreMR method to human-scale applications.

Another important consideration is the power deposited in such an insert coil as it scales with the square of the required current and therefore field strength. Considering the designs presented in Table 2.2, it can be estimated that the power dissipated by Joule effects at maximum fields ranges between 75 W to 10 kW. An adapted cooling system is then required for heat extraction from the resistive windings for each system. Limited cooling capacity of the insert coil requires duty cycle adjustments or/and the maximum field (current) must be reduced. Therefore, a sufficient cooling capacity of the insert coil has to be considered during the design process as a change after construction is difficult. For example, the insert coil from Hoelscher et al. is limited to a duty cycle of 1:8 to allow for sufficient cooling. Harris et al. [29] implemented an effective cooling system so that the operation (6 kW generated at maximum field) is only limited by the duty-cycle of the power supply. They utilize a parallel water flow through each winding layer to increase the water flow and therefore the heat extraction. The cooling system involved in [30] (10 kW generated at maximum field) has a primary closed-loop circuit with circulating perfluorocarbon in contact with the insert coil and a secondary circuit with circulating water. The insert coil (1.4 kW at maximum field) in [31] employs a cooling system with six internal multipath circuits filled with water and the operation is only limited by the duty cycle of the power supply.

In contrast to the horizontal-field scanner geometry used in the clinical MRI systems described above, Pine et al. [36] presented a disk-shaped, vertical-field insert coil for the use with a 59 mT permanent-magnet vertical-field scanner. The combination of this geometry with a surface radio frequency (RF) coil provides an improved flexibility with respect to the imaging region of the patient when compared to the reduction in accessible bore size for a solenoidal insert coil geometry currently used in horizontal-field MRI systems.

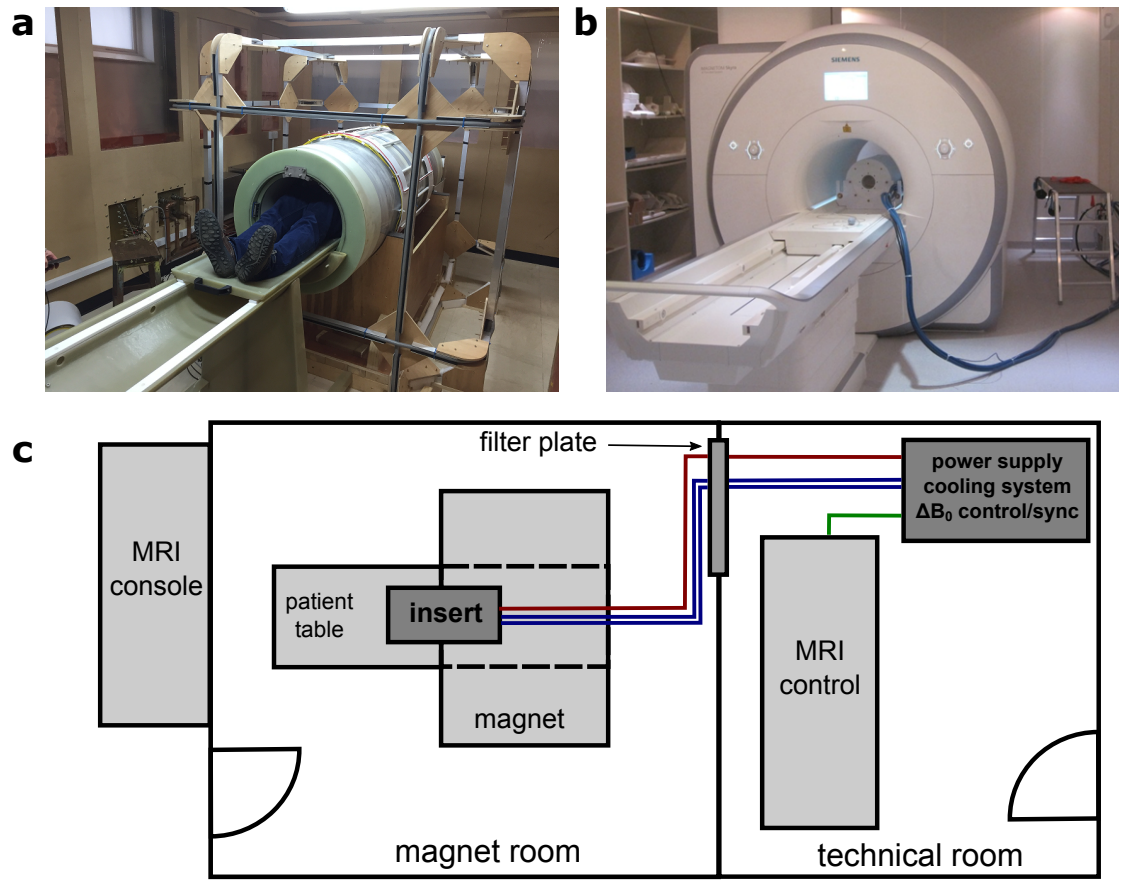

Figure 2.3: Integration of the FFC-MRI systems in their respective environments. (a) Current developments at the University of Aberdeen focus on a completely resistive human-scale FFC-MRI device [35] reaching a field strength up to 0.2 T. This scanner has a bore of 50 cm allowing for whole-body scans of slim people. (b) Shows a resistive B_0 insert coil within the bore of a superconducting magnet system at a field strength of 3 T [31]. Although this method uses clinical MRI systems for signal detection, the small bore sizes limit the imaging volume to pre-clinical small animal experiments. (c) Schematic of a typical on-site integration of an insert coil for an otherwise commercial MRI system.

2.3 Technical Comparisons

2.3.1 B_0 field stability and homogeneity

Most MRI image acquisitions are performed in the k-space and the phase of the NMR signal is essential for the image reconstruction process. Errors in the phase measurements in the order of half a degree or more lead to visible ghosting artefacts that degrade the image (see Figure 2.4). To mitigate this problem, field inhomogeneities are usually corrected by using spin echo sequences but this approach has limited results for time-varying fluctuations.

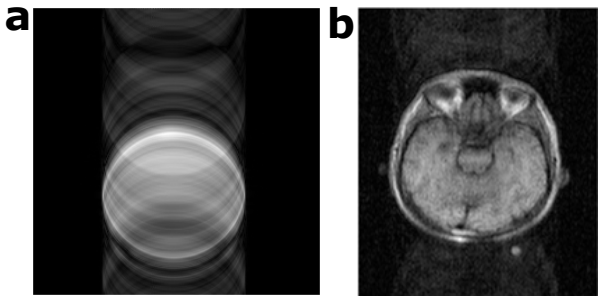

Figure 2.4: Small deviations of B_0 induce shifts in the signal phase that degrades the image producing ghosting artefacts e.g. (a) phantom image obtained from a B_0 insert coil [31] and (b) head scan obtained from a resistive whole-body magnet [41].

The average NMR phase from a simple spin-echo experiment can be modeled as follows

$$\varphi(2\tau) = \gamma \left[\int_0^{\tau} B_0(t)dt - \int_{\tau}^{2\tau} B_0(t)dt \right], \tag{2.1}$$

where τ is the delay between the excitation and refocusing pulses, γ is the gyromagnetic ratio and $\varphi(2\tau)$ is the phase of the NMR signal when the echo forms. One can simplify the expression above by using a polynomial expansion of the field B_0

$$\varphi(2\tau) = \gamma \left[\int_0^{\tau} \sum_{i=0}^{\infty} b_i t^i dt - \int_{\tau}^{2\tau} \sum_{i=0}^{\infty} b_i t^i dt \right], \tag{2.2}$$

where b_i are the decomposition coefficients of the B_0 series. This gives:

$$\varphi(2\tau) = \gamma \sum_{i=0}^{\infty} \frac{b_i}{i+1} \tau^{i+1} \left[2 - 2^{i+1} \right]. \tag{2.3}$$

The terms of this series only cancel out for constant fields and dephasing increases with larger orders and with the echo time. Hence phase errors can only be corrected by better control of the magnetic field or by shortening the echo time, but the latter increases the acquisition bandwidth and lowers the signal-to-noise ratio (SNR). Permanent or superconducting magnets have stability time constant orders of magnitude larger than the echo time so they are not affected by this problem and any drift can be corrected by tracking the resonance frequency every few minutes. Fast temporal fluctuations of the magnetic field are mainly a problem when dealing with resistive magnets, either in isolation or in an insert system if the resistive coil is not disabled during image acquisition. In such systems the field fluctuations that affect the phase of the NMR signal are due to imperfect control of the electric current by the magnet power supply. Yet resistive magnets are natural

low-pass filters with a frequency f defined by their inductance L and resistance R:

$$f = \frac{R}{2\pi L}. \tag{2.4}$$

It results that field stability is more easily achieved with large inductance and low resistance (which requires some compromises), however reducing the cut-off frequency of the magnet also reduces its response time for the field ramps and makes it more difficult to drive, requiring power supplies able to provide large voltages. Particular care is therefore necessary to design resistive magnets for FFC-MRI to balance these needs. As an example, ramp times are typically 1 to 10 ms long whereas echo times can reach 10 to 40 ms, hence a possible trade-off could be to set a cut-off frequency between 20 and 60 Hz.

For the insert system with the highest field offset reported above (500 mT obtained with 320 A, with and a cut-off frequency of 50 Hz [30], the current fluctuations remaining during signal acquisition are typically producing NMR frequency fluctuations up to 200 Hz. To avoid such fluctuations during the acquisition phase, which uses the stable main field of the superconducting magnet, an ad-hoc strategy is to switch to a highly resistive state, which is equivalent to opening the coil circuit by disabling the amplifier [31]. Another approach is to switch the amplifier load between the insert coil and an inductance-matched dummy load using a fast high-power solid state switch [29].

Whole-body resistive FFC-MRI scanners present less problems and experimentation on the Aberdeen 0.2 T system showed fluctuations lower than 2 ppm (8 Hz proton Larmor frequency). It produces images with visible artefacts but these can be corrected by post-processing [41], where the background signal is minimized by finding the optimum phase correction for each k-space line.

Theses resistive magnets also produce heat that leads to field drift via thermal expansion, similar to what is observed with permanent magnets. This effect can reach 0.1% of the full field so it is of little concern for insert magnets but causes large field drifts in whole-body systems during the detection field. Correction techniques can easily be applied by scaling B_0 as the acquisition progresses, taking advantage of the long time constant associated with such thermal effects (40 minutes on the Aberdeen 0.2 T system). Yet this requires access to the data acquired during the scan.

Permanent magnets also present problems with field stability because of their temperature dependence. The dual FFC-MRI magnet at Aberdeen is based on ferrite and is thermally controlled but the resistive insert generates heat during field-cycled experiments. As a result, B_0 fluctuates over several kHz when acquiring field-cycled T_1 maps but the characteristic time of the drift is very long compared with an acquisition so that one can make some corrections during the experiment, using one acquisition set to correct for the next one. Note that in this case the field correction cannot be done by adjusting B_0, but by adjusting the system frequency from the MRI console.

2.3.2 Signal-to-noise ratio

SNR is a crucial parameter for MRI images: large SNR allows detecting with higher accuracy and improved spatial resolution, which are desirable for medical applications. SNR depends largely on the acquisition field strength [42], which limits the technology available for the detection of the NMR signal. At NMR frequencies typically higher than 1 MHz (corresponding to 23 mT for ^{1}H), inductive detection can be used efficiently with mature technologies involving preamplifiers, acquisition electronics and radiofrequency coil designs. With such systems, the signal-to-noise ratio is summarised as

$$SNR = \gamma NPKC\sqrt{T_{acq}}, \tag{2.5}$$

where γ is the gyromagnetic ratio, N is the number of nuclei within the imaged volume, P is the polarisation at equilibrium (which is proportional to the polarisation field under the Curie law), K provides the sensitivity of the RF detection coil (which is proportional to the acquisition field), C relates to the contrast due to relaxation and depends on the pulse sequence applied, and T_{acq} is the total acquisition time. As can be seen, in the choice of a strategy for FFC-MRI, the magnetic fields and their timing during the three distinct phases of polarisation, relaxation and acquisition interact in determining the achievable SNR. Separating each phase, SNR increases linearly with polarisation, motivating the use of high field or pre-polarising approaches when lower field FFC-MRI are used. Regarding the acquisition field, for biological tissues maintained at body temperature, an optimised RF detection setup would be in the sample-noise dominating regime, in which K is only dependent of the coil geometry and not on the acquisition frequency. However, in practice this regime is not always reached, when other noise sources dominate such as intrinsic RF coil noise, preamplifier noise and noise due to electromagnetic coupling with the environment. The limitation of noise performance depends on the acquisition field strength and RF coil size, with higher fields being more susceptible to patient noise while coil noise usually dominates at lower fields. Regarding the relaxation field that provides the image contrast, it is completely determined by the relaxation behaviour under the applied pulse sequence, with a trend to have shorter T_1 at lower fields, enabling to sensitize faster to this parameter. Finally, if an SNR is targeted for a given system, two basic imaging parameters can be adjusted to achieve it, the voxel size (to increase the number of nuclei N), and the available time the signal is actually acquired. In summary, an ideal system would benefit from high-field pre-polarization, optimized acquisition field in the sample-noise dominating regime, and from the most relevant relaxation field to reveal field-dependant contrast.

However, in practice, experimental factors also impact SNR depending on the technology used. In particular, the heat dissipation in the resistive coil in FFC-MRI requires efficient cooling, and limitations of currently-available power-supply amplifiers lead to limited duty-cycles of the magnetic field. The most constrained systems in that matter are the resistive FFC-MRI magnets such as the one in Aberdeen which operates at a maximum of 50 % duty

ratio to allow the current amplifiers to cool down when operating at 0.2 T. Additionally, pre-polarisation at 0.2 T can only last up to 2 seconds so that tissues with long T_1 cannot be completely polarised, which decreases SNR accordingly. The cooling time is also lost in terms of acquisition time and increases the scan duration, typically by a factor 1.2 to 2. Insert systems also have restrictions imposed by their cooling systems but these mainly impact the magnet size because of the volume occupied by the cooling pipes.

2.3.3 RF coil setup

While a variety of commercial solutions exist for RF coils used in conventional MRI systems, FFC-MRI scanners present various non-standard features such that the RF coil has to be home-built. Design considerations differ according to the frequency regime and the RF coils designs vary between the insert and the whole-body systems even if in both systems the ratio of the wavelength to the cavity dimension is much larger than unity and the birdcage or saddle coil geometries are well-suited for the coil shape.

Insert magnet systems operating at 1.5 T or 3 T are characterised by resonant frequencies on the order of 100 MHz range and tight volume. An example of coil for such systems is presented in Figure 2.5 [43]: its diameter is set to fit tightly inside the insert bore of 40 mm diameter and the shield is very close to the coil during insertion, which causes large detuning when inserted inside the insert magnet. At high frequency the design of the inductive loop also needs to take into account the wavelength of the RF signal in the conductors. For MRI systems operating at 1.5 T, the proton NMR frequency is about 64 MHz and the corresponding wavelength in vacuum is 4.7 m. This number drops down to 2.8 m in typical RG58 coaxial cables and is further reduced as B_0 increases. This requires particular care when placing lumped elements on large RF coils, such as used for human scans, and numerical simulations are required to validate the behaviour of the coil and avoid hot spots that could generate RF burns. Baluns are also needed at regular intervals along the transmission line to prevent current conduction along the cable shield, which could also result in burns and increases the signal noise, though these problems are not significant for animal-size systems.

Acquisition on the whole-body 0.2 T FFC-MRI scanner also requires custom RF coil design to adapt to low-frequencies, and this field strength is no longer used by MRI manufacturers. Such coils typically include large tuning capacitors, (typically hundreds or pF to several nF), large matching capacitors to adapt the load to the 50 ω transmission line (usually hundreds of pF), thick conductors to take advantage of the large skin depth (100 μm to accommodate a skin depth of about 20 μm) and large windings or multiple turns to increase the inductance. They also have some interesting benefits such as negligible dephasing with conductor length, since the wavelength at such frequencies is above 30 m, low power consumption from the RF power amplifier, Q factors typically between 100 and 400 depending on the geometry and low patient loading so that the Q factor remains high when the coil is

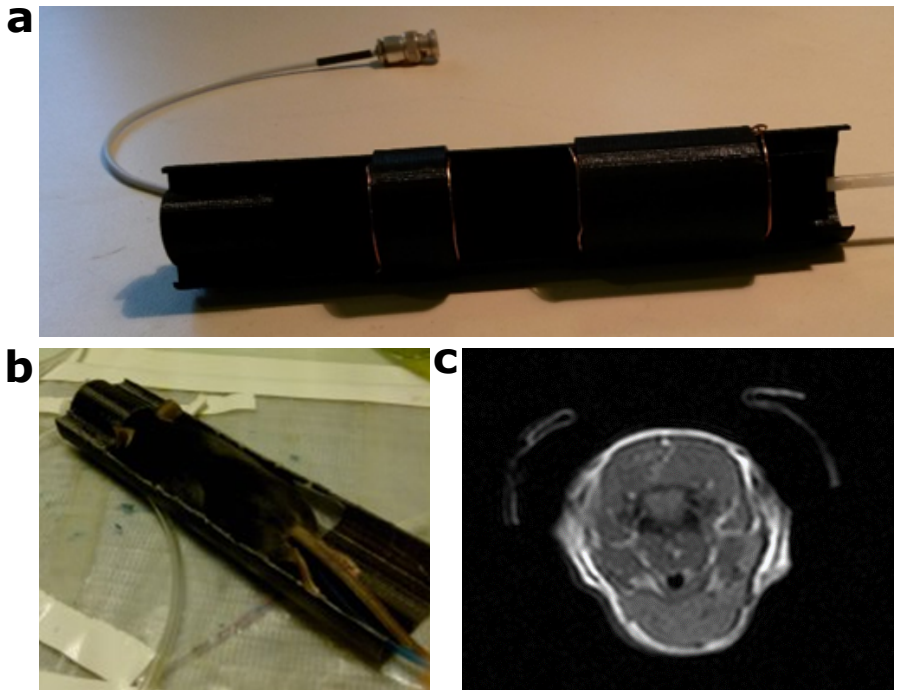

Figure 2.5: Specific RF coil design (a) and small animal bed adapted to gaseous anaesthesia (b) fitted to the tight available space due to the small bore size of the B_0 insert coil [43]. Exemplarily, an in vivo mouse image (axial slice at the neck level) obtained with the dedicated RF coil is shown in (c).

used (coil noise regime). They also require very few baluns, if any, so the risk of RF burns remains small. An important improvement could come from the use of parallel imaging (PI) techniques [44] in FFC-MRI. PI is a routine method to accelerate image acquisition over a wide range of applications in conventional MRI, but this approach relies on the use of coil arrays and such detectors require additional components such as pin diodes for active decoupling and low input impedance preamplifiers for passive decoupling. The lack of readily available dedicated low-impedance preamplifiers at frequencies below 20 MHz makes coil arrays difficult to build at low frequencies for the moment. This is aggravated by the large inductors needed at low magnetic fields, which cannot be miniaturised into the currently existing high-field preamplifiers so that new designs must be created for applications at the MHz regime. Additionally, filtering elements such as present on the DC bias line of the PIN diodes are less efficient at low magnetic fields so that a trade-off must be found between the size and the signal loss of the coil array control boards. Developments in this field are currently ongoing in Aberdeen.

2.3.4 Eddy currents

FFC-MRI is prone to eddy currents resulting from the fast variations of the resistive coil inducing currents in all surrounding conductive materials. Their importance consequently depends on the scanner design. Insert magnets tend to generate most eddy currents because of the large amount of conductive materials incorporated in the cryostats and support structures of superconductive magnets; eddy currents generated in liquid-He temperature structures such as radiation shields may be particularly problematic since the eddy current lifetime is prolonged due to high conductivity at low temperature. Insert magnet coils may need to be actively shielded in order to reduce the risk of quenching the main magnet. Eddy currents do appear significantly in dual-magnet FFC-MRI systems but a small delay before image acquisition (1 ms) is usually sufficient to avoid artefacts, and no eddy currents have been observed so far in the Aberdeen team's purely-resistive FFC-MRI magnet, which can be explained by the absence of conductive surfaces around the magnet and the use of copper mesh for the RF shield.

Most effects have been reported in the case of insert coils into superconductive MRI systems used for dreMR imaging [29–31, 45]. Typically, to characterise them, a ΔB_0 pulse of trapezoidal shape with defined ramps, flat top time and amplitude is applied. The induced eddy current field varies temporally and can be characterized by a mono-exponential (or even multi-exponential) decay. A comprehensive analysis of eddy current formation has been given by Hoelscher et al. in [45]. The main problem with induced eddy current fields is that they result in temporally varying offset in the Larmor frequency. This frequency offset gives rise to a shift of the field of view (FOV) along frequency and slice encoding axis causing substantial degradation of the dreMR image quality due to subtraction artefacts. A typical eddy current characterisation can be found in Figure 2.6a. The influence of the shifted FOV on FFC-MRI images can be seen in Figure 2.6b-c. To illustrate this problem, we consider a system with a maximum gradient strength of 45 mT/m acquiring over a slice thickness of 1 mm so that the maximum slice selection transmit bandwidth would be around 1.9 kHz. In such a situation the 380 Hz (peak) frequency shift induced by eddy currents as seen in Figure 2.6c dynamically shifts the FOV in the slice direction by up to 200 μm, a dynamic slice selection error of 20 %. Similarly, such eddy currents would produce a shift of 180 μm within the plane of the image. This clearly indicates the need for a compensation of such effects for such preclinical systems.

Two strategies are then usable to compensate for these effects, the first one is to wait long enough to go below a predefined shift level, the other is to compensate based on an underlying calibrated linear model in prospective (through real time RF modulation or compensation coils) or retrospective (through signal demodulation) ways, as the shifts are small enough to be restricted to the bandwidth of the RF setup. One prospective way to compensate eddy current effects, proposed by Hoelscher et al. [45], is to modulate the system reference frequency (based on the identified decay model) in such a way that the offset

between system reference frequency and Larmor frequency is zero throughout the pulse sequence. In principle, this compensation can be implemented into any sequence type and does not require any additional hardware modifications. Another approach implemented by Harris et al. [29] is to apply an additional compensation field with a dedicated low-power Helmholtz coil counteracting the eddy current decay during image acquisition.

Both approaches rely on an accurate eddy current characterisation and may be compromised by phase instabilities. It is important to note that the characterization parameters are specific to the parameters of the ΔB_0 pulse such as amplitude, ramp times, flat top time and repetition time. For example a compensation based on the parameters determined in Figure 2.6a is only valid for a ΔB_0 pulse with an amplitude of 100 mT, duration of 300 ms and ramp times of 1 ms. The repetition time (TR) has to be chosen to account for a sufficient eddy current decay before applying the next field-shift. In this example, a TR shorter than 900 ms would lead to an incorrect compensation as the eddy currents of the previous field-shift add to the eddy current field of the next one. Furthermore, the characterization parameters may be altered slightly by a repositioning on the patient table between experiments. In practice, however, these problems can be overcome by performing a re-characterization prior the actual experiment to account for different timing and field-shift parameters. Whereby, it is possible to account for other effects like a slightly altered coupling between the insert coil and the MRI system by a repositioning of the coil on the patient table between experiments.

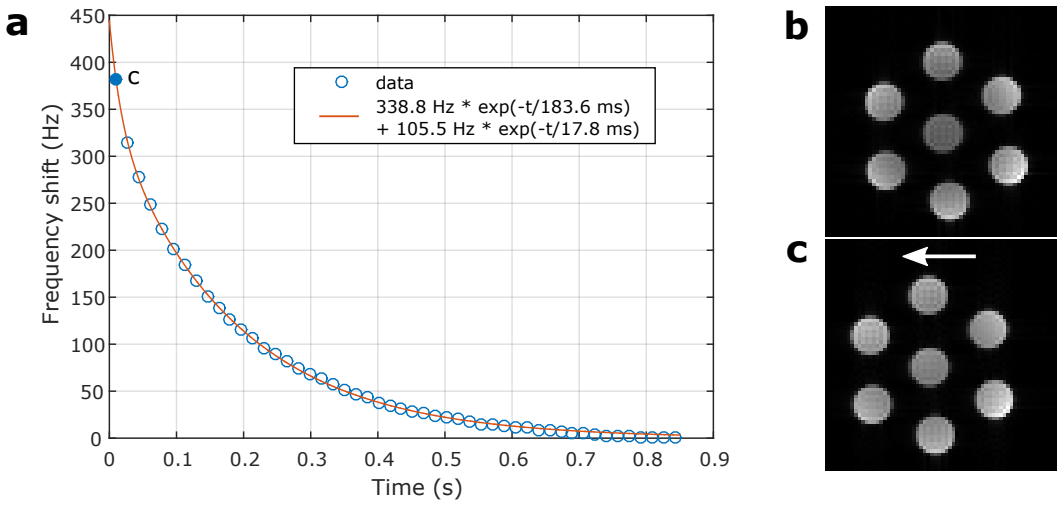

Figure 2.6: (a) Measured (blue circles) frequency shift induced by eddy currents in the FFC-MRI system for 3T (ΔB_0 = 100 mT, T_{evol} = 300 ms and ramp times of 1 ms) [31]. The red solid line represents a bi-exponential model fit. This frequency offset results in a shifted image (c) with respect to the reference image (b) without applied ΔB_0. The shifted image in (c) corresponds to the frequency offset in the first data point (filled circle) and clearly indicates the need to compensate for such eddy current effects.

2.3.5 Pulse sequences

Magnetisation-prepared spin-echo pulse sequences have been commonly used in FFC-MRI to determine R_1 dispersion maps (e.g. in [31, 46, 47]); this has been adopted as it corresponds to the gold-standard way to measure R_1. In the most general case it comprises three phases between which the magnetic field B_0 is switched: polarisation, evolution and acquisition [28]. During the evolution phase the spin system undergoes relaxation imposed by the applied evolution field. Signal acquisition is always carried out at the same detection field strength and can either be the nominal B_0 of a permanent or superconducting magnet system, or at the maximum field for resistive magnets (dominance regime) to increase SNR. A pre-polarisation of the magnetisation is not necessarily required in the high SNR regime and therefore the polarisation field is equal to the detection field. This scheme has to be repeated in the usual manner for the acquisition of the whole k-space.

One important limitation of FFC in the design of pulse sequences comes from the detection technology. The use of tuned transmit and receive coils imposes the use of the corresponding field for detection and as a consequence only the detection field allows modifying the spin system by RF pulses, or detecting the NMR signal. This forbids the use of speed-up strategies such as parallel slice acquisitions, at least during the evolution field. FFC measurements are also iterative: R_1 maps are generated for each evolution field by acquiring series of images with varying evolution times. As an example, a 128 x 128 image with 12 sec repetition time, and 2 evolution fields and 5 evolution times would provide a quantitative $\Delta R_1/\Delta B_0$ map in 4 hours and 16 minutes, which is definitely not practical.

Depending on the application, qualitative $\Delta R_1/\Delta B_0$-weighted images (e.g. dreMR image contrast) can be acquired, as illustrated in Figure 2.7b, In such case the overall measurement time can be reduced by acquiring only two images needed for image subtraction. In the above example this would lead to a measurement time of 51 min, which is achievable for in vivo scans but not practical for clinical use. It is therefore crucial in FFC-MRI to speed up the measurement procedure under consideration of particular hardware restrictions and without significantly compromising the SNR.

FFC-MRI offers two ways to do so, either by speeding-up k-space acquisition strategies or by exploiting the data redundancy in the NMRD profile. For the latter, Broche et al. [37] proposed a multi-field two-point method to estimate R_1 for different evolution fields, reducing the number of images to one image per evolution field and an additional reference image taken at the detection field. This approach provides reasonably accurate R_1 values in less time and is valid for relatively linear regions in the NMRD profile. To speed up k-space acquisition in the context of FFC-MRI, several strategies have been followed successfully, such as faster imaging modules like Rapid Acquisitions with Refocused Echos (RARE) [48]. In contrast to conventional spin echo sequences, in RARE imaging multiple lines of k-space are acquired within one TR interval instead of only one. Echo train lengths of up to 4 were used in studies by Ross et al. [46] and Araya et al. [47] without image

degradation. This speed up by a factor of 4 reduces the acquisition time per image in our example from approximately 25 minutes to a reasonable 6 minutes. Furthermore, the use of steady-state sequences like fast low-angle shot (FLASH) [49] or IR-Look-Locker [50, 51] may be considered in conjunction with field-cycling. In the line of the adaptation of fast MRI pulse sequence with R_1 contrast, Chanet et al. [52] provided a theoretical derivation and analysis of the FLASH steady-state signal equation modified for field-cycling. Such sequences are usually used with short TRs, which, on the one hand, may reduce the acquisition time significantly but on the other hand poses high demands on the FFC hardware. In particular, TR could be limited by eddy current effects, ramp times and/or duty-cycle of the field shifts.

The choice of acquisition schemes is reduced in the Aberdeen team's resistive FFC-MRI scanner because of the limited duty-cycle ratio of the scanner. As mentioned earlier, this scanner may overheat if driven continuously and a 20 to 50 % duty cycle must be observed to avoid problems so that steady-state approaches are difficult to develop. Additionally, the field temporal stability is relatively poor and the signal phase fluctuates randomly with a typical decorrelation time of 15 ms, making Carr-Purcell-Meiboom-Gill (CPMG) or other similar techniques inefficient. This also prevents averaging the complex signal since the random phase error tends to cancel the signal out.

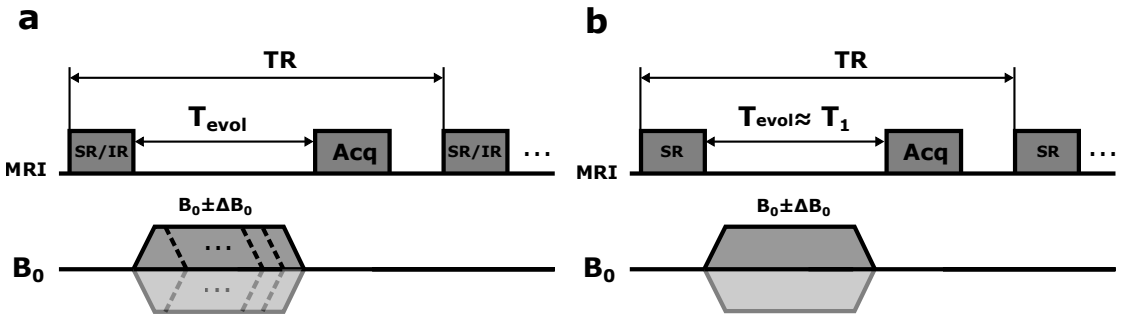

Figure 2.7: Comparison between FFC-MRI pulse sequences used for (a) quantitative $\Delta R_1/\Delta B_0$ mapping and (b) qualitative R_1 dispersion imaging in the case of dreMR imaging. In (a) R_1 mapping is performed at different fields by acquiring a series of images with various T_{evol} increasing the overall measurement time by the total number of needed T_{evol} and evolution fields. For example, a series of 10 images is needed for 2 evolution fields ($B_0 \pm \Delta B_0$) and 5 T_{evol} per field. In comparison, for dreMR imaging in (b) only one T_{evol} is needed, which is chosen in the order of T_1 to maximise SNR, therefore the overall measurement time can be reduced to the acquisition time of 2 images needed for image subtraction.

2.4 Potential applications

2.4.1 Contrast-to-noise ratio

While SNR is important to characterise an MRI system, contrast-to-noise ratio (CNR) is what ultimately determines the usefulness of an image. We define CNR here as how much the SNR varies with respect to an underlying physical parameter of interest. In MRI, the sources of contrast mainly rely on T_1 and T_2 at fixed B_0 field. In FFC-MRI, the source of contrast up to now has mainly been based on T_1 dispersion. For instance, considering a polynomial expansion of R_1 around the magnetic field B_0 as $R_1 = R_{10} + \beta \Delta B_0$, where R_{10} is the relaxation rate at the field B_0, and β the slope of the dispersion profile, one possible dreMR-related CNR could be:

$$CNR = \frac{\Delta SNR}{\Delta B_0}. \tag{2.6}$$

Indicating that dreMR contrast is maximized when the slope of the signal is the largest. Considering an inversion-recovery sequence, where the signal equation is proportional to $1 - 2e^{-R_1 T_{evol}}$ with T_{evol} the evolution time, in first approximation, the CNR, corrected from thermal equilibrium will vary as a function of βT_{evol}. Reciprocally, the CNR as a function of β is linked to the product $\Delta B_0 T_{evol}$, such that larger field offsets and longer application times are more sensitive.

Besides T_1, T_2 dispersion may also be of interest. However, it is technically difficult to maintain phase coherence while switching the magnetic field. Initial work has been done to access R_2 dispersion profiles in FFC-MRI systems [53], with the major target of endogenous ferritin imaging [54] that, as a major component of iron metabolism, may represent a biomarker of neurodegenerative diseases.

It is important to consider that T_1 varies significantly between different magnetic fields. This effect is more pronounced in tissues that disperse strongly, such as cartilage or muscle, and less so in fatty tissues or brain. Other effects may influence the contrast such as quadrupolar relaxation, as explained later. Therefore, CNR using FFC-MRI varies depending on the field strength that can be accessed, and therefore on the technology employed, and its evaluation and benefits for biomedical applications is widely unexplored. Here we present some contrast mechanisms accessible by the FFC-MRI systems presented here.

2.4.2 Quadrupole peaks due to ^{14}N-^{1}H cross-relaxation

The presence of cross-linked proteins in tissues may result in local increases in the R_1 relaxation rate in the dispersion curves of protons at particular magnetic fields, around ^{1}H Larmor frequencies of 600 kHz, 2.2 MHz and 2.8 MHz, respectively. This quadrupole cross-relaxation effect has been first reported in living biological tissues by Kimmich et al. [55] and is now relatively well understood as being due to a transfer of magnetisation between water protons and the ^{14}N nuclei, probably from amine and/or amide groups of

protein backbones, even though the transfer mechanism from the protein proton to the bulk water is still a topic of debate. Nevertheless, efficient models exist that allow predicting this so-called quadrupole relaxation enhancement (QRE) for an arbitrary quadrupole spin number [56].

QRE from ^{14}N is an interesting source of contrast since it is naturally found in vivo and it directly informs on the presence of immobilised proteins. Experiments on cross-linked albumin [57] or the fibrin system [12] showed that the amplitude of the peak is directly proportional to the concentration of the protein responsible for the relaxation enhancement, which makes this a quantitative biomarker. However, experimentation on biological tissues have so far only found the same pattern of peaks, so this signal does not discriminate between different sources and does not inform on the nature of the protein responsible for it. Another important aspect of the ^{14}N quadrupole peaks is that they appear at relatively low magnetic fields so that they are not accessible by high-field insert technologies such as those used for dreMR.

Experiments with FFC-MRI scanner and FFC-NMR relaxometer have shown interesting applications for the ^{14}N quadrupole signals in muscle atrophy [58] and osteoarthritis [13, 59]. In both pathologies, the amplitude of the peaks informs on the protein structures, which relates to the pathology.

2.4.3 Dispersive contrast agents for FFC-MRI

The fact that some MRI contrast agents show a strong dependence of R_1 upon the magnetic field can be exploited by FFC-MRI [60–62]. The idea is to acquire one image (or even a relaxometric R_1 map) for an evolution field where the probe shows a high relaxivity, and another one with an evolution field corresponding to a low relaxivity. In this way one can obtain image contrast based on the slope dR_1/dB_0 of the contrast agent's NMRD profile. In the low field range, FFC-MRI mainly relies on the large endogenous R_1 dispersion of biological tissues, which can show the aforementioned quadrupole peaks due to ^{14}N-^{1}H cross-relaxation, but can also benefit from the use of exogenous contrast agents. O'Hogain et al. [63] investigated the use of liposomes encapsulating paramagnetic Mn[II] ions as a tailored FFC-MRI contrast agent for low field applications. This probe shows a large difference in relaxivity values between 5 mT and 60 mT, whereas the reference sample displays almost no change in relaxivities over the same field range. In the high field range (above 0.5 T), R_1 dispersion of tissue becomes relatively invariant as several NMRD studies have emphasised [64, 65]. There is a relatively simple decrease of R_1 with field above 0.5 T, with proposed descriptions involving a macromolecular-based power law and a logarithmic term involving the restricted diffusive exploration of the macromolecular interfaces [66]. Endogenous R_1 dispersion properties can thus be characterized by a small number of parameters, including the slope of the dispersion profile around the central B_0 value, providing contrast sensitive to the macromolecular content, although there still are

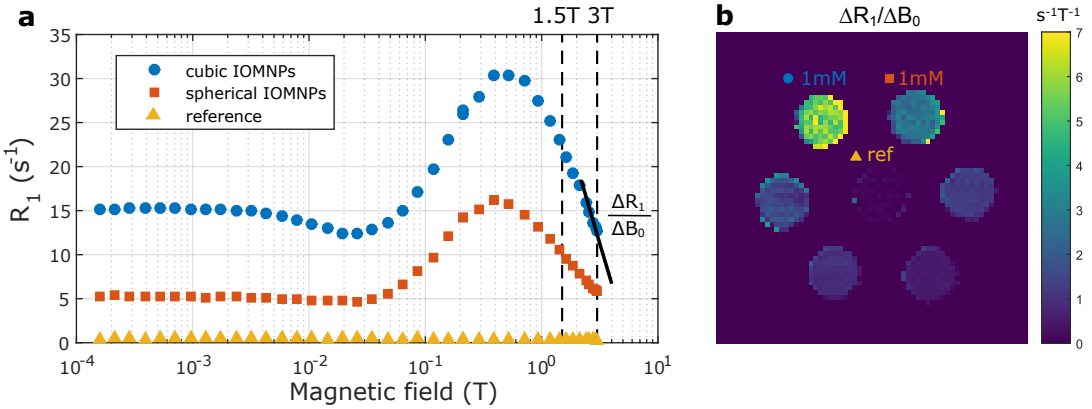

Figure 2.8: Comparison between FFC-MRI pulse sequences used for (a) quantitative $\Delta R_1/\Delta B_0$ mapping and (b) qualitative R_1 dispersion imaging in the case of dreMR imaging. In (a) R_1 mapping is performed at different fields by acquiring a series of images with various T_{evol} increasing the overall measurement time by the total number of needed T_{evol} and evolution fields. For example, a series of 10 images is needed for 2 evolution fields ($B_0 \pm \Delta B_0$) and 5 T_{evol} per field. In comparison, for dreMR imaging in (b) only one T_{evol} is needed, which is chosen in the order of T_1 to maximise SNR, therefore the overall measurement time can be reduced to the acquisition time of 2 images needed for image subtraction.

no in vivo studies exploiting this aspect with FFC-MRI.

To date, FFC-MRI for typical clinical-system field strengths (1.5 or 3.0 T) mainly relies on the use of contrast agents with a strong magnetic field dependency in the corresponding field-cycling range. Alford et al. [17] were the first to introduce the dreMR method for in vitro differentiation between the bound and unbound state of gadofosveset at 1.5 T. This probe exhibits a strong R_1 dispersion upon activation by binding to large molecules such as serum albumin but shows weak R_1 dispersion in the unbound state. Araya et al. [47] conducted in vivo experiments with mice demonstrating an unambiguous localization of gadofosveset activated by protein binding. Hoelscher et al. [18] extended these results by quantitative measurements of concentration using the dispersive contrast agent Gadofluorine M. Furthermore, it was shown by Bödenler et al. [31] that iron oxide magnetic nanoparticles (IOMNPs) are suitable for in-vitro FFC-MRI studies up to 3 T. The corresponding NMRD profiles, as illustrated in Figure 2.8a, exhibit a sufficiently high $\Delta R_1/\Delta B_0$ to perform dreMR imaging or relaxometric mapping in the field-cycling range of 2.89 T$\pm$0.1 T (Figure 2.8b). All these results demonstrate the potential of FFC-MRI in the field of contrast agents, to improve the sensitivity and specificity of contrast agent detection over a wide range of field strengths. Although approximately 40 % of clinical MRI exams employ Gadolinium-based CAs [67], the availability of clinical approved CAs suitable for FFC-MRI is rather limited. The aforementioned gadofosveset was designed as blood pool agent for contrast-enhanced MR angiography and is approved for a clinical use [68]. This agent shows favourable dispersive properties in the clinical field range between

1.5 T and 3 T, but the manufacturer discontinued the production in 2017 [69]. Iron oxide nanoparticles also show dispersive properties in the clinical field range. For example, ferumoxytol is approved by the United States Food and Drug Administration (FDA) for treatment of iron deficiency anemia in adult patients and its off-label use as MRI contrast agent has rapidly grown [70, 71]. Over the years, significant effort has gone into the development of new MRI contrast agents but sophisticated toxicology and pharmaceutical investigations are necessary to take the step from preclinical development to approval for clinical use.

One important means to determine the suitability of contrast agents for FFC-MRI is the measurement of the ^{1}H R_1 NMRD profile by FFC-NMR relaxometry. For paramagnetic systems the shape of the NMRD profile is influenced by various parameters such as the water exchange rate, coordination number, rotational correlation time and electron spin relaxation [60]. As already shown with the protein-binding gadofosveset, the most promising for FFC-MRI are slowly tumbling systems where the reorientational correlation time τ_R becomes long. This leads to a relaxivity peak located between 20 and 80 MHz followed by a steep downward slope which can be exploited by a clinical FFC range. In future, it may be possible to design contrast agents specific for FFC-MRI by aiming for extremely high $\Delta r_1/\Delta B_0$ in the activated state and almost no $\Delta r_1/\Delta B_0$ in the inactivated state.

2.4.4 Potential frequency-selective contrast agents for FFC-MRI

A promising alternative to the currently used contrast agents for FFC-MRI is the design of frequency-selective molecular probes based on QRE. The idea is to utilise QRE between water protons and exogenous quadrupole nuclei, similar to the aforementioned interaction between endogenous ^{1}H and ^{14}N in the amide groups of proteins at low field strengths. QRE becomes effective if the ^{1}H Larmor frequency matches one of the frequencies with high transition probability of the quadrupole nuclei, a condition which depends on the Quadrupole Coupling Constant Q_{cc}, the asymmetry parameter η and the Zeeman splitting [72]. Q_{cc} and η are the main parameters describing the frequency positions of the nuclear quadrupole spin transitions of a QRE active molecule. Consequently, QRE based contrast agents show a frequency-selective nature, similar to the quadrupole peaks due to ^{14}N-^{1}H cross-relaxation.

For instance, several compounds containing high spin quadrupole nuclei such as ^{209}Bi show very characteristic QRE patterns in the field range between 0.5 T and 3 T, as was recently shown by Kruk et al. [73] in NMRD studies of solid powder samples. For the envisaged aim of an exogenous QRE contrast agent, one would require, in a next step, to show QRE in the liquid state by grafting these core compounds onto nanoparticles and dissolve them in an aqueous solution. The relaxation dynamics of QRE in the liquid state can be simulated by the stochastic Liouville approach [72, 74, 75]. As an example, a simulated NMRD profile for a possible QRE contrast agent is displayed in Figure 2.9

for tris(2-methoxyphenyl)bismuthane. Several QRE peaks emerging up to 3 T indicate the potential to exploit this frequency-selective nature with FFC-MRI to enhance image contrast. Moreover, the overlay with FFC ranges of currently available FFC-MRI systems clearly shows the benefit of a wide variety of cycling ranges as it is completely unexplored at which field strength such compounds lead to the best image contrast. Another interesting consideration is that the Q_{cc} is sensitive to structural changes in the chemical surrounding of the quadrupole nuclei. It is possible to tune the quadrupole transition frequency, and therefore the QRE effect, by attaching different substituents to the core compound. Recently, Gösweiner et al. [76] showed the tuning possibilities of the resonance condition for various Bi-aryl compounds. Although current research is focusing on ^{209}Bi as core compound, it is also conceivable to use other quadrupole nuclei to design QRE based contrast agents specific for a FFC range of choice.

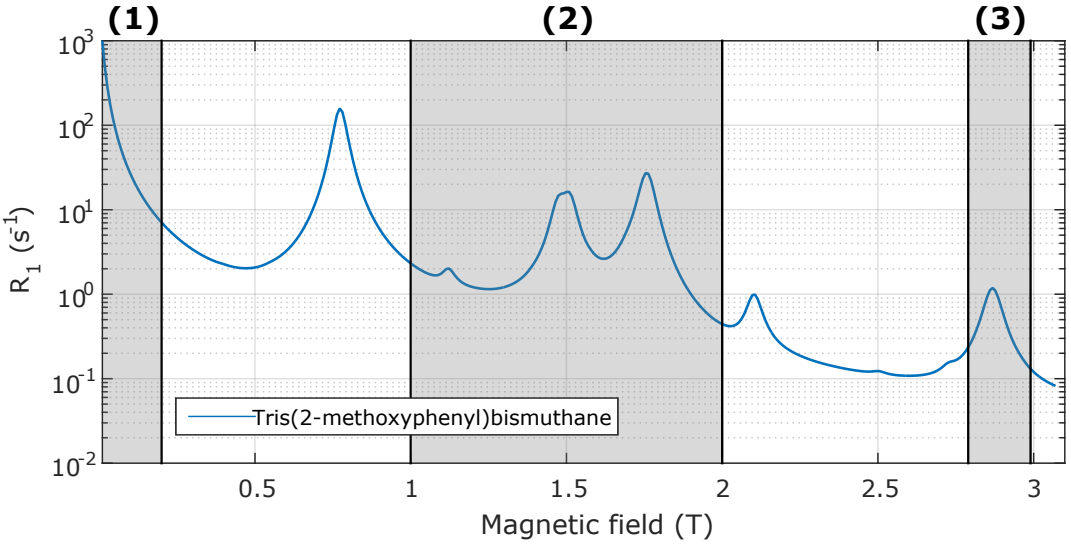

Figure 2.9: ^{1}H R_1 NMRD profile of a potential QRE based contrast agent simulated with the stochastic Liouville approach for a rotating, coupled system ^{209}Bi-^{1}H with a rotational correlation time of 300 ns, inter-nucleus distance of 2 $\AA$, Q_{cc} of 715 MHz and $\eta = 0$ (parameters taken from [76]). The grey overlay illustrates achievable FFC ranges of different FFC-MRI systems: (1) up to 0.2 T [35] (2) 1.5 T ± 0.5 T [30] and (3) 2.89 T ± 0.1 T [31].

2.4.5 FFC-MRI on biological tissues

Thanks to the recent technological improvements of FFC-MRI systems leading to exploitable image quality, initial in-vivo biomedical imaging applications are emerging. Figure 2.10 and Figure 2.11 display typical images obtained with clinical and preclinical systems with anatomical targets such as brain, musculoskeletal and abdominal regions, and current pathological targets that mostly focused on cancer. These examples illustrate the excellent image quality that FFC-MRI can provide, and initial biomedical evaluation of the translation from FFC-NMR to FFC-MRI. In the future, it is expected that the suc-

cessful biological applications of FFC-NMR [14] will be translated to FFC-MRI, leading to new imaging biomarkers of diseases that still remain to be validated and compared to the already rich contrast available on conventional fixed-field MRI systems.

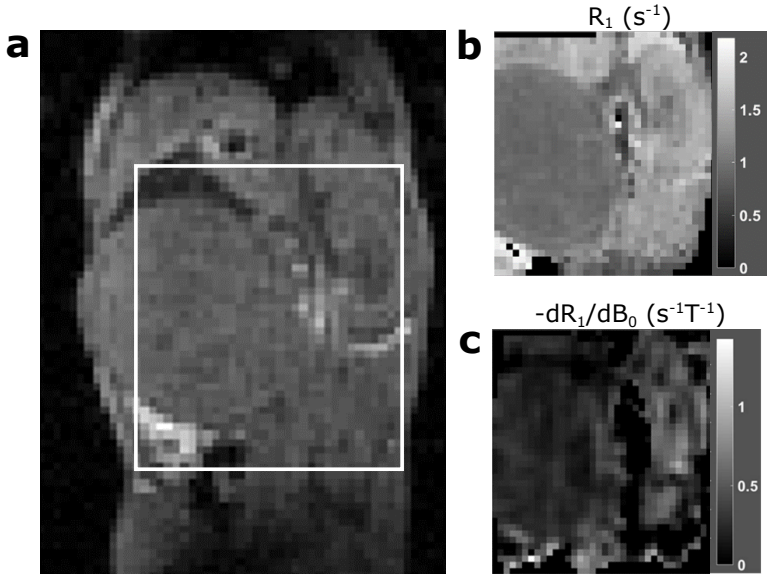

Figure 2.10: In vivo FFC-MRI measurements in a kidney tumor mouse model obtained from the preclinical insert system operating at 1.5 T ± 0.5 T [77]. (a) Standard spin-echo T_1-weighted image (0.5 mm isotropic in-plane and 2.5 mm through-plane resolution, acquisition time per image is 5 min) of the abdomen of a mouse acquired at 1.5 T. (b) R_1 map at 1.5 T corresponding to the white square in (a). (c) Corresponding dispersion ($-dR_1/dB_0$) map calculated for three different field strengths of 1.34 T, 1.5 T and 1.66 T. The tumor displays lower R_1 and $-dR_1/dB_0$ than the medulla and kidney.

2.5 Conclusions

Fast Field-Cycling provides a wealth of information at a molecular level and pioneer works on FFC-MRI show promising results, but also additional technical complexity. The compromises that have to be made to develop FFC-MRI scanners have to balance field strength, B_0 bandwidth, scanner size, field stability and scan time. The technologies presented in this paper show several approaches that allow exploring different regions of the magnetic field strength and present different advantages and drawbacks.

Extending the measurement of the dispersion curve towards low magnetic fields is more easily performed using a single electromagnet, at the cost of degraded field stability. This may be mitigated by using detection methods at very low field and has the added benefit to provide near-immunity against ferromagnetic elements, at the cost of SNR and possible additional complexity. Fields ranging between several mT and 0.5 T can be probed using a combination of permanent and resistive magnets. This prevents field fluctuations during

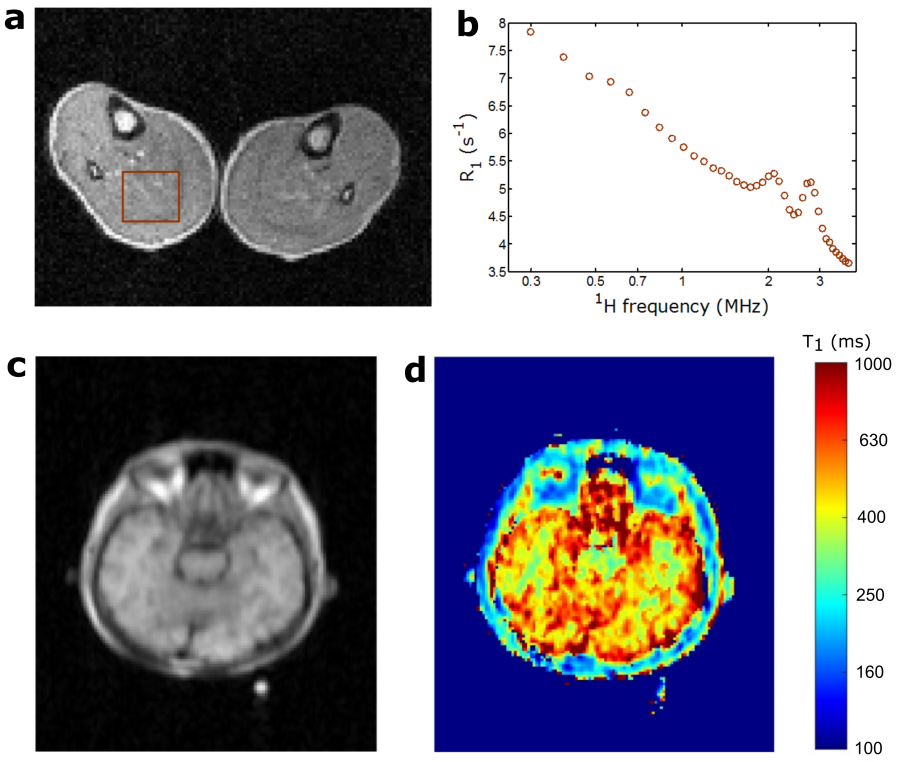

Figure 2.11: Data obtained from whole-body FFC-MRI scanners (from [58]). (a) 1 cm-thick section of thighs of a healthy volunteer, obtained at 59 mT from the dual-magnet system presented in [34]. Relaxometry was performed using FC-PRESS over a volume of interest to provide dispersion curves (b). (c) Spin echo image from a healthy volunteer's head obtained at 0.2 T from the resistive magnet presented in [35] (32 ms echo time, polarisation at 0.2 T for 0.3 s, 6 mm slice thickness, 2.3 mm in-plane resolution, 0.3 s recycle delay at Earth field). The T_1 map at that field is shown in (d); it clearly shows the difference between grey matter, white matter, and fatty tissues.

readout but limits the lowest field attainable. T_1 dispersions at high magnetic fields can be measured using a combination of resistive insert coils and superconducting magnets. This provides high SNR and resolution, at the cost of lower usable volume and lower B_0 bandwidth.

These various technical solutions allow covering a wide range of the magnetic field spectrum and collaborative work is now possible to explore T_1 dispersion contrast mechanisms over 5 decades of B_0, from 20 μT to 3 T. This opens new research avenues for the discovery of biomarkers as well as to better understand pathological processes at the molecular level. In conclusion, FFC-MRI is emerging as a powerful research tool readily available, and future developments may enable exploring its large potential for biomedical applications.

3

R_1 Dispersion Contrast at High Field with Fast Field-Cycling MRI

Markus Bödenler[1], Martina Basini[2], Maria Francesca Casula[3], Evrim Umut[4], Christian Gösweiner[1], Andreas Petrovic[1], Danuta Kruk[4], and Hermann Scharfetter[1]

[1] Institute of Medical Engineering, Graz University of Technology, Austria
[2] Physic Department and INSTM, Università degli Studi di Milano, Italy
[3] Department of Chemical and Soil Sciences and INSTM, University of Cagliari, Italy
[4] Faculty of Mathematics & Computer Science, University of Warmia & Mazury, Poland

Published in:
Journal of Magnetic Resonance 290 (2018) 68-75
https://doi.org/10.1016/j.jmr.2018.03.010

Abstract

Contrast agents with a strong R_1 dispersion have been shown to be effective in generating target-specific contrast in MRI. The utilization of this R_1 field dependence requires the adaptation of a MRI scanner for fast field-cycling (FFC). Here, we present the first implementation and validation of FFC-MRI at a clinical field strength of 3 T. A field-cycling range of ±100 mT around the nominal B_0 field was realized by inserting an additional insert coil into an otherwise conventional MRI system. System validation was successfully performed with selected iron oxide magnetic nanoparticles and comparison to FFC-NMR relaxometry measurements. Furthermore, we show proof-of-principle R_1 dispersion imaging and demonstrate the capability of generating R_1 dispersion contrast at high field with suppressed background signal. With the presented ready-to-use hardware setup it is possible to investigate MRI contrast agents with a strong R_1 dispersion at a field strength of 3 T.

3.1 Introduction

As the name implies, fast field-cycling magnetic resonance imaging (FFC-MRI) is the combination of fast field-cycling nuclear magnetic resonance (FFC-NMR) relaxometry with imaging methods of MRI and is based on cycling the B_0 field within an imaging sequence [28]. This gives access to new types of contrasts arising from the field dependency of the ^1H relaxation rates R_1 and R_2, also termed as R_1 and R_2 nuclear magnetic relaxation dispersion (NMRD), respectively. FFC-MRI can be implemented on clinical MRI systems by inserting an additional B_0 insert coil into an otherwise conventional scanner. This was previously realized for a clinical field strength of 1.5 T and is also referred to as delta relaxation enhanced magnetic resonance (dreMR) imaging [17, 18, 29, 78].

Alford et al. [17] demonstrated a differentiation between bound and unbound contrast agent (CA) using the targetable probe gadofosveset which only exhibits a strong R_1 dispersion upon binding to serum albumin. This leads to an improved target specificity by exploiting image contrast based on the increased dR_1/dB_0 of the bound CA instead of the absolute difference of the relaxation rate at a fixed magnetic field. Therefore, the dreMR image shows only contrast arising from the bound CA and supresses contrast from the anatomical background as well as from the unbound agent, which has been recently shown by in-vivo experiments with mice [47]. Hoelscher et al. [18] extended the dreMR theory to quantitative concentration measurements using a correction for finite ramp times during field-cycling and a compensation of field-cycling induced eddy current fields by dynamic reference phase modulation [45].

Whereas the R_1 dispersion of healthy tissue is large for low magnetic fields, in the range of clinical field strengths, the dispersion is inherently weak (e.g. $-0.19s^{-1}T^{-1}$ around 1.5 T for murine muscle tissue), as recent findings by Araya et al. [47] have emphasized. Therefore, the use of contrast agents exhibiting a strong dependence of R_1 upon the magnetic field i.e. a steep slope dR_1/dB_0 in the NMRD profile is favourable to obtain significant R_1 dispersion contrast. Up to now, all suitable CAs for dreMR utilize a preferably steep slope in the NMRD profile. An interesting alternative for dreMR imaging at clinical fields could be the exploitation of extrinsic contrast agents based on quadrupole relaxation enhancement (QRE). High spin quadrupole nuclei (QN) such as ^{209}Bi offer the potential of QRE peaks emerging in the clinical B_0 range instead of a smooth dispersion [79].

The cross-relaxation between water protons and quadrupole nuclei, i.e. nuclei with a spin quantum number $> 1/2$, gives rise to a shortening of the longitudinal proton relaxation time T_1. This so called quadrupole relaxation enhancement [72, 80, 81] offers a high potential for designing smart molecular probes for the usage as MRI contrast agents in the context of cellular and molecular imaging [79]. So far the effectiveness of QRE for increasing MRI contrast has been shown at low magnetic fields for the cross-relaxation between ^{14}N and ^1H in protein backbones [28, 82, 83]. However, this effect is entirely unexplored for the

design of extrinsic contrast agents at clinical field strengths such as 1.5 T or 3 T. QRE based CAs are frequency-selective as the cross-relaxation can only become effective if the proton Larmor frequency matches one of the transition frequencies of the QN [72]. This favourable feature offers the possibility to activate and inactivate QRE, and therefore image contrast, by modulating the magnetic field. The frequency position of QRE can either be altered by chemical interaction with the biological environment allowing for chemically selective contrasts or by shifting of the main B_0 field of the MRI system itself, namely FFC-MRI.

The validation and future application of QRE contrast agents at clinical fields requires a dedicated MRI system adapted for fast field-cycling. Although there exist a handful of 1.5 T systems worldwide, we show, to the best of our knowledge, the first FFC-MRI setup for a field strength of 3 T. To this end, the aim of this work is to present important steps for the implementation and validation of a small animal FFC-MRI system for 3 T by means of a B_0 insert coil. We describe the specification of our hardware setup and show a rather simple approach to overcome imaging artefacts due to random phase fluctuations induced by the output noise current of the gradient power amplifier. Furthermore, system validation is performed by FFC-NMR relaxometry measurements and proof-of-concept dreMR imaging of selected iron oxide magnetic nanoparticles (IOMNP). The final result is a ready-to-use FFC-MRI system for a clinical field strength of 3 T with the envisaged aim of exploiting the magnetic field dependency of MRI contrast agents in general and to investigate the imaging potential of prospective QRE compounds in particular.

3.2 Methods

3.2.1 Hardware setup

The field-cycling hardware was implemented on a clinical 3 T MRI system (Skyra, Siemens Healthineers, Germany) using a custom-built B_0 insert coil (Resonance Research Inc., USA). The insert coil has a resistance of 63.8 $m\Omega$ and an inductance of 1.69 mH. It is driven by a gradient power amplifier (IECO, Finland) capable of a maximum continuous output current of ±150 A (±300 A peak) and a field efficiency of 0.668 mT/A. This allows for an offset field ΔB_0 of ±100 mT within a minimum ramp time of 1 ms. Field inhomogeneities are less than 1 % over a diameter of 35 mm in axial direction. Shielded design of the coil reduces the fringe field to 0.2 mT at the main magnet bore (radius of 35 cm). The insert is placed in the isocenter of the main magnet and holds a custom-built transmit/receive ^1H birdcage radio frequency (RF) coil (MRI.TOOLS GmbH, Germany) with variable tune and match capability. This enables an imaging region of 40 mm in axial and 40 mm in longitudinal direction, which is suitable for imaging of phantoms and small animals. The ΔB_0 pulses are generated with an arbitrary waveform generator controlled by an optical trigger signal from the MRI pulse sequence. This design ensures that there is no electronic coupling to the main magnet system.

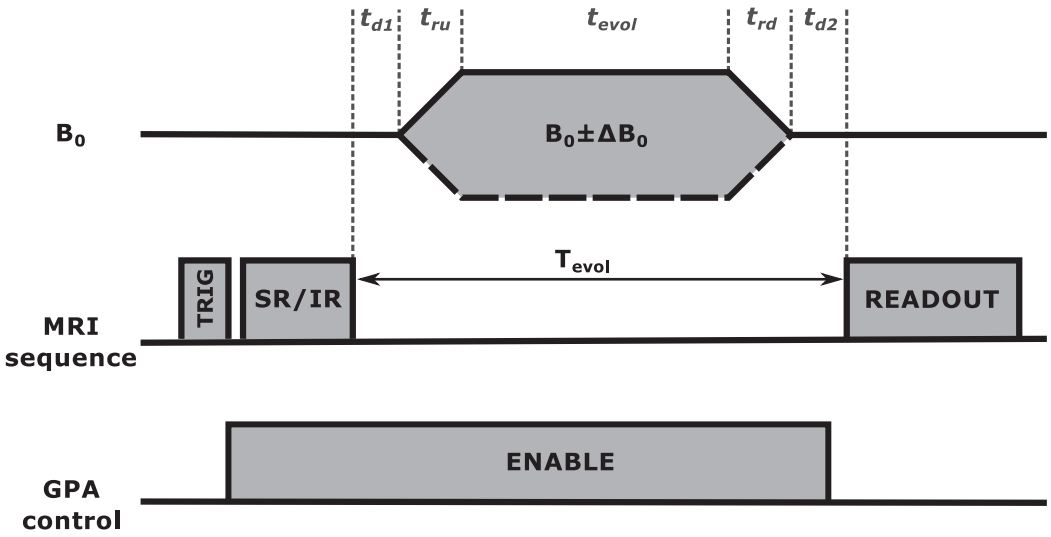

Figure 3.1: Schematic of a FFC-MRI pulse sequence with saturation (SR) or inversion (IR) magnetization preparation. The trigger (TRIG) synchronizes the B_0 insert coil with the MRI system. The ENABLE signal is used for blanking the GPA during image readout to prevent imaging artefacts due to random phase fluctuations. The timing of the ΔB_0 pulse is as follows: delay time after the preparation phase t_{d1}, ramp up and ramp down times t_{ru} and t_{rd}, respectively, flat top time t_{evol} and settling time t_{d2}. T_{evol} denotes the total time between magnetization preparation and image acquisition.

A basic FFC-MRI pulse sequence consists of a magnetization preparation such as an inversion (IR) or a saturation (SR) RF pulse followed by an evolution phase of duration T_{evol} with applied field shift $B_0 \pm \Delta B_0$ and subsequent signal acquisition at the nominal B_0 field. The trigger defines the timing of the ΔB_0 pulse within the pulse sequence synchronizing the B_0 insert coil with the MRI system. A schematic of the aforementioned timing is illustrated in figure 3.1 and thorough reviews of pulse sequences can be found in [18, 29, 46, 63].

Whereas magnetic field inhomogeneities in the order of 1 % during the evolution phase are not critical for FFC-MRI, the field stability during signal acquisition is crucial to prevent phase errors. In our case the output noise current of the gradient power amplifier (GPA) in the idle state induces random phase fluctuations during image acquisition causing serious ghosting artefacts in phase encoding direction. This problem has also been observed in other FFC-MRI systems [29, 38, 41]. Recently, a post-processing correction technique was proposed minimizing the background signal by determining the optimum phase correction for each line in k-space [41]. Another hardware based approach is to alternate the amplifier load between the B_0 insert coil and an inductance-matched dummy load using a fast high-power solid state switch [29]. Here, we choose an approach utilizing an additional synchronized TTL signal to the dedicated control input of the GPA. The GPA is only enabled during the evolution phase and disabled throughout image acquisition (see

ENABLE signal in figure 3.1) so as to suppress the output noise current sufficiently. There is, however, a timing restriction in the hardware of the GPA: According to the specifications there is a delay between the edges of the control signal for enable and disable and the physical response of the GPA output stage, i.e. about 20 ms (enable) and 2 ms (disable), respectively. Consequently, the trigger signal has to be sent earliest 2 ms prior to the rising edge of the actual ΔB_0 pulse to ensure a safe operation mode of the GPA.

To show the effectiveness of this approach, images were acquired with and without GPA blanking using a modified saturation recovery spin echo (SR-SE) sequence with the following parameters: repetition time TR = 1000 ms, echo time TE = 15 ms, T_{evol} = 150 ms, field of view FOV = 50 mm x 50 mm, matrix size 256 x 256, bandwidth BW = 130 Hz/Px, flip angle = 90° and slice thickness = 5 mm. No field shift was applied for these measurements.

3.2.2 Eddy current characterization and compensation

Eddy current related artefacts are a key challenge for FFC-MRI [29, 45], in particular, when two images with contrast from different B_0 field shifts are subtracted. Thus, the characterization and compensation of the spurious signal dynamics induced by the eddy current field is crucial. Fast ramping of the offset field induces eddy currents in the main magnet structure of the MRI system. Though the B_0 insert coil is actively shielded to reduce the coupling to the main magnet system, the residual fringe field results in a temporally varying offset of the Larmor frequency. This offset gives rise to a rigid-body image shift in frequency and slice encoding direction.

The temporal behaviour of the eddy currents (i.e. the Larmor frequency shift) is characterized using a modified multi-phase spoiled gradient echo sequence [30]. A phantom holding six samples with different concentrations (two-fold serial dilution beginning with 1 mM) of the contrast agent Gadovist® (Bayer Vital GmbH, Germany) and a water reference sample was prepared. After an applied ΔB_0 pulse of +100 mT and T_{evol} of 300 ms a total number of 50 images (phases) were acquired with a repetition interval of 17 ms, resulting in a sampling duration of 850 ms during the eddy current decay. The remaining imaging parameters were as follows: TE = 8.5 ms, FOV = 50 mm x 50 mm, matrix size = 64 x 64, BW = 100 Hz/Px, flip angle = 15° and slice thickness = 5 mm. The ΔB_0 was cycled with a repetition time of 3000 ms. Mono- and bi-exponential decay curves were fitted to the obtained frequency shift resulting in an accurate model of the eddy current decay.

During the acquisition of FFC-MRI images, eddy currents then are compensated by dynamic reference phase modulation (eDREAM) as proposed in [45]. This method can be directly implemented into the MRI pulse sequence and does not require any additional hardware adaptations. To validate the eDREAM implementation a reference image (without applied field shift) and an image at shifted B_0 (ΔB_0 of +100 mT and T_{evol} of 300 ms) of the aforementioned Gadovist® phantom were acquired, respectively, using a modified SR-SE sequence with parameters: TR/TE = 3000/15 ms, FOV = 50 mm x 50 mm, matrix

size = 256 x 256, BW = 130 Hz/Px, flip angle = 90° and slice thickness = 5 mm. The shifted image was normalized to account for the different equilibrium magnetizations [18] and the difference image was obtained by magnitude subtraction of the reference image and shifted image.

3.2.3 Dispersive contrast agent for 3 T and FFC measurements

In order to validate the implementation of the FFC-MRI hardware setup, the availability of a contrast agent exhibiting strong R_1 relaxation dispersion at 3 T is crucial. Recently published iron oxide magnetic nanoparticles [84] were selected for system validation because of a suspected R_1 dispersion at 3 T. Such IOMNPs are obtained by a high temperature surfactant-assisted chemical route which leads to size- and shape- controlled nanocrystals. IOMNPs with similar average size (nearly 8 nm) and with different shapes (spherical and cubical) were used dispersed in hexane, and will be referred to as S8_hex and C8_hex, respectively. Samples containing three different concentrations (1 mM, 0.5 mM and 0.25 mM) for each shape and a hexane reference were prepared and arranged as illustrated in Figure 3.6a. The samples were investigated by Transmission electron microscopy (TEM) on an H-7000 Microscope (Hitachi, Japan) equipped with a W gun operating at 125 kV. Fe concentration in the dispersion was assessed by quantitative analysis through inductively coupled plasma atomic emission spectrometry using a Varian Liberty 200 ICP-AES (Agilent Technologies, USA).

^1H R_1 NMRD measurements were performed for the 1 mM samples and the hexane reference sample by using a Spinmaster FFC 1 T relaxometer (Stelar, Italy) for a Larmor frequency range of 10 kHz-30 MHz. An external HTC-110 3 T superconducting magnet equipped with a standalone PC-NMR console (Stelar, Italy) was used for a frequency range of 40 MHz-128 MHz. For measurements between 10 kHz-40 MHz one-pulse FFC sequences were used: Below 10 MHz the sample is pre-polarized at a field of 0.57 T and then the magnetic field is cycled to a different value, where the spin system is allowed to relax for a variable time period. Finally, the field is cycled back to the detection value, where the FID is recorded following the application of a 90° RF pulse. Above 10 MHz, where the signal is reasonably higher than at low field, the same procedure was followed except prepolarization was omitted. For measurements between 40-128 MHz a standard inversion recovery sequence was used. Furthermore, additional points were measured at 119 MHz, 123.2 MHz and 127.4 MHz corresponding to the achievable field cycling range (2.89 T ± 100 mT) of the B_0 insert coil.

Images were acquired with the FFC-MRI system at three different field strengths (2.79 T, 2.89 T and 2.99 T) and various evolution times (T_{evol} = 60, 100, 150, 300, 500, 800, 1500 and 3000 ms) using a modified SR-SE sequence. The remaining imaging parameters were: TR/TE = 10000/15 ms, FOV = 40 mm x 40 mm, matrix size = 64 x 64, BW = 130 Hz/Px, flip angle = 90° and slice thickness = 5 mm. For each field strength, R_1 maps were

estimated on a pixel-by-pixel basis by nonlinear fitting to a mono-exponential saturation recovery model [85]. In addition, a $\Delta R_1/\Delta B_0$ map was calculated by subtracting R_1 maps obtained for 2.99 T and 2.79 T.

3.2.4 DreMR signal simulation

In general, the behaviour of the magnetization in presence of an external magnetic field can be described by the Bloch equations. In the case of field-cycling, the main magnetic field B_0 is modulated throughout the pulse sequence and thus is a function of time. As the equilibrium magnetization M_0 and the longitudinal relaxation rate R_1 depend on B_0, they exhibit also a time-dependent behaviour requiring a numerical solver for the Bloch equations. However, under several assumptions for the waveform of the ΔB_0 pulse, closed-form solutions exist for the longitudinal magnetization M_z [63, 82]. To predict the behaviour of M_z as a function of the evolution time and for different field shifts we slightly adapted the proposed equation in [63] for saturation recovery and an additional delay time before the applied field shift. The common used linear ramps can be approximated by a step response with relaxation for half of the time at the nominal field and the other half at the desired field shift. The change in M_0 and R_1 can be assumed to be linear with respect to ΔB_0 within the field-cycling range. This gives a full description of the magnetization behaviour $M_z^{\pm}$ under consideration of the underlying timing restrictions in a FFC-MRI pulse sequence:

$$\begin{aligned} M_z^{\pm}(t_{evol}) = M_0 \; + \\ \left\{ M_0^{\pm} - M_0 - \left\{ M_0^{\pm} - M_0 + \alpha M_0 \exp\left[-\left(\frac{t_{ru}}{2} + t_{d1} \right) R_1 \right] \right\} \right. \\ \left. \exp\left[-\left(t_{evol} + \frac{t_{ru} + t_{rd}}{2} \right) R_1^{\pm} \right] \right\} \exp\left[-\left(\frac{t_{rd}}{2} + t_{d2} \right) R_1 \right], \end{aligned} \tag{3.1}$$

$$\text{where} \qquad M_0^{\pm} = M_0 \left(1 \pm \frac{\Delta B_0}{B_0} \right). \tag{2}$$

M_0 and $M_z^{\pm}$ are the equilibrium magnetizations, R_1 and $R_1^{\pm}$ the relaxation rates at nominal and shifted B_0 field, respectively. The superscript $\pm$ indicates whether a positive or negative field shift is applied. For saturation recovery the parameter α should be equal to 1, t_{d1} is the delay time between saturation pulse and begin of the ramp up time t_{ru}, t_{rd} is the ramp down time, t_{evol} is the flat top time and t_{d2} is the settling time after the ΔB_0 pulse. T_{evol} is given by the total time between magnetization preparation and begin of the image acquisition. This timing of ΔB_0 within the pulse sequence is illustrated in 3.1. Exemplarily, we simulated the relaxation curves for a positive and negative field shift

of ±100 mT for the sample containing 0.5 mM of cubic-shaped IOMNPs (ROI 2 in Figure 3.6a). The estimated R_1 values as well as M_0 from the aforementioned measurements were used for the simulation. The timing parameters of the ΔB_0 used for simulation were as follows: t_{d1} = 9 ms, $t_{ru} = t_{rd}$ = 1 ms, t_{d2} = 9.78 ms and t_{evol} was increased in 0.01 ms steps to span the desired simulation range (up to 3000 ms). In a next step, the simulated relaxation curves were compared to the measured curves. All curves were normalized to account for different equilibrium magnetizations and effective offset fields as proposed in [18]. Furthermore, the difference between M_z^+ and M_z^- relaxation curves was calculated resulting in the corresponding dreMR signal.

3.2.5 DreMR imaging

Images at $B_0 + \Delta B_0$ (2.99 T) and $B_0 - \Delta B_0$ (2.79 T) were acquired to demonstrate the feasibility of generating contrast based only on dispersive properties of the contrast agent. The imaging parameters of the modified SR-SE sequence were as follows: t_{evol} = 150 ms, TR/TE = 3000/15 ms, FOV = 40 mm x 40 mm, matrix size = 192 x 192, BW = 130 Hz/Px, flip angle = 90° and slice thickness = 5 mm. In order to maximize the contrast in the dreMR image the evolution time T_{evol} should be chosen to match approximately the sample's T_1 [18]. Again, all images were normalized prior to magnitude subtraction obtaining the final dreMR image.

3.3 Results and Discussion

3.3.1 Hardware setup

Figure 3.2a shows ghosting artefacts which arose when the GPA was left enabled during image acquisition. They appeared only in phase encoding direction due to the random phase fluctuations caused by the output current noise of the GPA. The GPA blanking eliminates all visible ghosting artefacts and a well-resolved image of the phantom can be obtained (Figure 3.2b). In addition to the intrinsic timing restrictions, i.e., 20 ms for enable and 2 ms for disable, the GPA noise might interfere with the magnetization preparation module if an overlap with the RF pulse occurs. Hence, the beginning of the trigger signal must be timed accordingly to prevent such interferences. Figure 3.3 shows the measured timing between trigger and begin of the field-shift including the onset of increased output noise once the GPA is enabled.

This required delay time was included in equation (3.1) as t_{d1} to account for a relaxation with B_0 prior the actual begin of the field shift. The GPA blanking approach is rather easy to implement as it utilizes the available control input of the GPA and requires only one additional TTL signal. Of course, the implementation is restricted to amplifiers providing such a dedicated control input and sufficient short enable and disable times. The inherent timing delays can be considered during the design and programming of the FFC-MRI pulse

sequence and are not a limiting factor for the FFC-MRI sequences discussed here as the TR is usually much longer than the enable time. However, for other types of sequences, e.g. with very short repetition times, i.e. in the range of the enable time (i.e. 20 ms), other correction methods like in [29, 41] must be used.

The imaging region of the presented B_0 insert coil is limited to phantom and small animal applications. Significant effort has gone into the construction of a fully commissioned human-scale FFC-MRI system with a maximum field strength of 0.2 T [35]. The inherently present R_1 dispersion in this field cycling range may have applications in the early diagnosis of a range of disease [13, 86]. For dreMR imaging there exist feasibility studies of B_0 insert coils designed for human head and prostate imaging [39, 40], which is an important step towards clinical applications at high field.

3.3.2 Eddy current characterization and compensation

The measured frequency shift induced by the eddy currents after a positive ΔB_0 pulse is shown in Figure 3.4a for an amplitude of 100 mT, ramp times of 1 ms and an evolution time of 300 ms. Fitting of a mono-exponential model resulted in a model amplitude of 367.6 Hz and a time constant of 169.3 ms with 95% confidence intervals (CI) of [359.4 Hz, 375.8 Hz] and [164.2 ms, 174.9 ms], respectively. Fitting of a bi-exponential model resulted in a slow and fast decaying component with amplitudes of 336.2 Hz and 97.6 Hz and with time constants of 183.6 ms and 17.8 ms, respectively. The CIs were [331.0 Hz, 341.5 Hz] and [87.5 Hz, 107.8 Hz] for the amplitudes and [180.9 ms, 186.4 ms] and [14.8 ms, 22.4 ms] for the time constants, respectively. The bi-exponential model with an adjusted R^2 value of 0.9996 performs better than the mono-exponential model with an adjusted R^2 value of 0.9951. The better fit can be seen notably at the beginning of the eddy current decay curve in 3.4a, i.e. in the time interval where the eddy current characterization is crucial for the eDREAM compensation. Given this more accurate description in the beginning of the eddy current decay the bi-exponential model was used for the eDREAM implementa-

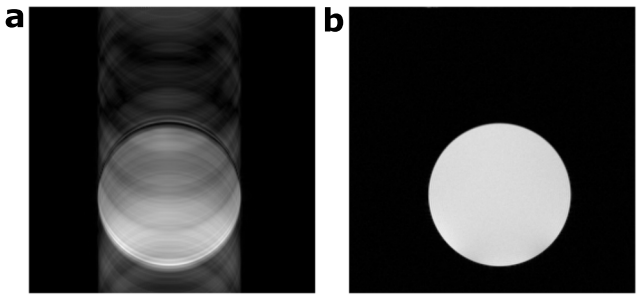

Figure 3.2: (a) Random phase fluctuations induced by the output current noise of the GPA cause severe ghosting artefacts in phase encoding direction. (b) Disabling the GPA during image acquisition eliminates all visible artefacts.

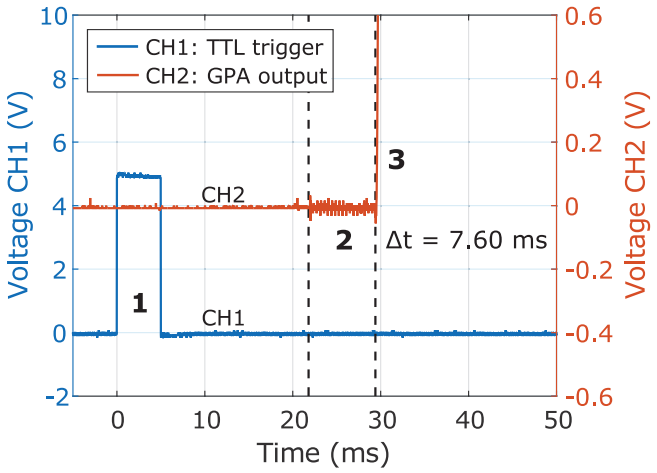

Figure 3.3: Measured timing of the TTL trigger signal (CH1, lower trace) and the voltage proportional to the output current of the GPA (CH2, upper trace). The rising edge of the B_0 waveform (3) occurs 24.5 ms after the end of the trigger pulse (1). The cursors indicate the interval (2) between GPA enable and the rising B_0 edge. The increased noise level in this phase is clearly visible and has a duration of $\Delta t = 7.60$ ms.

tion. The uncompensated eddy current effects lead to a rigid-body image shift in frequency and slice encoding direction causing severe artefacts when calculating the difference between reference image and shifted image (Figure 3.4b). The eddy current artefacts are completely removed by using the eDREAM compensation with the bi-exponential model (Figure 3.4c). As Gadovist®(Bayer Vital GmbH, Germany) has a negligible magnetic field dependence [87] in the achievable B_0 field-cycling range, no significant signal is expected in the difference image.

It is important to note that the dynamics of the eddy current field depend on several parameters of the ΔB_0 pulse such as amplitude, ramp up time, flat top time, ramp down time and repetition time. The results presented herein are exemplary for a field shift of 100 mT, equal ramp times of 1 ms each, a T_{evol} of 300 ms and a TR of 3000 ms. For different timing parameters a new characterization becomes necessary. It is to be expected that increasing the ramp times would lead to a decrease of the frequency shift due to a smaller dB/dt and hence lower eddy currents. Furthermore, a TR of 3000 ms is long enough (> 5 time constants) to allow for a sufficient eddy current decay before applying the next ΔB_0 pulse as can be seen in Figure 3.4a where the measured frequency shift has decayed below 3 Hz after 900 ms. Short TRs (< 5 time constants) lead to a formation of a dynamic steady state as the eddy current fields of the previous ΔB_0 pulse add to the field induced by the next ΔB_0 pulse. A comprehensive analysis of eddy current formation and the eDREAM compensation has been given by Hoelscher et al. in [45].

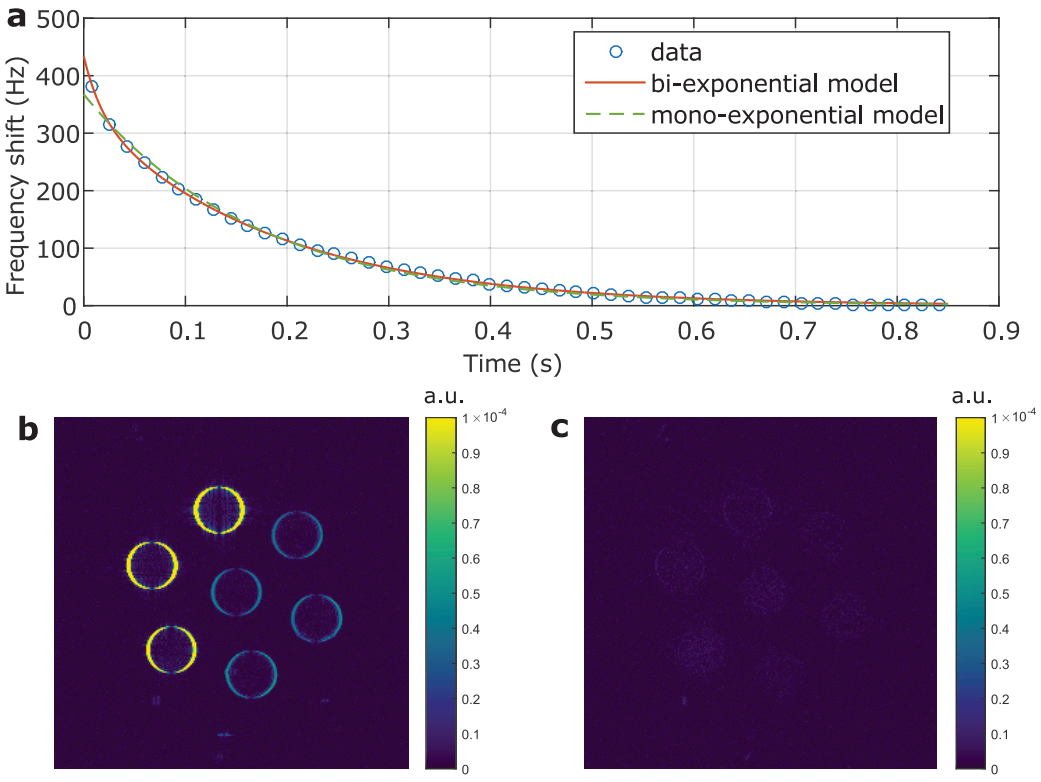

Figure 3.4: (a) Measured frequency shift induced by the eddy currents (blue circles) for a 100 mT ΔB_0 pulse with T_{evol} of 300 ms and a ramp times of 1 ms. A mono-exponential (green line) as well as a bi-exponential (red line) model were fitted to the data. This characterization of the eddy current field dynamics allows for a compensation by means of dynamic reference phase modulation. (b) Difference between reference image and image at shifted B_0 without eddy current compensation and (c) with compensation using the bi-exponential model.

3.3.3 Dispersive contrast agent for 3 T and FFC measurements

Both the cube-shaped as well as the spherically shaped IOMNPs proved to be suitable for system validation at a field strength of 3 T as they exhibit a pronounced peak in the NMRD profile (Figure 3.5) around 20 MHz followed by a steep downward slope in the targeted frequency range of 119-127.4 MHz corresponding to 2.89 T±100 mT. In contrast, the hexane sample shows only a weak dependence on the magnetic field i.e. a flat slope in the NMRD profile within the achievable field-cycling range and is therefore suited as a non-dispersive reference. Furthermore, for visual comparison of all samples, R_1 maps for 2.79 T and 2.99 T together with the corresponding R_1 dispersion map are shown in Figure 3.6b-d, respectively. The spherical IOMNPs (C8_hex) show higher R_1 values and a steeper slope of the NMRD profile (Figure 3.5) in comparison to the cubic IOMNPs (S8_hex). This is also emphasized by the R_1 dispersion map in Figure 3.6d, giving a good linear approximation of the slope in the NMRD profile within the achievable field-cycling

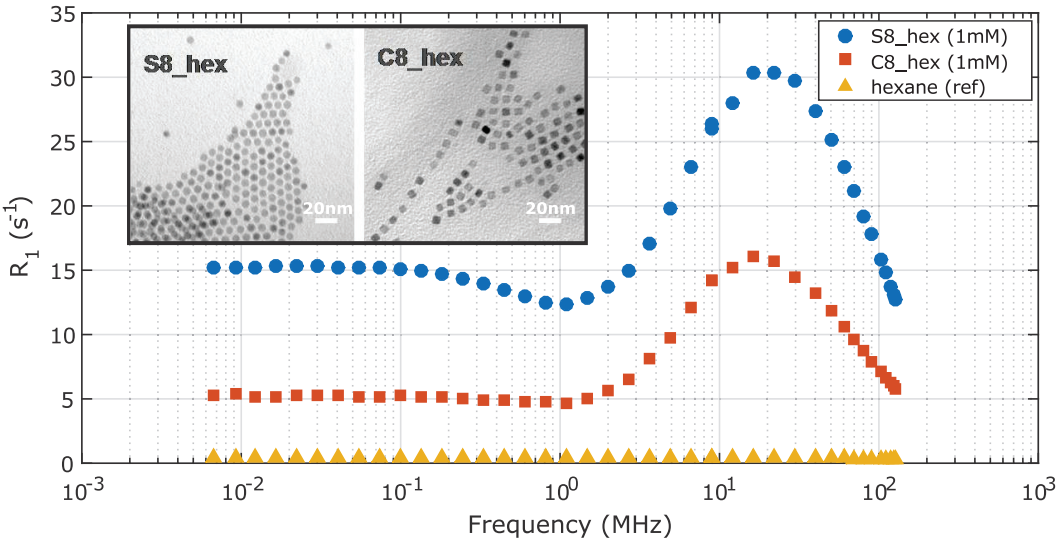

Figure 3.5: ^1H R_1 NMRD profiles of the cubic (C8_hex, red squares) and spherical (S8_hex, blue circles) IOMNPs with 1 mM concentration as well as of pure hexane (ref, yellow triangles) measured up to a field strength of 3 T (127.8 MHz) using a commercial FFC-NMR relaxometer. All measurements were performed at room temperature (295 K). The insets show representative TEM images of S8 and C8 samples, indicating that the used IOMNPs have different morphology and are nearly monodisperse in size and shape.

range i.e. $\Delta R_1/\Delta B_0$. As expected, no significant $\Delta R_1/\Delta B_0$ is visible in the R_1 dispersion map for the hexane reference sample.

Table 3.1: Comparison of R_1 at different field strengths measured with a commercial FFC-NMR relaxometer and with the proposed FFC-MRI system (mean ± standard deviation). For the FFC-MRI method, R_1 values were obtained by ROI analysis (rectangular ROI in the middle of each sample).

Sample	**Method**	**Longitudinal relaxation rates (s^{-1})**		
		2.79 T	2.89 T	2.99 T
S8_hex (1mM)	FFC-NMR	13.62 (±0.14)	13.17 (±0.13)	12.77 (±0.13)
	FFC-MRI	12.21 (±0.31)	11.63 (±0.34)	11.14 (±0.35)
C8_hex (1mM)	FFC-NMR	6.25 (±0.06)	6.07 (±0.06)	5.93 (±0.06)
	FFC-MRI	6.81 (±0.13)	6.54 (±0.14)	6.29 (±0.13)

Table 3.1 compares the R_1 values obtained with FFC-MRI measurements and the corresponding data points in the NMRD profile (2.79 T, 2.89 T and 2.99 T) for C8_hex and S8_hex IOMNPs samples with 1 mM concentration. In order to exclude pixels at the edges from the evaluation, the R_1 values have been estimated over a rectangular ROI in the middle of sample 1 and 4 in 3.6a. The R_1 estimation with the proposed FFC-MRI system is in accordance with the FFC-NMR measurements (Stelar, Spinmaster). Compared to the FFC-NMR measurements, the R_1 values obtained with FFC-MRI are slightly lower

for the S8_hex samples and slightly higher for the C8_hex samples with mean relative errors of -11.6% and +7.6%, respectively. It is likely that this systematic error results from different sample concentrations due to inaccuracies in the sample preparation and possible sample degradation during delivery to the FFC-NMR facility. Regardless of this error, the agreement between FFC-MRI and FFC-NMR measurements is sufficient for system validation.

All used IOMNPs were dispersed in hexane as they are produced by a synthetic route which leads to hydrophobic nanocrystals with high crystallinity and highest size and shape control achievable to date. The inset in Figure 3.5 reports representative TEM images of the C8 and S8 IOMNPs, showing that both samples are nearly monodisperse in size and shape. The use of the IOMNPs dispersed in an organic solvent is therefore justified for the validation of the proposed FFC-MRI system, because the signal-to-noise ratio (SNR) is important for an accurate characterization. Theoretically, it is possible to dissolve them in an aqueous solution, but this comes at the expense of losing R_1 dispersion [84]. The development of strategies for the dispersion in water without losing the beneficial relaxometric properties and achievable SNR, should be investigated in a separate study to

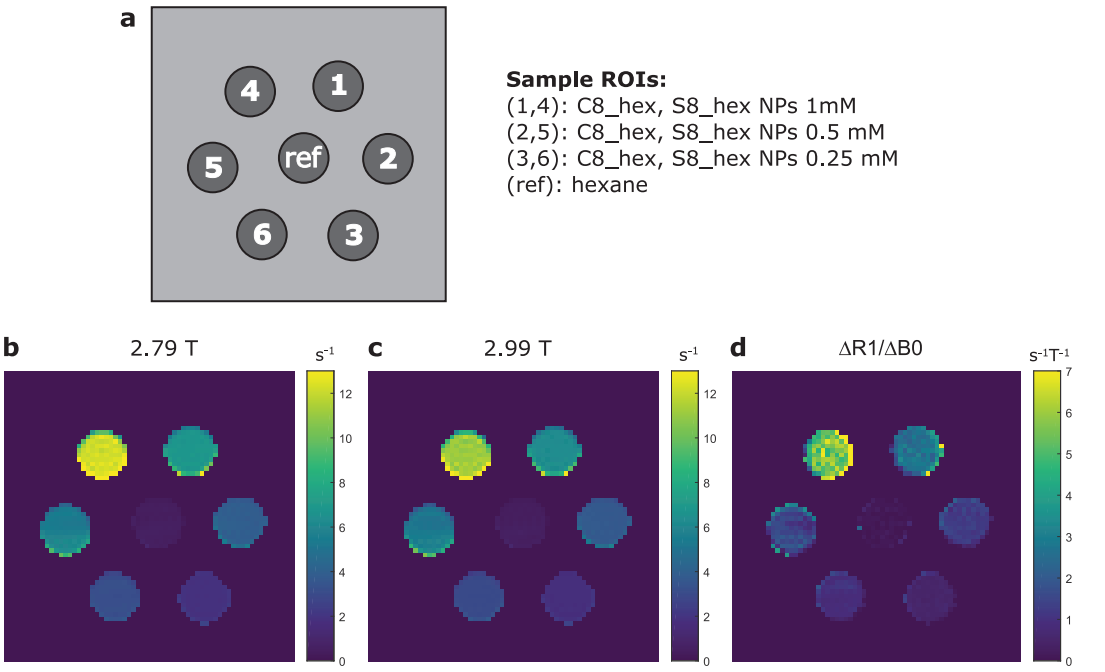

Figure 3.6: (a) Sample arrangement in the phantom containing three different concentrations of cubic (C8_hex) and spherical (S8_hex) IOMNPs as well as a non-dispersive hexane reference sample (ref). (b) and (c) show R_1 maps calculated on a pixel-by-pixel basis for a field strength of 2.79 T and 2.99 T, respectively. (d) R_1 dispersion map $\Delta R_1/\Delta B_0$ (magnitude) obtained from (b) and (c).

enable direct applicability of the IOMNPs to in-vivo experiments.

3.3.4 DreMR signal simulation

The behaviour of the longitudinal magnetization M_z in the presence of a trapezoidal field shift applied during the evolution phase was simulated using equation (3.1). Simulated relaxation curves (normalized to M_0) for a positive and negative field shift of 100 mT are shown in Figure 3.7a and compared to FFC-MRI measurement data for various evolution times (T_{evol} = 60, 100, 150, 300, 500, 800, 1500 and 3000 ms). The measured relaxation curves show a high degree of congruence with the simulation, which accounts for all underlying timing restrictions in the ΔB_0 pulse. The applied field shifts of ±100 mT result in a relaxation to different equilibrium magnetizations of $M_0^{\pm} = M_0 \pm 3.3$ %. Theoretically, a relaxation to $M_0^{\pm} = M_0 \pm 3.46$ % ($M_0(1 \pm \Delta B_0/B_0)$) is expected for a rectangular field shift without timing restrictions such as finite ramp times and delay times t_{d1} and t_{d2}. In order to isolate only the effect of R_1 dispersion in the dreMR signal a proper field-dependent scaling is of great importance as discussed by Hoelscher et al. in references [18, 88]. Figure 3.7b shows the characteristic dreMR signal (magnitude) obtained after subtraction of the relaxation curves for 2.79 T and 2.99 T. Prior to subtraction the relaxation curves were normalized to account for relaxation to different M_0 and effective offset fields. The measured data is in good agreement with the dreMR signal simulation after accounting for all timing restrictions. Furthermore, we observe a minimum (for negative $\Delta R_1/\Delta B_0$) located around the T_1 of the sample (ROI 2) which is approximately 267 ms. As dreMR images are based on image subtraction they suffer from a poor SNR. In order to maxi-

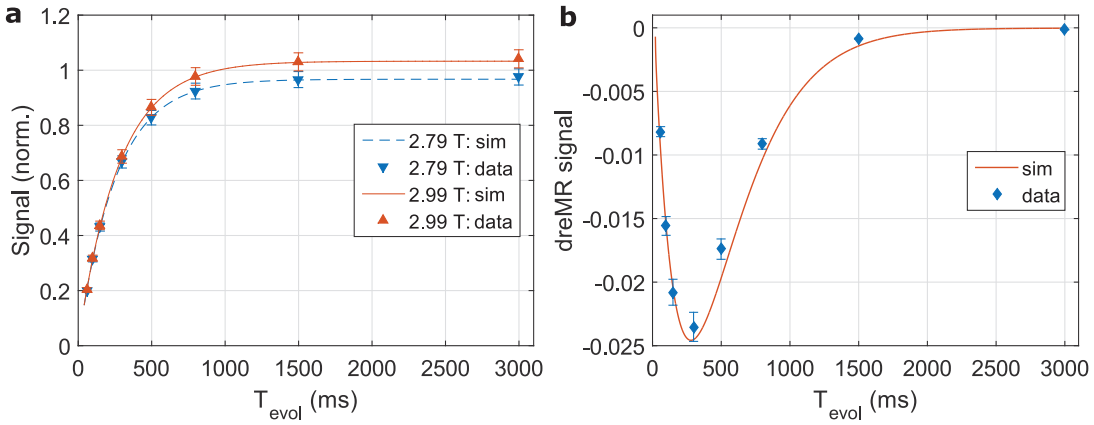

Figure 3.7: a) Simulated longitudinal relaxation curves for 2.99 T (red solid line) and 2.79 T (blue dashed line) compared to relaxation curves measured (mean ± standard deviation of ROI 2 in Figure 3.6a) with the proposed FFC-MRI system (upward-pointing triangle for 2.99 T and downward-pointing triangle for 2.79T). (b) Simulated and measured dreMR signal obtained by subtraction of the relaxation curves in (a) after normalization to account for different equilibrium magnetizations and effective ΔB_0 offset fields.

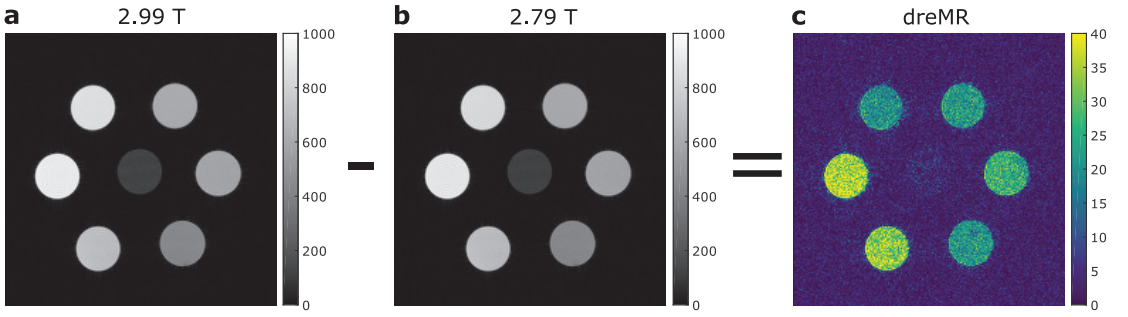

Figure 3.8: Images acquired for a field strength of 2.99 T (a) and 2.79 T (b) with an isotropic in-plane resolution of 0.2 mm and T_{evol} of 150 ms were normalized to account for different M_0 and effective offset fields. Image subtraction of (a) and (b) resulted in the corresponding dreMR image whereof the magnitude is shown in (c).

mize the dreMR contrast for a specific sample the evolution time T_{evol} should be chosen to match the sample's T_1 [18]. Therefore, equation (3.1) can be used to optimize dreMR imaging parameters under consideration of all timing restrictions of the ΔB_0 pulse in the MRI pulse sequence.

3.3.5 DreMR imaging

Figure 3.8 shows a dreMR image acquired with a T_{evol} of 150 ms and an isotropic in-plane resolution of 0.2 mm. As can be clearly seen, signal arises only from samples containing the dispersive IOMNPs, whereas the signal is strongly suppressed in the hexane reference sample. When comparing samples containing cubic shaped IOMNPS (samples 1-3 in Figure 3.6a), theoretically, maximum signal intensity should be observed for sample 1 as $T_{evol} \approx T_1$. In practice, the dreMR contrast in Figure 3.8 is altered by an additional T_2-weighting due to short T_2 of the IOMNPs [84]. Consequently, the samples with the highest concentrations seemingly paradoxically, show less contrast enhancement, though, in reality, their T_1 enhancement is maximal. Nevertheless, this dreMR image is a clear proof-of-principle, demonstrating the capability of generating R_1 dispersion contrast with suppressed background signal at a clinical field strength of 3 T. This proof is sufficient for the purpose of system validation only. For improved evaluation of signal contrasts, the TE of 15 ms has to be reduced to the order of a few ms to minimize the T_2-weighting, which was not feasible with the modified SR-SE sequence used herein.

Theoretically, a twofold increase in SNR of the images prior dreMR image subtraction is to be expected for 3 T compared to 1.5 T [89]. Aside from this potential benefit, the SNR increase in the dreMR image may be compensated by a reduced R_1 dispersion at 3 T. Whether a field strength of 1.5 T or 3 T is more beneficial for dreMR imaging depends strongly on the NMRD profile of the contrast agent in use. In the context of prospective QRE based contrast agents, it is favourable to have a wide variety of field-cycling ranges

as it is completely unexplored at which field strength such compounds give the best image contrast. Therefore, the presented FFC-MRI system expands the field cycling technique with an additional cycling range centered at 2.89 T.

3.4 Conclusions

In conclusion, we have successfully implemented a small animal FFC-MRI system for a clinical field strength of 3 T by inserting an additional B_0 insert coil into an otherwise conventional MRI system. Iron oxide magnetic nanoparticles proofed to be suitable for system validation as they exhibit a sufficiently high R_1 relaxation dispersion in the achievable field-cycling range of ± 100 mT around the nominal field strength of 2.89 T. System validation was successfully performed by comparison of FFC-MRI measurements with FFC-NMR relaxometry. Furthermore, a proof-of-principle for dreMR imaging at 3 T has been achieved by generating contrast arising only from the dispersive properties of the contrast agent in use. In the context of developing new contrast agents, this hardware implementation and validation provides a ready-to-use hardware setup for investigating dispersive properties of MRI contrast agents at a field strength of 3 T.

4

High-Field Detection of Biomarkers with Fast Field-Cycling MRI: The Example of Zinc Sensing

Markus Bödenler[1], Kyangwi P. Malikidogo[2], Jean-François Morfin[2], Christoph Stefan Aigner[1], Éva Tóth[2], Célia S. Bonnet[2], and Hermann Scharfetter[1]

[1] Institute of Medical Engineering, Graz University of Technology, Austria
[2] Centre de Biophysique Moléculaire, CNRS, France

Published as Hot Paper in:
Chemistry - A European Journal 25 (2019) 8236-8239
https://doi.org/10.1002/chem.201901157

Abstract

Many smart MRI probes provide response to a biomarker based on modulation of their rotational correlation time. The magnitude of such MRI signal changes is highly dependent on the magnetic field and the response vanishes at high fields (< 2 T). To overcome the loss of efficiency of responsive probes at high field, with FFC-MRI we exploit field-dependent information rather than the absolute difference in the relaxation rate measured in the absence and in the presence of the biomarker at a given imaging field. We report here the application of fast field-cycling techniques combined with the use of a molecular probe for the detection of Zn^{2+} to achieve 166 % MRI signal enhancement at 3 T, while the same agent provides no detectable response using conventional MRI. This approach can be generalized to any biomarker provided the detection is based on variation of the rotational motion of the probe

4.1 Introduction

Magnetic resonance imaging (MRI) is a prevalent diagnostic technique in medicine, due to its high temporal and spatial resolution, penetration depth, superb soft tissue contrast and the lack of harmful ionizing radiation. Contrast in MRI is essentially obtained by differences in local proton density and spatially varying relaxation times in the tissue of interest. MRI has moderate sensitivity compared to nuclear or optical imaging and therefore requires, in certain cases, amplification strategies to enhance water proton relaxation, such as the use of a contrast agent. MRI has great potential for molecular imaging (MI), which can provide spatially and temporally resolved maps of biomarkers (pH, presence of cations, enzymes, metabolites, temperature, etc.) to unravel molecular processes in tissues rather than their simple morphology. MI might enable earlier diagnosis, as these physiological changes happen prior to the morphological changes typically monitored by traditional MRI. MI requires the use of a contrast agent selective to the biomarker to detect.

The majority of MRI contrast agents are Gd^{3+} complexes, which affect mainly the longitudinal relaxation time T_1. Their efficiency, called relaxivity r_1, is defined by the paramagnetic relaxation rate enhancement of water protons by concentration unit of the agent. Two main approaches exist to render Gd^{3+} complexes responsive to the presence of a biomarker: altering either the number of water molecules directly coordinated to Gd^{3+}, q, or the rotational correlation time, τ_R, of the complex [90, 91]. With the "q-activated" approach, the response is roughly constant at any magnetic field, whereas with the "τ_R-activated" approach (τ_R modulation), the response is highly field-dependent. The effect of τ_R on relaxivity is reflected in the characteristic shape of the ^{1}H nuclear magnetic relaxation dispersion (NMRD) profile of slowly tumbling systems and provides the best efficiency at intermediate fields (relaxivity peak between 0.5-1.5 T) [60]. At higher magnetic fields (3 T and above), where the resolution of MRI is better, the benefit of long τ_R on proton relaxivity is diminished.

Fast field-cycling magnetic resonance imaging (FFC-MRI) is a novel strategy in MRI that takes specific advantage of the magnetic field dependency of relaxivity. In contrast to conventional MRI where the main magnetic field is fixed, in FFC-MRI the magnetic field can be altered during the imaging sequence [18, 28, 92] This allows for exploiting field-dependent information based on the partial derivative of the longitudinal relaxation rate with respect to the magnetic field, dR_1/dB_0. This method is particularly interesting to visualize slowly tumbling agents with high R_1 dispersion (i.e. high dR_1/dB_0; $R_1 = 1/T_1$ and $r_1 = (R_1 - R_{1dia})/[Gd]$, where R_{1dia} is the diamagnetic contribution to the relaxation rate and $[Gd]$ is the concentration of the contrast agent). It was successfully used to image probes that exhibit a strong relaxivity response upon protein binding, especially in the case of human serum albumin (HSA) [17, 93, 94]. To the best of our knowledge, this technique has not been used for responsive contrast agents. We demonstrate here its potential in zinc detection.

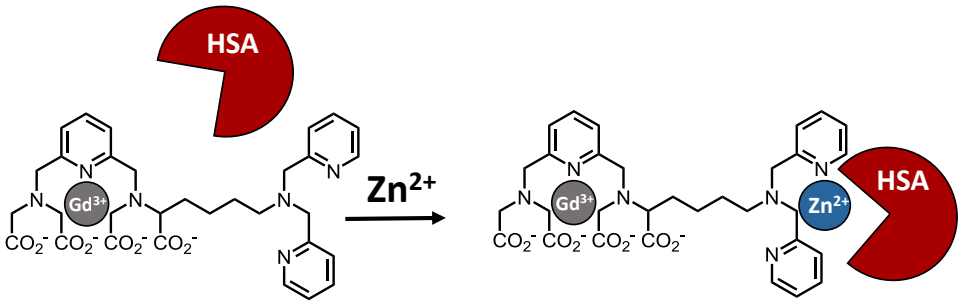

Figure 4.1: Chemical structure of the contrast agent and schematic representation of Zn^{2+} detection mechanism, based on τ_R modulation due to increased binding affinity in the presence of Zn^{2+}.

Zinc plays a pivotal role in various cellular processes including enzyme activities, DNA and protein synthesis or signal transduction [95]. Misregulations in Zn^{2+} homeostasis are associated with diabetes [96], cancers [97] and neurodegenerative diseases [98]. Significant effort has been devoted to non-invasive imaging of Zn^{2+} distribution to study its role in biological processes and to improve early stage diagnosis of diseases. Zn^{2+}-responsive probes have been designed based on q or τ_R modulation [99]. The rotational correlation time is typically controlled via binding of the Gd^{3+} complex to a macromolecule or protein, which becomes more important after Zn^{2+} coordination (Figure 4.1). This approach was mostly investigated for HSA because of its high concentration (0.6 mM) and the presence of several binding sites at the surface of the protein [100]. Although the relaxivity response to Zn^{2+} is remarkable at intermediate fields with these systems, it vanishes at high fields [90]. q-activated contrast agents could represent an efficient way to obtain a maximal response at higher fields, but their rational design remains a difficult challenge especially for metal ion detection. Indeed, the coordination spheres of both Gd^{3+} and the cation to detect, as well as the flexibility and length of the linker between the Gd^{3+}- and the Zn^{2+}-coordinating units should be all controlled in the design [99]. Therefore, novel strategies allowing sensitive, high-field MRI detection of τ_R-activated responsive probes are highly desirable.

Herein, we report on using FFC-MRI with a τ_R-activated, Zn^{2+} responsive agent in the presence of HSA. FFC-MRI takes benefit of the change of dR_1/dB_0 (slope in the NMRD profile), rather than the absolute difference in R_1 at a fixed magnetic field, upon Zn^{2+} binding. In a proof-of-concept in vitro experiment, we demonstrate that it is possible to overcome the loss of efficiency at a clinically relevant field strength and to generate Zn^{2+} dependent image contrast. Indeed, while the agent does not respond to Zn^{2+} in classical MRI at 3 T, 166 % MRI intensity increase is achieved upon Zn^{2+}-binding in FFC-MRI at the same field.

4.2 Results and Discussion

Our Zn^{2+}-responsive probe, GdL, comprises three moieties: (1) a Gd^{3+}-complexing unit based on a pyridine backbone; (2) a bis(pyridinylmethyl)amine (DPA) for Zn^{2+} chelation; and (3) a linker (Figure 4.1). The pyridinic backbone has shown to possess relatively good thermodynamic stability and kinetic inertness which previously enabled its safe application in animal studies [101]. In this complex, Gd^{3+} has two inner sphere water molecules, which are not replaced by physiological anions, and result in a high relaxivity. DPA displays good affinity (K_d = 7.57) and sufficient selectivity [102] for Zn^{2+}, and has been previously used for the detection of Zn^{2+} by MRI [103–106].

The hydrophobic moieties of the Gd^{3+} complex promote interaction with HSA, which generate a field-dependent relaxometric response to Zn^{2+} at physiological HSA concentration as illustrated in Figure 4.2. The NMRD profiles, both in the presence and in the absence of Zn^{2+}, show the hump typical for macromolecular systems at intermediate fields. The Zn^{2+} response is maximal at 0.7 - 1 T with a relaxivity increase of about 25 % upon Zn^{2+}-binding. In contrast, at 9.4 T, a roughly 30 % relaxivity decrease is obtained, while around 3 T, the response vanishes as the two NMRD profiles cross each other. In accordance with these results, no visible difference in R_1 can be observed in response to increasing Zn^{2+} concentration in solutions of GdL and HSA, by using standard MRI methods at 3 T (Figure 4.3b).

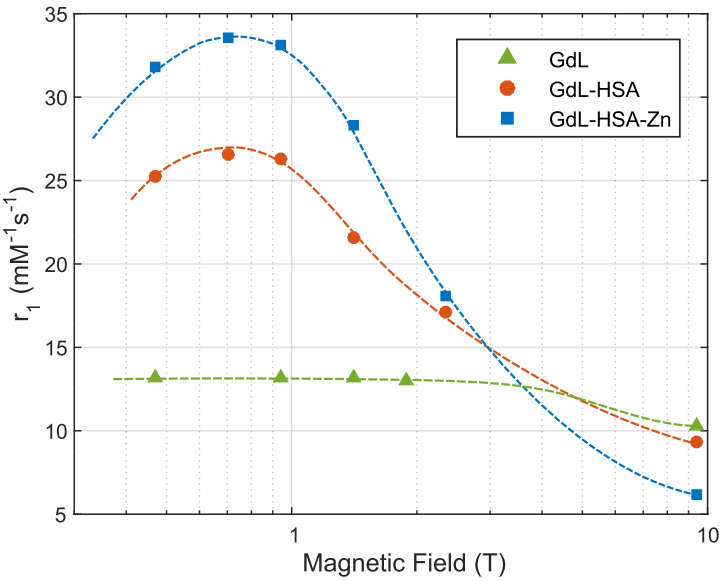

Figure 4.2: ^{1}H NMRD profiles of GdL alone (1.35 mM), GdL (0.26 mM) and GdL-Zn (equimolar ratio; 0.27 mM) in the presence of 0.6 mM of HSA at pH = 7.4 (HEPES buffer) and 298 K; the symbols represent measured points and the dashed lines serve to guide the eye.

For FFC-MRI, the hardware was realized by means of an additional B_0 insert coil synchronized with a clinical MRI system with a main magnetic field strength B_0 of 2.89 T [31]. The field-cycling hardware is capable of generating offset fields ΔB_0 of ± 100 mT within a minimum ramp time of 1 ms. Images were acquired at three different evolution fields (2.79, 2.89 and 2.99 T) using a saturation prepared spin echo sequence, where B_0 was ramped to the desired field-shift for a duration T_{evol} between the preparation pulse and image acquisition. A detailed description of the imaging experiments and the analysis of the regions of interest (ROI) is given in the experimental details section 4.4.

R_1 maps were obtained at 2.89 T (the nominal B_0 field strength of the MRI system; Figure 4.3b), 2.79 T (Figure 4.5c) and 2.99 T (Figure 4.5d) by cycling the evolution field. The magnetic field dependence was calculated from the difference between R_1 maps for 2.99 T and 2.79 T. After normalization with ΔB_0, this yields the R_1 dispersion map presented in Figure 4.3c (i.e. $\Delta R_1/\Delta B_0$ within the achievable field-cycling range). No significant $\Delta R_1/\Delta B_0$ is visible for the reference samples containing Gadovist [87] and GdL without HSA as expected from the NMRD profile. The complex without Zn^{2+} in the presence of HSA shows a background dispersion due to the formation of the GdL-HSA adduct as shown in the NMRD profile (Figure 4.2). It represents the "inactivated" state of the

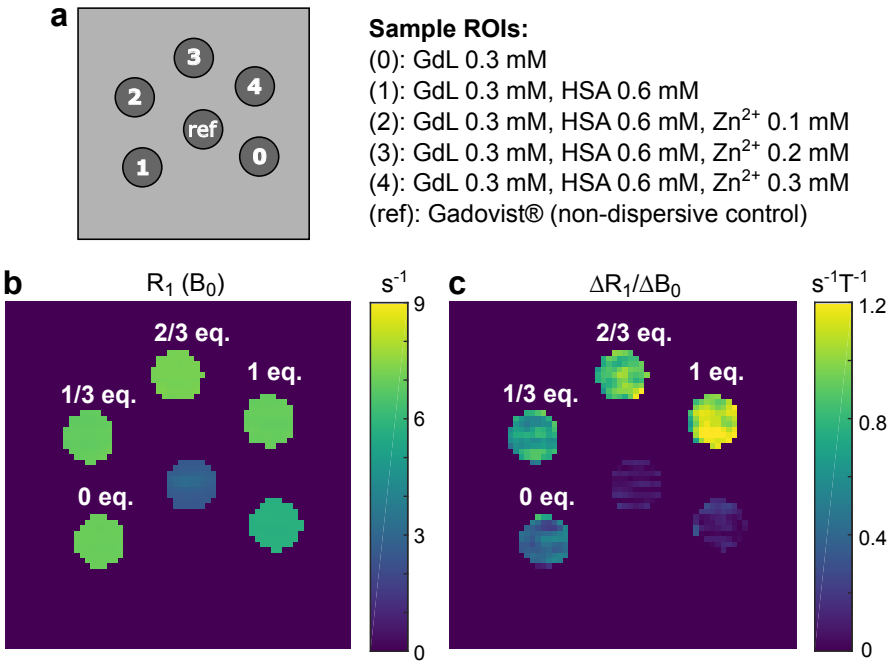

Figure 4.3: (a) Sample arrangement for the MR phantom measurements. (b) R_1 map obtained at the nominal B_0 field strength (2.89 T) of the MRI system. No visible difference in R_1 can be observed upon the addition of Zn^{2+}. (c) $\Delta R_1/\Delta B_0$ map calculated by subtracting R_1 maps for 2.99 T and 2.79 T. The high contrast for samples with increasing Zn^{2+} concentration should be noted. See Experimental Details section 4.4 for image acquisition details.

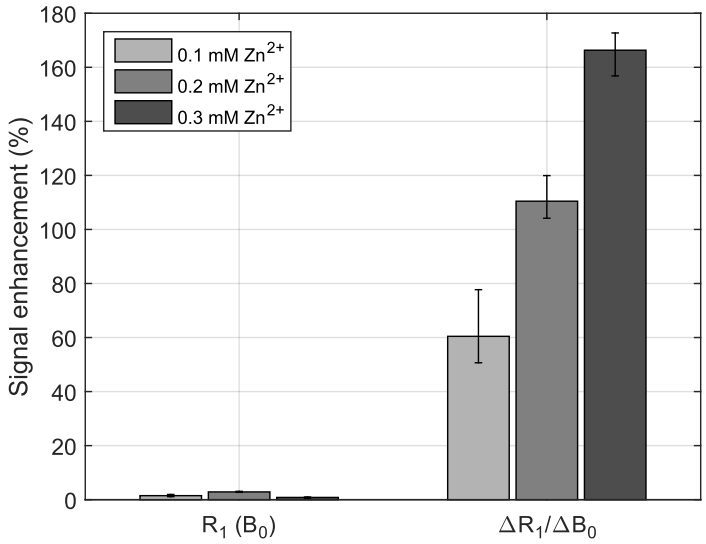

Figure 4.4: Percent signal enhancement of the Zn^{2+} response for a change in R_1 at the nominal B_0 of the MRI system (left) and the change of $\Delta R_1/\Delta B_0$ accessed by FFC-MRI (right). The signal enhancement was calculated with respect to the value obtained for the GdL-HSA complex without Zn^{2+}; data is presented in 1st quartile, median, and 3rd quartile. The activation response is linear with respect to an increasing Zn^{2+} concentration (up to 1 eq. Zn^{2+}); see Experimental Details for the linear regression analysis.

probe. The FFC-MRI signal intensity increases with increasing Zn^{2+} concentration up to one equivalent of Zn^{2+} (Figure 4.3c; see Table 4.1 in section 4.4 for values). Figure 4.4 (and Table 4.1, section 4.4) summarizes the relative signal enhancement upon Zn^{2+} addition to the GdL/HSA solution. The maximum signal enhancement is about 166 % upon the addition of 1 eq. of Zn^{2+}, in contrast to no signal enhancement detected with standard MRI at the nominal field strength of 2.89 T. This is quite remarkable since, even at the most optimal field (0.5 T), the relaxivity change upon Zn^{2+}-binding is only 26 % for this probe (see NMRD profile). For comparison, 100 to 220 % relaxivity changes were reported for q-activated Zn-responsive contrast agents [107, 108]. Similar relaxivity response (165 %) was obtained for the most-studied τ_R-activated contrast agent at 0.5 T [106], however, at higher field the response decreases dramatically. This last agent was used in vivo to detect Zn^{2+} in the pancreas [109] or in prostate cancer [110]. These studies were performed at 9.4 T, where relaxometric data predict about 50 % relaxivity response to Zn^{2+}. In a recent study, Zn^{2+} was imaged with another contrast agent providing a relaxivity response of only 7.5 % at the imaging field of 9.4 T [111]. With the FFC-MRI technique, remarkably higher signal variations are achieved. Moreover, the $\Delta R_1/\Delta B_0$ signal increase is linearly proportional to Zn^{2+} concentration (see section 4.4 for linear regression analysis). This, combined with our previously-reported bimodal quantification approach [112], might open unprecedented opportunities towards high precision zinc quantification.

In the magnetic field range of 1.5 T to 3 T, routinely used for clinical imaging, the R_1 dispersion of tissues is inherently weak. For contrast agents exhibiting a large $\Delta R_1/\Delta B_0$, this small tissue R_1 dispersion (e.g. -0.19 $s^{-1}T^{-1}$ for murine muscle tissue at 1.5 T) represents a negligible anatomical background signal [47]. In our example, if any free (not protein-bound) GdL or GdL-Zn is present, it will be "silent" (see Figure 4.3c), as the NMRD curves of such small complexes show no dispersion at these fields. On the other hand, the binding of GdL to HSA in the absence of Zn^{2+} entails a dispersion (background signal) that cannot be suppressed in the FFC-MR image. In order to decrease this signal of the inactivated state and to generate an even more important response to Zn^{2+}, the affinity of the GdL probe for HSA could be decreased.

It is important to estimate the in vivo detection limit of zinc. Considering the linear response of $\Delta R_1/\Delta B_0$ to zinc concentration and assuming that the background signal is provided by the GdL-HSA adduct, a rough estimate of the detection limit would be 60 μM Zn^{2+} (corresponding to 0.213 eq. Zn^{2+} for 0.3 mM GdL concentration; see Experimental Details). The contrast agent concentration used in this proof-of-principle study lies in the clinically relevant region (the approved dose ranges from 0.1 to 0.3 mmol/kg) [4]; and the estimated Zn^{2+} detection limit matches physiological concentrations which attain 100 μM to 1 mM in pancreatic regions or neurons [113]. This detection limit is lower than that previously calculated for classical MRI detection [105]. It should be noted that FFC-MRI requires an insert coil to vary the B_0 field which, with respect to classical MRI, implies technical constraints on image acquisition, such as duty cycle considerations for electromagnetic operation, prolonged scan times and limited imaging region [92]. Despite these constraints, pre-clinical FFC-MRI studies have been promising and shown the feasibility of in vivo visualization of MRI probes with a detection limit of about 40 μM [18, 47, 93, 94]. This is rather encouraging as it suggests that the contrast agent concentration used in our study can be reduced which implies an even lower Zn^{2+} detection limit. Additional technical improvements and post-processing methods such as image denoising can further contribute to better detection limits, which will be subject of future investigations.

4.3 Conclusions

To conclude, we have demonstrated successful Zn^{2+} detection at 3 T using FFC-MRI (166 % intensity increase), while no detection was possible with the same probe at this field using conventional MRI. As the chemical design of efficient Zn^{2+} responsive probes adapted to classical T_1 detection at high fields remains a challenge, FFC-MRI represents a highly interesting alternative. It can potentially add value to a great number of previously reported responsive probes that did not produce a detectable signal change at high fields. This technique is not solely limited to the detection of zinc, but can be adapted for the detection of any biomarker.

4.4 Experimental Details

4.4.1 Syntheses and Characterizations

The chemicals and solvents were purchased from Alfa-Aesar, Fisher Scientific, Sigma-Aldrich and TCI Europe. They were used as received unless otherwise noted. The solvents used for reactions were dried and kept under molecular sieve. Aluminum sheets cover with 60 F254 silica gel plates were used for thin layer chromatography and visu-alized using UV light or revealed under the appropriate conditions. Flash chromatographies were performed using Interchim flash chromatography Spot II device. ^{1}H NMR (600 MHz) and ^{13}C NMR (150 MHz) spectra were recorded in deuterated solvents on a Bruker Advanced III HD Spectrometer. Proton and carbon chemical shifts (δ) are reported in parts per million (δ scale), and all coupling constant (J) values are in Hertz (Hz). The following abbreviations were used to explain the multiplicities: s (singlet), d (doublet), t (triplet), q (quartet), m (multiplet) and bs (broad signal). High Resolution Mass Spectrometry (HRMS) spectra were recorded using an electron spray ionization (Experimental Details section 4.4) technique.

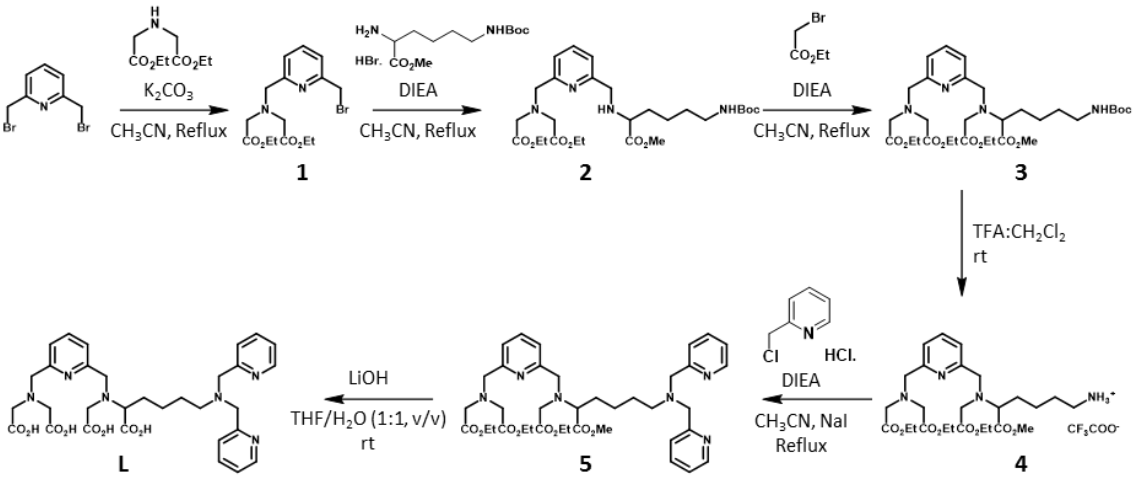

Compound 1: Diethyl 2,2'-(((6-(bromomethyl)pyridin-2-yl)methyl)azanediyl)diacetate

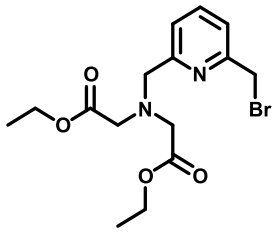

To a solution of 2,6-bis(bromomethyl)pyridine (5.0 g, 19.02 mmol) in acetonitrile (200 mL) were added potassium carbonate (2.2 g, 15.92 mmol) and diethyl iminodiacetate (1.2 g, 6.34 mmol) dropwise over a period of 1 h. The mixture was refluxed for an additional 3h. The solids were removed by filtration and the solvent was evaporated. The product 1 was obtained after purification by flash chromatography on silica gel (Dichloromethane: Ethyl Acetate 6:4) as a yellow oil (2.06 g). **Yield: 87 %**

^{1}H NMR (600 MHz, $CDCl_3$): δ(ppm) 7.68 (t, ^{3}J= 7.8 Hz, ^{1}H); 7.56 (d, ^{3}J= 7.8 Hz, ^{1}H); 7.34 (d, ^{3}J = 7.8 Hz, ^{1}H); 4.53 (s, 2H); 4.16 (q, ^{3}J = 7.2 Hz, 4H); 4.07 (s, 2H); 3.63 (s, 4H); 1.25 (t, ^{3}J = 7.2 Hz, 6H).

^{13}C NMR (150 MHz, $CDCl_3$): δ(ppm) 170.7; 158.8; 155.7; 137.3; 121.9; 121.6; 60.1; 59.4; 54.4; 33.7; 13.9.

HRMS: calc. for $C_{15}H_{21}BrN_2O_4$ $[M+H]^+$ 373.0685; found 373.0789

Compound 2: Diethyl 2,2'-(((6-(((6-((tert-butoxycarbonyl)amino)-1-methoxy-1-oxohexan-2-yl)amino)methyl)pyridin-2-yl)methyl)azanediyl)diacetate

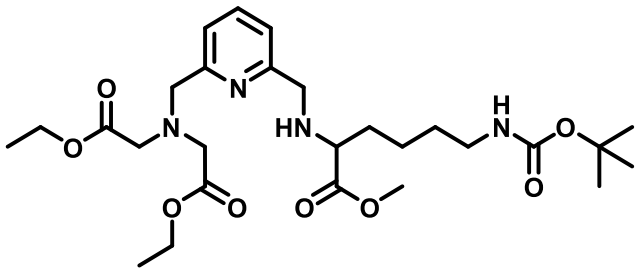

A solution of compound 1 (419 mg, 1.12 mmol) in acetonitrile (30 mL) was added dropwise over a peri-od of 1h to a mixture of Nϵ-Boc-L-lysine methyl ester hydrochloride (1g, 3.37 mmol) and di-isoproplylethylamine (1.45g, 11.23 mmol) in acetonitrile (70 mL). The mixture was refluxed for 18h. The solvent was evaporated, and the crude product

was purified by flash chromatography on silica gel (Ethyl Acetate, 1 % triethylamine) to afford compound 2 as a yellow oil (438 mg). **Yield: 71 %**

^{1}H NMR (600 MHz, $CDCl_3$): δ(ppm) 7.63 (t, ^{3}J = 7.6 Hz, 1H); 7.46 (d, ^{3}J = 7.6Hz, 1H); 7.21 (d, ^{3}J = 7.6 Hz, 1H); 4.81 (s, 1H); 4.17 (q, ^{3}J = 7.2 Hz, 4H); 4.04 (s, 2H); 3.96 (d, 2J = 15.4 Hz, 1H); 3.84 (d, 2J = 15.4 Hz, 1H); 3.70 (s, 3H); 3.61 (s, 4H); 3.31 (t, ^{3}J = 6.6 Hz, 1H); 3.10 (m, 2H); 2.30 (bs, 1H); 1.70 (m, 2H); 1.48 (m, 2H); 1.42 (s, 9H); 1.40 (m, 2H); 1.26 (t, ^{3}J = 7.2 Hz, 6H).

^{13}C NMR (150 MHz, $CDCl_3$): δ(ppm) 175.4; 171.0; 158.5; 158.3; 155.8; 136.9; 121.0; 120.3; 78.7; 60.8; 60.3; 59.8; 54.7; 53.2; 51.6; 40.2; 32.9; 29.7; 28.3; 22.9; 14.1.

HRMS: calc. for $C_{27}H_{44}N_4O_8$ $[M+H]^+$ 553.3159; found 553.3233

Compound 3: Diethyl 2,2'-(((6-(((6-((tert-butoxycarbonyl)amino)-1-methoxy-1-oxo hexan-2-yl)(2-ethoxy-2-oxoethyl)amino) methyl)pyridin-2-yl)methyl)azanediyl) diacetate

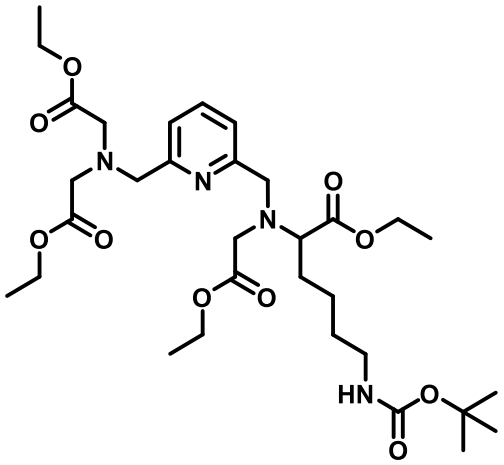

A mixture of compound 2 (436 mg, 0.79 mmol), ethyl bromoacetate (171.3 mg, 1.03 mmol) and di-isoproplylethylamine (816 mg, 6.31 mmol) in acetonitrile (10 mL) was refluxed for 23h. The solvent was evaporated, and product 3 was isolated after a purification by flash chromatography on silica gel (Di-chloromethane: Ethyl Acetate 1:1 + 1% Triethylamime) as a yellow oil (430 mg). **Yield: 85 %**

^{1}H NMR (600 MHz, $CDCl_3$): δ(ppm) 7.66 (t, ^{3}J = 7.6 Hz, 1H); 7.52 (d, ^{3}J = 7.6 Hz, 1H); 7.45 (d, ^{3}J = 7.6 Hz, 1H); 4.73 (s, 1H); 4.17 (q, ^{3}J = 7.1 Hz, 4H); 4.12 (q, ^{3}J = 7.1 Hz, 2H) ; 4.03 (s, 2H); 3.97 (d, 2J = 15.5 Hz, 1H); 3.84 (d, 2J = 15.5 Hz, 1H); 3.70 (s, 3H); 3.61 (s, 4H); 3.53 (d, 2J = 17.6 Hz, 1H); 3.24 (d, 2J = 17.6 Hz, 1H); 3.43 (t, ^{3}J = 7.5 Hz, 1H); 3.09 (m, 2H); 1.73 (m, 2H); 1.45 (m, 2H; 2H); 1.43 (s, 9H); 1.26 (t, ^{3}J = 7.1, 6H); 1.24 (t, ^{3}J = 7.1, 3H).

^{13}C NMR (150 MHz, $CDCl_3$): δ(ppm) 173.4; 171.5; 171.1; 159.0; 158.0; 155.9; 137.1; 121.1; 120.9; 78.8; 63.4; 60.4; 59.8; 57.6; 54.8; 52.5; 51.3; 40.2; 29.7; 29.4; 28.3; 23.2; 14.1.

HRMS: calc. for $C_{31}H_{50}N_4O_{10}$ [M+H]+ 639.3527; found 639.3599

Compound 4: Diethyl 2,2'-(((6-((((6-amino-1-methoxy-1-oxohexan-2-yl)(2-ethoxy-2-oxoethyl) amino)methyl)pyridin-2-yl)methyl) azanediyl) diacetate

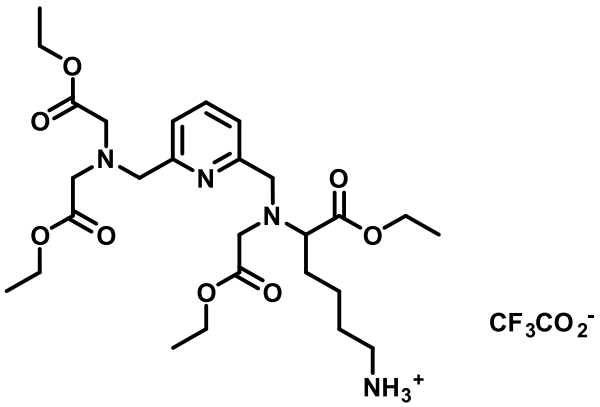

To a solution of compound 3 (0.428 g, 0.67 mmol) in dichloromethane (5 mL) was added trifluroacetic acid (5 mL) and the mixture was stirred for 1 h at room temperature. The solvent and the excess of tri-fluoroacetic acid were evaporated to give yellow oil (437 mg).
Yield: 100 %

^{1}H NMR (600 MHz, D_2O): δ(ppm) 8.42 (t, ^{3}J = 7.8 Hz, 1H); 7.89 (d, ^{3}J = 7.8 Hz, 1H); 7.84 (d, ^{3}J = 7.8 Hz, 1H); 6.09 (s, 3H); 4.48 (d, 2J = 17,1 Hz, 1H); 4.44 (s, 2H); 4.43 (d, 2J = 17,1 Hz, 1H); 4.13 (m, 4H7, 2H); 3.75 (s, 4H); 3.72 (s, 3H); 3.70 (m, 2H); 3.57 (t, ^{3}J = 7.2 Hz, 1H); 2.91 (t, ^{3}J = 7.6 Hz, 2H); 1.80 (m, 2H); 1.65 (m, 2H); 1.45 (m, 2H); 1.22 (m, 6H, 3H).

^{13}C NMR (150 MHz, CD_3OD): δ(ppm) 173.0; 172.3; 171.5; 154.3; 145.9; 124.2; 124.0; 64.8; 60.9; 60.8; 55.5; 55.1; 53.3; 52.9; 51.0; 39.0; 29.4; 26.8; 22.9; 13.0; 13.0.

HRMS: calc. for $C_{26}H_{42}N_4O_8$ $[M+H]^+$ 539.3003; found 539.3077

A mixture of compound 4 (380 mg, 0.57 mmol), 2-(chloromethyl)pyridine hydrochloride (750 mg, 4.5 mmol), sodium iodide (200 mg, 1.34 mmol) and DIEA (1.3 g, 10.05 mmol) was refluxed in acetonitrile (20 ml) for 24h. The solids were filtered and the solvent was evaporated. The residue was purified by flash chromatography on silica gel (Ethyl Acetate, 1% triethylamine) and compound 6 was obtained as a yellow oil (350 mg).
Yield: 83 %

Compound 5: D Diethyl 2,2'-(((6-(((6-(bis(pyridin-2-ylmethyl) amino)-1-methoxy-1-oxohexan-2-yl)(2-ethoxy-2-oxoethyl)amino)methyl) pyridin-2-yl)methyl)azanediyl)diacetate:

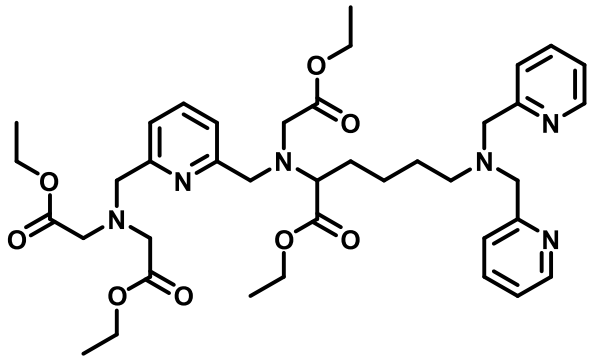

^{1}H NMR (600 MHz, $CDCl_3$): δ(ppm) 8.57 (d, ^{3}J = 4.4 Hz, 2H); 7.64 (t, ^{3}J = 7.4 Hz, 2H); 7.59 (t, ^{3}J = 7.8 Hz, 1H); 7.51 (d, ^{3}J = 7.8 Hz, 1H); 7.45 (d, ^{3}J = 7.5 Hz, 1H); 7.14 (t, ^{3}J = 5.8 Hz, 2H); 4.16 (q, ^{3}J = 7.1 Hz, 4H); 4.10 (q, ^{3}J = 7.1 Hz, 2H); 4.02 (s, 2H); 3.96 (d, 2J = 15.7 Hz, 2H); 3.79 (s, 4H); 3.68 (s, 3H); 3.60 (s, 4H); 3.51 (d, 2J= 17.6 Hz, 2H) ; 3.39 (t, ^{3}J = 7.7 Hz, 1H); 2.52 (t, ^{3}J = 6.7 Hz, 2H); 1.65 (m, 2H); 1.53 (m, 2H); 1.39 (m, 2H); 1.26 (t, ^{3}J = 7.1 Hz, 6H); 1.21 (t, ^{3}J = 7.1 Hz, 3H).

^{13}C NMR (150 MHz, $CDCl_3$): δ(ppm) 173.4; 171.5; 171.1; 159.9; 159.2; 158.0; 148.8; 137.1; 136.3; 122.8; 121.8; 121.1; 120.8; 63.7; 60.4; 60.4; 60.4; 59.8; 57.6; 54.8; 54.1; 52.5; 51.2; 30.0; 26.8; 23.9; 14.2; 14.1.

HRMS: calc. for $C_{38}H_{52}N_6O_8$ $[M+H]^+$ 721.3847; found 721.2156

Ligand 2,2'-(((6-(((5-(bis(pyridin-2-ylmethyl) amino)-1-carboxypentyl)(carboxymethyl) amino)methyl)pyridin-2-yl)methyl) azanediyl)diacetic acid

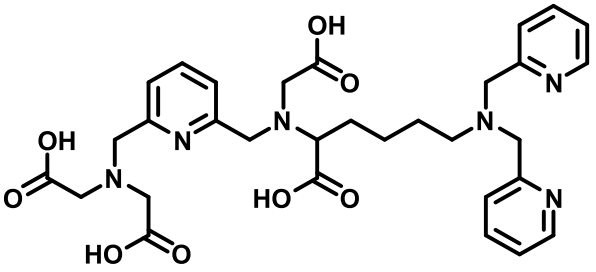

To a solution of compound 5 (0.348 g, 0.47 mmol) in a mixture of THF: H2O (1:1 v:v, 20 mL), was add-ed lithium hydroxide (0.222 g, 5,29 mmol) and the solution was stirred for 1 day at room temperature. The solvent was evaporated and the ligand L was obtained after a purification by flash chromatography on C18 phase (MeOH: H2O 1:1 with 0,1 % TFA), as a white solid (0.295 g).

^{1}H NMR (600 MHz, D_2O): δ(ppm) 8.66 (d, ^{3}J = 5.5 Hz, 2H); 8.45 (t, ^{3}J = 7.3 Hz, 2H); 8.01 (t, ^{3}J = 7.6 Hz, 1H); 7.98 (d, ^{3}J = 7.3 Hz, 2H); 7.88 (t, ^{3}J = 5.5 Hz, 2H); 7.54 (m, 2H); 4.58 (s, 2H); 4.55 (2H); 4.24 (s, 4H); 4.02 (s, 4H); 3.91 (s, 2H); 3.84 (m, 1H); 2.63 (t, ^{3}J = 7.5 Hz, 2H); 1.80 (m, 2H); 1.47 (m, 2H); 1.31 (m, 2H).

^{13}C NMR (150 MHz, D_2O): δ(ppm) 174.7; 173.1; 157.8; 155.7; 148.6; 139.6; 136.2; 124.0; 122.2; 121.0; 72.3; 63.5; 62.5; 60.3; 60.1; 57.9; 56.4; 28.6; 28.0; 23.8.

HRMS: calc. for $C_{31}H_{38}N_6O_8$ $[M+H]^-$ 621.2751; found 621.2686

4.4.2 ^{1}H R_1 NMRD Measurements

Solution preparation:

The exact ligand concentrations were determined by adding an excess of lanthanide solution to the ligand solution and titrating the metal excess with standardised Na_2H_2EDTA in urotropine buffer (pH 5.6 - 5.8) in the presence of Xylenol Orange as an indicator. The concentrations of the metal solutions were determined similarly by complexometric titrations. The complexes were prepared by mixing 1 eq. of L, with 1 eq. of Gd^{3+}, and the pH was adjusted to 7.4 either with a buffered solution or by adding KOH or HCl to the solution. The absence of free Gd^{3+} was checked by the Xylenol orange test. The concentrations of Gd^{3+}-containing solutions were also checked by ICP-MS and BMS measurements when possible. Zn^{2+} concentrations were also checked by ICP-MS. HSA was used in its fatty-acid free form.

Relaxometric measurements:

Proton NMRD profiles were performed on a Bruker WP80 NMR electromagnet adapted to variable field measurements (20-80 MHz) and controlled by a SMARTracer PC-NMR console, or on a minispec Bruker "mqvar" (20, 30, 40, 60 MHz). The temperature was monitored by a VTC91 temperature control unit and maintained by a gas flow. The temperature was determined by previous calibration with a Pt resistance temperature probe. Relaxivities at 100 MHz and 400 MHz were measured on a Bruker Advance 100 and 400, respectively. The longitudinal relaxation rates ($1/T_1$) were determined in water.

4.4.3 FFC-MRI Measurements and Analysis

The FFC-MRI hardware was implemented by means of an additional B_0 insert coil (Resonance Research Inc., USA) synchronized with a clinical MRI system (Skyra, Siemens Healthineers, Germany) with a main magnetic field strength B_0 of 2.89 T [31]. A custom-built transmit/receive birdcage radio frequency coil (MRI.TOOLS GmbH, Germany) was designed to fit in the bore of the insert coil and enables an imaging region suitable for small animal and phantom imaging. The field-cycling hardware is capable of generating offset fields ΔB_0 of $\pm$100 mT within a minimum ramp time of 1 ms. This adds an extra

dimension to the MRI pulse sequence by allowing for a modulation of the main magnetic field by $B_0 \pm \Delta B_0$. A MRI phantom was prepared holding six glass tubes, each tube with 4 cm length and 8 mm diameter. The glass tubes were arranged as illustrated in Figure 4.5a and contain: (0) 0.3 mM GdL, (1-4) 0.3 mM GdL, 0.6 mM HSA, 0, 0.1, 0.2 and 0.3 mM Zn^{2+} concentration, respectively, and (ref) Gadovist® as non-dispersive control. Samples (0-4) were stabilized at pH 7.4 with 0.1 M HEPES buffer. Images were acquired at three different evo-lution fields (2.79, 2.89 and 2.99 T) using a saturation prepared spin echo sequence, where B_0 was ramped to the desired field-shift for seven different durations Tevol (60, 100, 150, 300, 500, 800 and 1500 ms) between the preparation pulse and image acquisition. During acquisition of FFC-MRI images, eddy current effects are compensated using dynamic reference phase modulation (eDREAM, [45]). The remaining imaging parameters were: repetition time TR = 3000 ms, echo time TE = 15 ms, Field of View FoV = 40 mm x 40 mm, matrix size = 64 x 64, bandwidth BW = 130 Hz/Px, flip angle = 90° and slice thickness = 5 mm; all measurements were performed at room temperature. At each field, R_1 maps (Figure 4.5b-d) were calculated on a pixel-by-pixel basis by nonlinear fitting the following three-parameter (S_0, α, and R_1) mono-exponential saturation recovery model:

$$S(T_{evol}) = S_0(1 - \alpha\ e^{-T_{evol}R_1}). \tag{4.1}$$

A $\Delta R_1/\Delta B_0$ map (Figure 4.5e) was obtained by subtracting R_1 maps for 2.99 T and 2.79 T. This gives a good linear approximation of the slope in the NMRD profile (i.e. dR_1/dB_0; $R_1 = 1/T_1$ and $r_1 = (R_1 - R_{1dia})/[Gd]$, where R_{1dia} is the diamagnetic contribution to the relaxation rate and $[Gd]$ is the concentration of the contrast agent) within the achievable field-cycling range. A region of interest (ROI) analysis was performed by calculating the median and quartiles out of all selected pixels within a sample; the values are summarized in Table 4.1. The increase of median $\Delta R_1/\Delta B_0$ values in Table 4.1 is linear ($R^2 = 0.998$) up to a Zn^{2+} concentration of 0.3 mM, which corresponds to one equivalent of Zn^{2+}. From linear regression analysis follows a background dispersion of -0.42 [-0.37, -0.46] $s^{-1}T^{-1}$ and a slope of -0.23 [-0.20, -0.25] $s^{-1}T^{-1}$/0.1 mM Zn^{2+}; brackets indicate the 95% confidence intervals (CI). Note that the $\Delta R_1/\Delta B_0$ values are negative as the slope in the NMRD profile is negative within the field-cycling range of 2.89 T ± 100 mT.

The detection limit of Zn^{2+} concentration can be roughly estimated with a detection limit defined as $S_{LOD} = S_{back} + 3SD_{back}$, where S_{back} is the background dispersion signal from the sample without Zn and the SD_{back} is the corresponding standard deviation in this region. Due to the dispersion intensity in the sample, the best estimation of these values is obtained from the regression analysis considering the linear relationship between the activation response and Zn^{2+} concentration. Hence, S_{back} = -0.42 $s^{-1}T^{-1}$ and SD_{back} can be calculated from the 95% CI (of the background dispersion determined before) by: $S_{back} = \sqrt{N}(CI_{upper} - CI_{lower}/3.92)$ with N, the number of points in the regression. This

gives an R_1 dispersion value for the S_{LOD} of -0.56 $s^{-1}T^{-1}$ which corresponds to a minimum detectable Zn^{2+} concentration of 60 μM (using the linear regression of the Zn^{2+} response) for a contrast agent concentration of 0.3 mM.

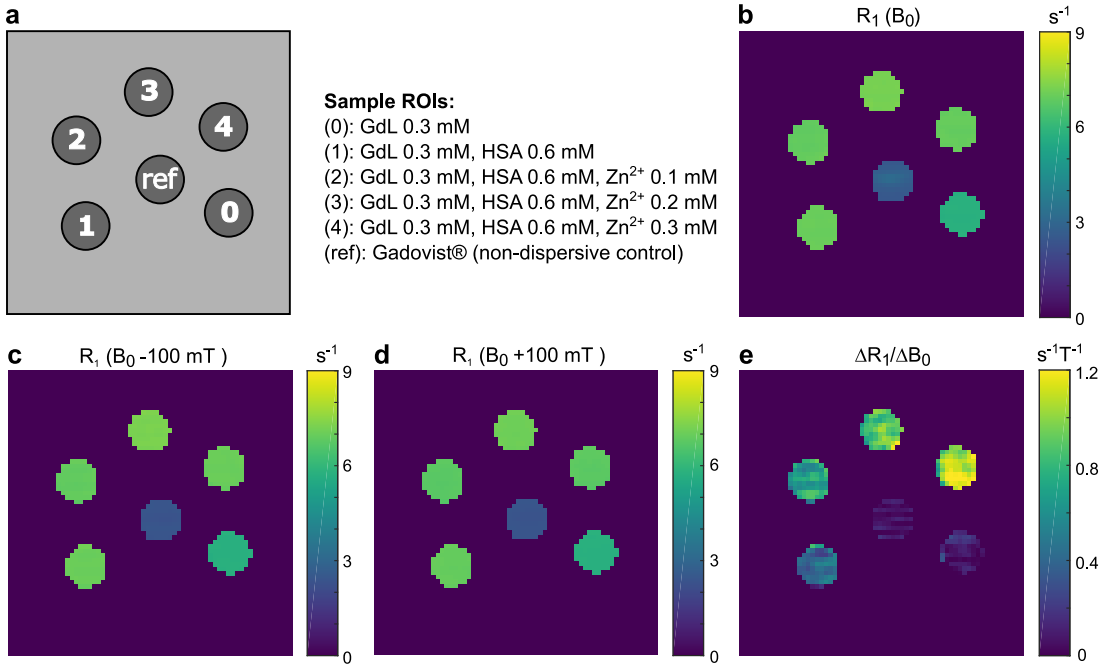

Figure 4.5: (a) Sample arrangement for the FFC-MRI phantom measurements. R_1 maps were calculated on a pixel-by-pixel basis for the nominal B_0 field of the MRI system (b), by cycling the evolution field to 2.79 T (c) and 2.99 T (d). (e) R_1 dispersion map $\Delta R_1/\Delta B_0$ obtained by subtracting R_1 maps in (d) and (c).

Table 4.1: Median (1st quartile, 3rd quartile) values of relaxation rates R_1 at 2.79, 2.89 and 2.99 T and R_1 dispersion $\Delta R_1/\Delta B_0$ (2.99 T-2.79 T) at room temperature; data were obtained by ROI analysis in Figure 4.5.

Sample	**R_1 (s^{-1})**			**$\Delta R_1/\Delta B_0$ ($s^{-1}T^{-1}$)**
	2.79 T	2.89 T	2.99 T	
GdL	5.69 (5.67, 5.70)	5.71 (5.69, 5.72)	5.69 (5.68, 5.70)	0.05 (-0.01, 0.13)
GdL-HSA	6.97 (6.94, 6.98)	6.95 (6.94, 6.96)	6.88 (6.87, 6.90)	-0.41 (-0.35, -0.50)
GdL-HSA-$(Zn^{2+})_{1/3\ eq.}$	6.84 (6.82, 6.87)	6.84 (6.82, 6.87)	6.71 (6.70, 6.73)	-0.66 (-0.35, -0.50)
GdL-HSA-$(Zn^{2+})_{2/3\ eq.}$	7.20 (7.18, 7.22)	7.15 (7.14, 7.16)	7.03 (7.02, 7.04)	-0.86 (-0.81, -0.95)
GdL-HSA-$(Zn^{2+})_{1\ eq.}$	6.96 (6.94, 6.98)	6.89 (6.87, 6.90)	6.74 (6.72, 6.77)	-1.09 (-0.99, -1.16)

5

CONQUER: Contrast by Quadrupole Enhanced Relaxation

This chapter is based on the work conducted within the scope of the research project CONQUER supported by the European Commission in the frame of the Horizon 2020 program (FET open, grant agreement 665172). Markus Bödenler contributed to the following peer-reviewed journal articles:

C. Gösweiner, P. Lantto, R. Fischer, C. Sampl, E. Umut, P.-O. Westlund, D. Kruk, M. Bödenler, S. Spirk, A. Petrovic, and H. Scharfetter. Tuning Nuclear Quadrupole Resonance : A Novel Approach for the Design of Frequency-Selective MRI Contrast Agents. *Phys. Rev. X*, 8(2):021076, 2018, `https://link.aps.org/doi/10.1103/PhysRevX.8.021076`

C. Gösweiner, D. Kruk, E. Umut, E. Masiewicz, M. Bödenler, and H. Scharfetter. Predicting quadrupole relaxation enhancement peaks in proton R1-NMRD profiles in solid Bi-aryl compounds from NQR parameters. *Molecular Physics*, 117(7-8):910–920, apr 2019, `https://doi.org/10.1080/00268976.2018.1519201`

Abstract

The FET Open project "CONtrast by QUadrupole Enhanced Relaxation", abbreviated with CONQUER, explored the feasibility of quadrupole relaxation enhancement (QRE) as a fundamentally new contrast mechanism for the design of responsive and frequency-selective MRI contrast agents. The vision of CONQUER is to develop exogenous QRE based molecular probes that exhibit a frequency-selective nature in the magnetic field range relevant for clinical diagnostics, similar to naturally observed QRE for amine and/or amide groups in protein backbones in the low field region. A variety of compounds containing the quadrupole nucleus ^{209}Bi have been investigated during CONQUER. As an essential breakthrough, the first QRE mediated by ^{209}Bi could be observed in the solid state and for aqueous dispersions of nanoparticles constituted of the QN core compound. This proof of the mechanism of action represents a notable step towards QRE based imaging.

5.1 The Vision: Towards Frequency-Selective MRI Contrast

The dipole-dipole interaction between quadrupole nuclei and water protons can lead to relaxation enhancement of proton spins i.e. an increase of the longitudinal relaxation rate R_1. The aim of CONQUER was to unravel the potential of this so-called quadrupole relaxation enhancement (QRE) as a central mechanism for the design of a new class of frequency-selective MRI contrast agents. As already mentioned in chapter 2.4.2, QRE has been first observed between water protons and ^{14}N quadrupole nuclei from amine and/or amide groups in protein backbones. The effectiveness of QRE from ^{14}N as a contrast mechanism for MRI has been utilized with low field FFC-MRI systems to generate image contrast based on the presence of immobilized proteins [28, 82]. Quadrupole peaks of ^{14}N occur in the low field regime of the ^{1}H R_1 NMRD profile and therefore cannot be accessed with high field FFC-MRI systems. The vision of CONQUER is to generate pronounced quadrupole peaks in the clinical field range, comparable to the endogenous ^{14}N peaks at low fields, by the administration of an exogenous QRE contrast agent. Provided the resonance condition between the spin transitions of protons and the QN is fulfilled, QRE can become effective leading to a frequency-selective nature of the contrast agent. Consequently, such QRE probes do not show a smooth R_1 dispersion as opposed to currently used FFC-MRI CAs e.g. based on τ_R modulation of the paramagnetic relaxation enhancement (PRE), which show a smooth NMRD profile with a maximum in the mid-field region followed by a negative slope (see chapter 2.4.3). QRE as a central relaxation mechanism is an interesting alternative to established approaches for the tailored design of field-dependent MRI contrast agents paving the way from rather smooth R_1 dispersion to frequency-selective QRE patterns at clincial B_0 fields (Figure 5.1). In the following we will discuss the theory, current state and potential of QRE based probes from the MR imaging point of view.

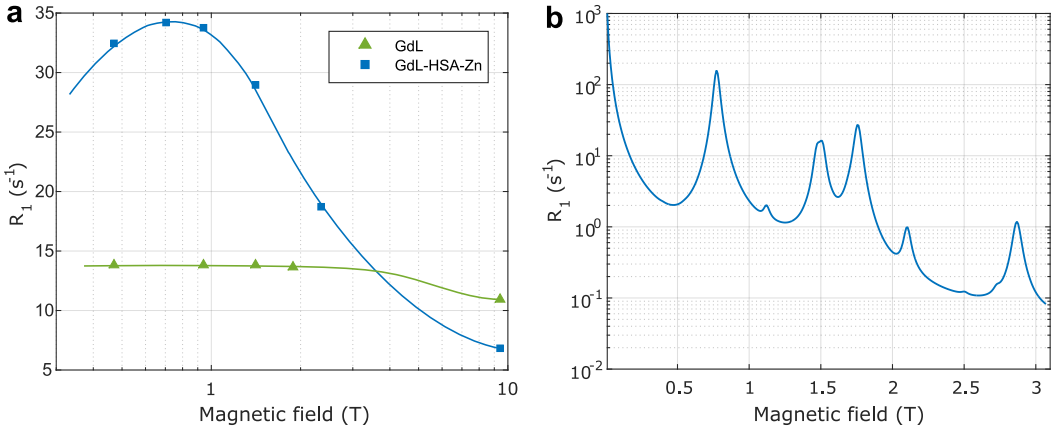

Figure 5.1: (a) ^{1}H R_1 dispersion profile of a CA (1 mM) based on τ_R modulation of the paramagnetic relaxation enhancement. (b) Simulated ^{1}H R_1 dispersion profile of a QRE based contrast agent containing ^{209}Bi; for details see Figures 4.2 and 2.9, respectively. The PRE probe exhibits a smooth dispersion whereas the simulated QRE probe shows frequency-selective characteristics.

5.2 Paramagnetic vs. Quadrupole Relaxation Enhancement

5.2.1 Paramagnetic Relaxation

Paramagnetic contrast agents are complexes composed of a metal ion with unpaired electrons. They induce an increase in both longitudinal and transverse relaxation rates of water protons (or solvent protons in general) in the regions where they distribute. This effect is known as paramagnetic relaxation enhancement. PRE originates from dipole-dipole interactions between the electron spin of the paramagnetic species and the nuclear spin of water protons. Various metal ions could act as a paramagnetic center in PRE based probes, including Mn^{2+}, Mn^{3+}, Fe^{3+} and Gd^{3+}. Nowadays, Gd^{3+} chelates are the workhorses among contrast agents to improve diagnostic accuracy of clinical MRI examinations [4, 115]. This domination of Gd^{3+} relies on a strong paramagnetism due to seven unpaired electrons (i.e. a large magnetic moment) as well as relatively slow electronic relaxation. Both properties are favorable in terms of relaxation enhancement of water protons in the vicinity of the metallic center [60]. Relaxation theory of paramagnetic spin systems, in particular of Gd^{3+} complexes, is topic of extensive research and a detailed description can be found in several review articles [10, 116–120]. In the following we will focus on the mechanisms of action and parameters influencing the magnetic field dependency of R_1 of FFC-MRI contrast agents suitable for clinical fields. Although basically of interest as well, the effects of R_2 dispersion will be omitted here.

Gd^{3+}-based CAs are often referred to as T_1 agents as they predominantly shorten the longitudinal relaxation time leading to a bright signal in T_1-weighted images. The efficiency of such a CA can be described by its longitudinal relaxivity r_1, the longitudinal relaxation rate per 1 mM of contrast agent concentration $[CA]$. The observed water proton relaxation rate R_1^{obs} in presence of a CA is composed of the inherent relaxation rate of the tissue (or solvent) R_1^0 and the overall paramagnetic contribution $R_1^{PRE} = r_1[CA]$ (see equations (5.1) and (5.2)).

$$R_1^{obs} = R_1^0 + R_1^{PRE} \tag{5.1}$$

$$R_1^{obs} = R_1^0 + r_1[CA] \tag{5.2}$$

$$r_1 = r_1^{IS} + r_1^{SS} + r_1^{OS} \tag{5.3}$$

The relaxivity can be described by three terms arising from water molecules in each coordination sphere given in equation (5.3): the inner-sphere (IS), second-sphere (SS) and outer-sphere (OS) contributions [121]. The inner-sphere contribution originates from the relaxation of water protons directly coordinated to the paramagnetic center that are involved in chemical exchange with the bulk water. Some compounds (e.g. described in [122]) might form a second coordination sphere with water molecules not directly coordinated but located sufficiently close to the metallic center (<4 Å, [60]). The overall relaxivity of clinically approved contrast agents is composed of about 60% inner-sphere and 40% outer-

sphere relaxation. The outer-sphere contribution originates from a long-distance dipolar interaction of water molecules diffusing in the vicinity of the paramagnetic complex. The time scale of this mechanism is modeled by the translational (diffusional) correlation time $\tau_D = a^2/D$, which considers the relative diffusion coefficient D of solute and solvent and their distance of closest approach a depending on the molecular dimension and charge distribution of the compound [123, 124]. Although all contributions are important for optimizing the r_1 of a contrast agent, the inner-sphere effect offers the most versatile set of parameters to tune the paramagnetic relaxation enhancement. The inner-sphere contribution to relaxivity is denoted as

$$r_1^{IS} = \frac{q/[H_2O]}{T_{1m}^H + \tau_m}, \tag{5.4}$$

where q is the coordination number, $[H_2O]$ is the concentration of water (55 556 mM), τ_m is the mean lifetime of water molecules in the inner coordination sphere (with the water exchange rate given by $k_{ex} = 1/\tau_m$) and T_{1m}^H is the longitudinal relaxation time of inner-sphere protons. The relaxation rate $1/T_{1m}^H$ can be described by the Solomon-Bloembergen-Morgan theory [125–128] and is given by

$$\frac{1}{T_{1m}^H(B_0)} = \frac{2}{15}\left(\frac{\mu_0}{4\pi}\right)^2 \frac{\gamma_H^2 g^2 \mu_B^2 \; S(S+1)}{r_H^6} \left[\frac{3\tau_{c_1}}{1+\omega_H^2\tau_{c_1}^2} + \frac{7\tau_{c_2}}{1+\omega_S^2\tau_{c_2}^2}\right], \tag{5.5}$$

where μ_0 is the vacuum permeability, γ_H is the gyromagnetic ratio of the proton, g denotes the g-factor of the free electron (Landé factor), μ_B is the Bohr magneton and S is the spin quantum number ($S = 7/2$ for Gd^{3+}). The distance between the metallic center and coordinated water protons is given by r_H; ω_H and ω_S describe the Larmor frequencies (in $rad\ s^{-1}$) of the proton and electron, respectively. The overall correlation times τ_{c_1} and τ_{c_2} are composed of different contributions

$$\frac{1}{\tau_{c_i}} = \frac{1}{\tau_m} + \frac{1}{\tau_R} + \frac{1}{T_{ie}(B_0)} \qquad \text{with} \quad i = 1, 2\ , \tag{5.6}$$

where τ_R is the rotational correlation time of the hydrated complex and T_{1e} and T_{2e} are the longitudinal and transverse relaxation times of the electron spin, respectively. Equation (5.5) is constituted of two dispersive terms $3\tau_{c_1}/(1+\omega_H^2\tau_{c_1}^2)$ and $7\tau_{c_2}/(1+\omega_S^2\tau_{c_2}^2)$. With $\omega_H = \gamma_H B_0$ and $\omega_S = \gamma_S B_0$ this clearly shows the magnetic field dependency of the inner-sphere longitudinal relaxation time and consequently T_{1m}^H is a function of the main magnetic field of the MRI system i.e. $T_{1m}^H = f(B_0)$. Moreover, the electronic relaxation times T_{ie} in equation (5.6) are also a function of ω_S and therefore contribute to the field-dependent nature of T_{1m}^H (e.g. see [117, 129] for detailed theories).

In principle various molecular parameters can be tuned to optimize the efficiency of a PRE-based contrast agent (see Figure 5.2a): the number of coordinated water molecules q, the electron spin relaxation times T_{ie}, the metal-proton distance r_H, the water exchange rate $k_{ex} = 1/\tau_m$ and the rotational correlation time τ_R. As already noted in chapter 2.4.3,

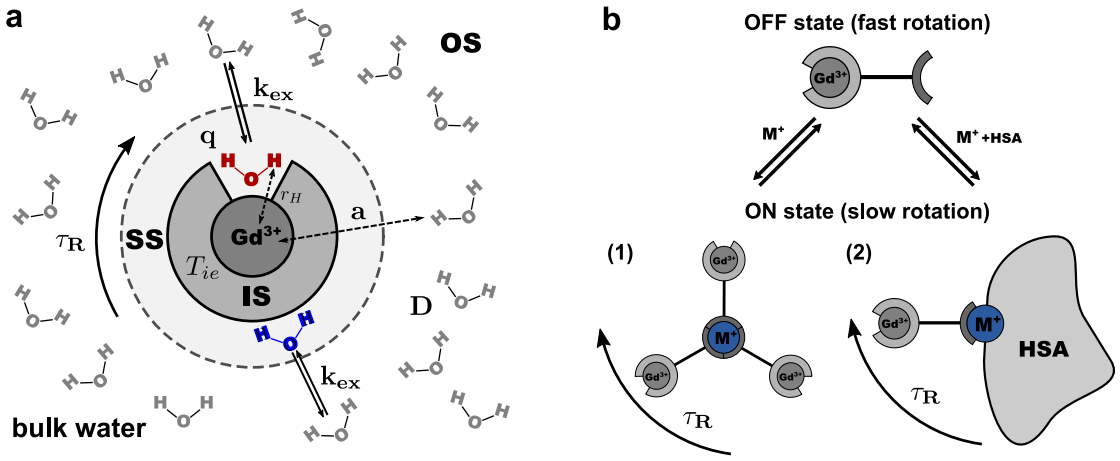

Figure 5.2: (a) Schematic illustration of a Gd^{3+} complex with corresponding coordination spheres of surrounding water molecules: inner-sphere (IS), second-sphere (SS) and outer-sphere (OS). The parameters that govern the paramagnetic relaxation enhancement are presented: number of coordinated water molecules q, Gd^{3+}-H distance r_H, relaxation times of the electron spin T_{ie} with $i = 1, 2$, rotational correlation time τ_R and diffusion coefficient D with distance of closest approach a. (b) Schematic principle of τ_R-modulation to render a contrast agent responsive to metal ions M^+. In addition to the Gd^{3+} chelate, the probe consists of a linker and a binding unit selective to the metal ion of interest. In the OFF state (low relaxivity) the system has a fast τ_R. τ_R is slowed down by forming a complex with higher molecular weight in the presence of M^+, either (1) by self-assembly around the metal ion or (2) by binding to a larger macromolecule such as HSA. The slowly tumbling system gives rise to an increased relaxivity i.e. a switch to the ON state.

modulating the rotational correlation time is the most promising for the design of dispersive FFC-MRI probes applicable in the clinical field range (1.5-3 T). Slowing down the rotational motion (i.e. increasing τ_R) of a complex is reflected by a peak in the R_1 NMRD profile located at intermediate fields between 0.5-1.5 T followed by a relatively steep downward slope towards 3 T. Slowly tumbling systems can be achieved by increasing the molecular weight, either by making the compound larger or by covalent or non-covalent binding to a large macromolecule (e.g. a protein, a polypetide, DNA, receptors of the cellular membrane, nanospheres, dendrimeres, micelles or liposomes [4, 118]). For example, the blood pool agent gadofosveset trisodium (also known as MS-325, Vasovist or Ablavar) shows a high affinity for human serum albumin (HSA). Upon HSA binding, MS-325 exhibits a relaxivity response characteristic for slowly tumbling systems and its slope at 1.5 T was first successfully exploited with FFC-MRI by Alford et al. [17]. Furthermore, τ_R modulation is also a central mechanism in the design of PRE-probes responsive to a biochemical stimulus. Coupling τ_R modulation e.g. to metal binding (via dedicated binding units, see Figure 5.2b) renders the relaxivity response activatable to the presence of metal ions such as Ca^{2+}, Cu^{2+} or Zn^{2+}, all playing a crucial role in cell signaling [90, 91, 99, 130]. Whereas currently available τ_R-based probes provide the best efficiency between 0.5-1.5 T, the benefit of slowly tumbling systems is diminished above 3 T for standard MRI techniques. In

chapter 4 we present the application of FFC-MRI to enable Zn^{2+} sensing at 3 T, while the detection of Zn^{2+} was not possible using conventional MRI [131].

5.2.2 Superparamagnetic Relaxation

Superparamagnetic iron oxide nanoparticles generally consist of an iron oxide core covered with a coating derived from an organic compound to avoid aggregation and guarantee biocompatibility. The core is usually formed by small crystallites such as magnetite (Fe_3O_4), maghemite (γ-Fe_2O_3) or hematite (α-Fe_2O_3) [132]. If an external magnetic field is applied, the iron ions align with the field leading to a magnetic moment three orders of magnitude higher than that of the individual paramagnetic ions. At zero field the particles exhibit no remnant magnetic moment i.e. they are no longer magnetic. The large magnetic moment of the superparamagnetic nanoparticle gives rise to local field inhomogeneities, which modulate the relaxation of water proton spins diffusing in the outer sphere of the iron oxide particle. The classical outer sphere theory from paramagnetic systems [124] is not directly applicable to the case of superparamagentic nanoparticles. A model was introduced by Roch et al. [133] including the magnetic properties of the particles such as the average size r, the saturation magnetization M_{sat}, the anisotropy energy of the crystal E_a and the Néel relaxation time τ_N. The large magnetic moment has favorable affects on increasing the transversal relaxivity, wherefore iron oxide nanoparticles are usually associated with negative T_2 contrast agents. However, it is important to note, that the contrast agent behavior is actually influenced by the r_2/r_1 ratio. Whereas typical T_2 agents have a large r_2/r_1 ratio, iron oxide particles that also have a strong r_1 characteristic (small r_2/r_1) can be used as T_1 or T_2 contrast agents depending on the MRI pulse sequence. [4, 115, 134]

In the context of FFC-MRI contrast agents, the r_1 NMRD profiles of iron oxide nanoparticles indicate auspicious properties in the clinical field range: a peak around 0.5 T followed by a steep slope towards high fields. Although the shape of the NMRD profile resembles with that of τ_R-based paramagnetic probes, the magnetic field dispersion of superparamangetic iron oxide particles originates from the aforementioned magnetic properties. A detailed analysis of parameters determining the shape of the NMRD profile can be found elsewhere [118, 135]. In short, important parameters that can be tuned to obtain a high $\Delta R_1/\Delta B_0$ for a given FFC-MRI field range are the average radius r and saturation magnetization M_{sat}. Reducing the size of the particle leads to a shift of the peak towards higher fields, but also to a reduced maximum while keeping the other parameters constant. In addition, an increase in M_{sat} gives rise to a general increase in relaxivity over the entire field range. Here, the applicability of iron oxide magnetic nanoparticles to FFC-MRI at 3 T ($\pm$100 mT) was shown in chapter 3. If one is interested in R_1 dispersion weighted images, it is noteworthy that the echo time should be minimized in order to reduce the influence of signal loss due to high r_2 of the superparamagnetic particles.

5.2.3 Quadrupole Relaxation

The relaxation enhancement of water protons for paramagnetic contrast agents originates from strong dipole-dipole interactions between the electron spin of the paramagnetic compound and adjacent water proton spins. In comparison, quadrupole relaxation enhancement is based on a frequency-selective dipole-dipole interaction between water proton spins and the nuclear spin of a quadrupole nucleus i.e. a nucleus with spin quantum number $S \geq 1$. The fluctuating dipole-dipole coupling acts as a path for a magnetization transfer from protons to the QN. The QN transfers the magnetization to the lattice, described by the quadrupole relaxation times T_{iQ} (with $i = 1, 2$), much faster than the proton alone. The primary condition of QRE, the so-called resonance condition, states that QRE becomes effective when the ^{1}H Larmor frequency matches one of the frequencies with high transition probability of the QN. This condition is mainly determined by the quadrupole coupling constant Q_{cc}, the asymmetry parameter η of the electrical field gradient (EFG) and the Zeeman splitting of the energy level systems. Other prerequisites for QRE are a close approach of protons to the QN (r_H of a few Å as the dipole-dipole coupling scales with $1/r_H^6$), sufficient water exchange rate $k_{ex} = 1/\tau_m$ and a proper timescale of the motional dynamics to enable efficient modulation of the dipole-dipole coupling [72, 76]. Grafting the

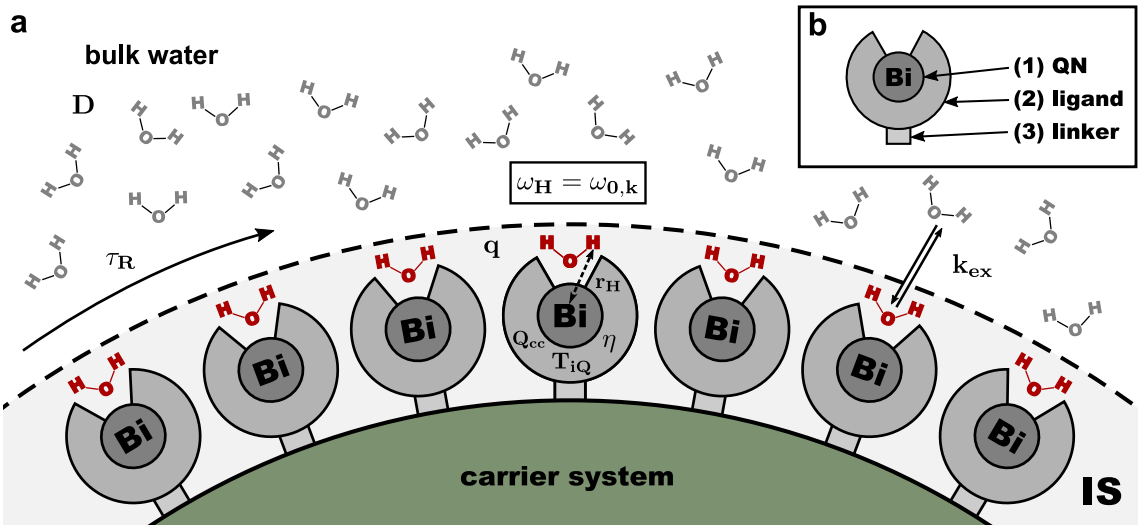

Figure 5.3: (a) Schematic illustration of the mechanism of a QRE contrast agent based on ^{209}Bi as quadrupole nucleus. QRE becomes effective if the resonance condition is satisfied, i.e., the ^{1}H Larmor frequency ω_H matches one of the frequencies with high transition probability of the QN $\omega_{0,k}$. The fluctuating dipole-dipole coupling than acts as path for magnetization transfer from water protons to the QN. Important parameters for efficient QRE are: the number of coordinated water molecules q in the inner sphere (IS), the QN-^{1}H distance r_H, the water exchange rate k_{ex} with diffusing water molecules in the bulk water (diffusion coefficient D), the pure quadrupole relaxation times T_{iQ} with $i = 1, 2$ and the rotational correlation time τ_R. The QRE core compound (b) can be linked to a carrier system (e.g. surface of a nanoparticle) to slow down the rotational motion of the complex.

QRE core compounds onto nanoparticles, or other carrier systems in general (e.g. micelles, liposomes, polymers, cyclodextrins), is required to slow down the motional dynamics, in particular the rotational motion described by τ_R, to guarantee that $\omega_{Q,k}\tau_R > 1$ is fulfilled. The mechanism of action and the parameters determining QRE are illustrated in Figure 5.3. As already discussed in chapter 2.4.4, to simulate the ^{1}H R_1 NMRD profile originating from QRE compounds dispersed in aqueous solution, the stochastic Liouville approach [72, 74, 75] is necessary (see Figure 2.9). Such a simulation environment is an important step towards the rational design of QRE-based probes to predict the amplitude, lineshape and position of QRE peaks of promising compounds.

5.2.4 Tuning of the QRE Resonance Condition

The resonance condition for QRE can be formulated as

$$\omega_H = \omega_{0,k} \tag{5.7}$$

where $\omega_H = \gamma_H B_0$ is the proton Larmor frequency and $\omega_{0,k}$ is one of the allowed transition frequencies k of the QN-transition bands. In an external magnetic field B_0, protons and QN undergo a Zeeman splitting of their energy level systems. The pure quadrupole transition frequencies $\omega_{Q,k}$ from zero-field (nuclear quadrupole resonance (NQR) transition frequencies) broaden to characteristic QN-transition bands $\omega_{0,k}$ with increasing B_0. The transition bands result from the total QN Hamiltonian and therefore depend on the angle Ω between the EFG and the direction of B_0. The molecular rotation of the complex in solution leads to a dynamic fluctuation of this angle i.e. $\Omega(t)$. Equation 5.7 states that for transition crossings between the proton Larmor frequency and the QN-transition bands the resonance condition is met and leads to regions where QRE can occur (see Figure 5.5).

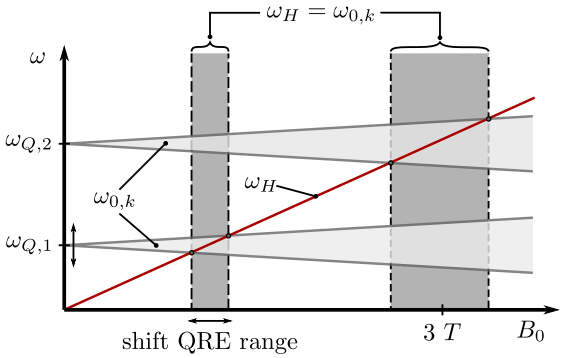

Figure 5.4: QRE becomes active if the resonance condition is satisfied i.e. the proton Larmor frequency ω_H matches the QN-transition bands $\omega_{0,k}$ depending on the external magnetic field B_0. The pure quadrupole frequencies $\omega_{Q,k}$ can be tuned to shift the regions of possible QRE to the desired B_0 as illustrated here for 3 T.

The pure quadrupole transition frequencies $\omega_{Q,k}$ can be characterized by zero-field nuclear quadrupole resonance spectroscopy (NQRS). The NQR spectra are a consequence of the coupling of the quadrupole moment of the QN with the EFG created by its surrounding electrical charge distribution. The emerging NQR frequency spectrum can be fully characterized by Q_{cc} and η (asymmetry parameter of the EFG). The number of transitions depends on the spin quantum number e.g. for $I = 9/2$ nuclei like ^{209}Bi four NQR peaks are present. The positions of $\omega_{Q,k}$ are sensitive to the electronic environment of the QN. Therefore, by structural or chemical changes (e.g. choice of the ligands), the transition frequency of the QN can be tuned to a desired frequency. In further consequence, the regions of possible QRE can be shifted towards the B_0 field of interest, e.g. 1.5 T or 3 T.

5.3 Proof of Concept: First QRE in ^{209}Bi compounds

Selection criteria for the identification of suitable QN for the development of prospective contrast agents for the clinical field range are: (1) high gyromagnetic ratio γ_{QN} to ensure a strong dipole-dipole coupling, (2) high spin quantum number I as R_1 is proportional to I and offers more possible quadrupole transition frequencies [72], (3) appropriate Q_{cc} to meet the resonance condition at clinical field strengths of 1.5 T or 3 T, (4) slow enough pure quadrupole relaxation to allow for an efficient magnetization transfer (5) promising biocompatibility, (6) high natural abundance and well-known chemistry. The QRE active molecules investigated in CONQUER are based on aryl compounds of ^{209}Bi, a quadrupole nucleus that satisfies the aforementioned criteria, most of all the requirement of a high spin quantum number of $I = 9/2$ and high Q_{cc}. Furthermore, toxicity studies of bismuth compounds show a promising biocompatibility [136, 137]; such compounds are already used in therapeutic treatment of gastrointestinal disorders [138]. Dextran-coated bismuth-iron oxide nanoparticles used as nanohybrid contrast agents for computed tomography and MRI were found to be biodegradable and biocompatible [139].

FFC-NMR studies of several of the investigated ^{209}Bi core compounds in solid state (powder samples) exhibit characteristic QRE patterns between 0.5 T and 3 T [73, 76]. QRE in the liquid state could also be observed for tris(2-methoxyphenyl)bismuth dissolved in tetrahydrofuran (THF) [140] and even in aqueous dispersion of nanoparticles constituted of triphenylbismuth nanocrystallites coated with polyvinylpyrrolidone (PVP) [141, 142]; the measured ^{1}H R_1 NMRD profiles can be found in Figure 5.5. The tris(2-methoxyphenyl)bismuth molecules in THF are assumed to form (uncontrolled) clusters slowing down the rotational correlation time τ_c. This slower rotation compared to the single molecules probably leads to the observed QRE pattern in Figure 5.5a, where two distinct peaks emerge above 1.5 T. An important prerequisite for the use as MRI contrast agent is water solubility. Therefore, the triphenylbismuth NPs were coated with PVP and dissolved in water. QRE peaks could be detected for particles with average hydrodynamic diameter of 750 nm, whereas the 400 nm sized NPs show considerable smoothing presumably due to faster rotation (Figure 5.5b).

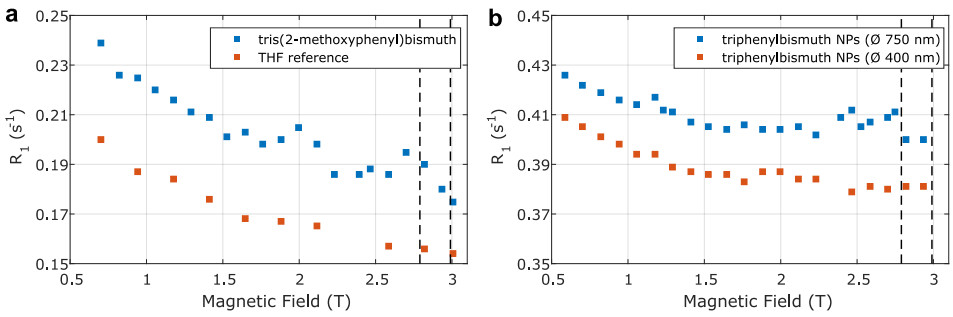

Figure 5.5: (a) Measured ^{1}H R_1 NMRD profiles of tris(2-methoxyphenyl)bismuth) dissolved in THF [140]. In comparison to the THF reference, distinct QRE peaks are visible. (b) ^{1}H R_1 NMRD profiles of nanoparticles constituted out of triphenylbismuth nanocrystallites coated with PVP and dissolved in water [141, 142]; average hydrodynamic diameter of 400 nm and 750 nm. The 750 nm sized NPs show QRE peaks close to the field-cycling range of 2.89 T ±100 mT (dashed vertical lines); all measurements were performed at 293 K.

Important considerations from the imaging point of view are the location and shape of the QRE peaks (height and width), i.e., the achievable $\Delta R_1/\Delta B_0$ in the accessible FFC range. Although the observed QRE maxima are close to the FFC range of 2.89 T ±100 mT, none of them lie directly within this range. However, for tris(2-methoxyphenyl)bismuth dissolved in THF, the $\Delta R_1/\Delta B_0$ can be approximated from two data points within 2.89 T ±100 mT and gives a value of $-0.08\ s^{-1}T^{-1}$. Unfortunately, this value lies below the resolution limit of the FFC-MRI system of $0.14\ s^{-1}T^{-1}$ (estimated in chapter 4.4.3), making imaging experiments with the current hardware system and compounds unfeasible. Although the relaxation enhancement in liquids is still inefficient due to suboptimal particle properties (e.g. wide size distribution), the occurrence of QRE peaks in the clinical field range is an essential breakthrough in the development of MRI contrast agents based on quadrupole relaxation enhancement. It is to be expected, that by optimizing the nanoparticles with respect to maximum enhancement and tuning of the QRE position will finally lead to feasible imaging experiments.

5.4 Prospective Impact on Molecular MRI

In the context of MRI, the first step towards the application as a contrast agent is the validation of the frequency-selective nature of QRE compounds by FFC-MRI. Prospective QRE probes are required to provide pronounced QRE peaks within currently available FFC ranges around clincical relevant field strengths of 1.5 T [18, 47, 78] and 3 T [31]. Distinct QRE peaks emerging within this ranges can be exploited by cycling the B_0 field to generate switchable image contrast based on differential imaging between a high (activated) and low (inactivated) relaxivity state. Currently used FFC-MRI probes show a smooth NMRD profile with a maximum in the mid-field region followed by a negative slope. In contrast, prospective QRE probes show no smooth dispersion but rather several peaks emerging in

the clinical field range leading to a frequency-selective nature.

The position of QRE peaks is determined by the QN-transition bands $\omega_{0,k}$. The dependence of $\omega_{0,k}$ on the electrical field gradient paves the way towards the design of molecular probes responsive to changes in the chemical environment of the quadrupole nucleus. It is conceivable to change image contrast by altering the conformational structure of the molecule e.g. when binding to a target. The choice of ligands surrounding the QN stronlgy influences the EFG and therefore Q_{cc}. In [76], for a variety of bismuth-aryl compounds the NQR parameters Q_{cc} and η have been experimentally characterized. Frequency shifts of Q_{cc} from -10.8 MHz up to 400 MHz with respect to triphenylbismuth ($Q_{cc} = 668.3\ MHz$) have been observed depending on the substituent and its molecular position. Based on these ligand induced frequency shifts, applications for QRE enhancement in conventional MR scanners without field-cycling equipment might be possible. An EFG change due to chemical interaction e.g. by targeting could shift the QRE peak to or from the fixed Larmor frequency of the MRI system, thus producing image contrast. Such an application would be highly desirable as it would not require dedicated hardware modifications for field-cycling and could be directly used with conventional MRI systems.

An important consideration for narrow QRE peaks within the FFC range is that one could either utilize a negative or positive slope to generate image contrast. As the background tissue shows a rather weak and negative dispersion [47], the utilization of a positive slope leads to an unambiguous localization of the QRE probe. Although, a positive R_1 dispersion is conceivable but not yet achieved for other FFC-MRI contrast agents, it would require a shift of the maximum beyond the clinical field range. Furthermore, using two or more QRE probes, each with a peak located within the FFC range but clearly separable from another, one could think of multi-spectral imaging. A simultaneous tracking of multiple probes or even different biological processes could become possible by selective activation via B_0 field-cycling.

Nano carrier systems are required to establish the necessary motional dynamics of the QN core compound for efficient dipole-dipole coupling. The particular choice of carrier systems offers various possibilities for combining molecular imaging with drug delivery, i.e., theranostic applications. Incorporating QN core compounds e.g. in self-assembled lipid based structures like liposomes could be one strategy along this path. Liposomes are widely studied and can serve as host for hydrophilic, hydrophobic and amphiphilic substances [143–145]. Their amphiphilic character allows for a proper distribution of the QN core compound to the desired target site when also combined with a targeting agent. Furthermore, one could also think of the design of multi-modal contrast agents by combining the QN core compound with dedicated nanoparticles with capabilities for other established molecular imaging modalities. For instance, it is conceivable to graft the QN core compounds onto the surface of gold nanoparticles, which are currently investigated as possible contrast agents for x-ray imaging and computed tomography [146].

6

Conclusions and Future Prospects

> *Before I came here, I was confused about this subject. Having listened to your lecture, I am still confused - but on a higher level.*
>
> Enrico Fermi, *1901-1954*

This thesis presents the worldwide first application of fast field-cycling within a clinical MRI system operating at a main magnetic field strength of 3 T. The focus lies on how to generate MR image contrast from molecular targets based on the nuclear magnetic relaxation dispersion of the longitudinal relaxation rate of specific MRI contrast agents. In the following, a summarized discussion of the key results and future prospects shall be given.

Fast field-cycling complements MRI by an additional dimension as it allows for a modulation of the B_0 field during the pulse sequence. In conventional MRI, on the contary, B_0 cannot be altered and is fixed to the nominal value of the magnet system. Implementing FFC-MRI systems is accompanied by various design constraints regarding magnet design, B_0 field stability and homogeneity, power supply, control electronics, scan time and image quality. Depending on the FFC range one wants to investigate, different approaches may be employed to enable field-cycling during a pulse sequence. The low field region of the NMRD profile can be accessed either by using only a single resistive magnet or by combining a permanent magnet for the acquisition field with a resistive one for the evolution field. In the clinical field range FFC-MRI is implemented by means of an insert coil together with the superconducting magnet provided by a commercial MRI system. This approach for field-cycling is also known as delta relaxation enhanced MR (dreMR).

So far, only clinical 1.5 T systems were equipped with a B_0 insert coil [18, 29, 77, 78]. Part of this thesis is devoted to the adaptation of a 3 T MRI system (Skyra, Siemens Healthineers) for fast field-cycling. The dedicated B_0 insert coil operates with a maximum FFC range of $\pm$100 mT centered around the nominal B_0 field strength, which is actually 2.89 T for the Skyra system. Adverse effects compromising FFC-MRI image quality were characterized and successfully mitigated. In particular, the output noise current of the gradient power amplifier and eddy currents induced by fast ramping of the B_0 field have been identified as primary sources of image degradation. The former is circumvented by a dedicated control signal to disable the GPA during image acquisition. The latter are characterized by sampling the eddy current decay curve using an adapted multi-phase spoiled gradient echo sequence [30] and consequently compensated using the eDREAM method [45]. These countermeasures lead to an image quality on par with images acquired without field-cycling. All together the fast field-cycling technique was successfully established and expands the variety of available FFC ranges towards a clinical field strength of 3 T.

FFC-MRI at clinical field strengths predominantly relies on dispersive properties of contrast agents, preferably a steep slope in the NMRD profile of the longitudinal relaxation rate within the accessible FFC range i.e. a high $\Delta R_1/\Delta B_0$. Superparamagnetic iron oxide nanoparticles and slowly tumbling paramagnetic systems indicate both auspicious $\Delta R_1/\Delta B_0$ values around 1.5 T and 3 T. Unfortunately, the commercial availability of clinically approved dispersive contrast agents is limited. Notwithstanding, among various imaging probes, which are currently subject of basic research in academia, part of them exhibit dispersive properties suitable for the respective FFC range. These contrast agents may be procured in cooperation with the responsible academic sites.

Two main approaches can be utilized to render paramagnetic systems activatable in response to a specific biomarker: modulating either the coordination number q, or the rotational correlation time τ_R. While for the q-modulation the relaxivity response is roughly constant with respect to the magnetic field, for τ_R-modulation the response is highly field-dependent. The latter provides the highest relaxivity change between the activated and inactivated state for intermediate fields ranging from 0.5 T to 1.5 T. Towards higher magnetic fields of 3 T and above the benefit of τ_R-based probes is attenuated as the longitudinal relaxivity decreases considerably with increasing field strength [90]. Here, we propose FFC-MRI as a means to overcome this drawback for high fields. The τ_R-based probe used herein displays an increased binding affinity to human serum albumin only in the presence of Zn^{2+}. Compared to gadofosveset trisodium, which directly binds to serum albumin without the presence of any metal ions, our probe informs about HSA bound zinc ions. Zinc is vital for a wide range of cellular processes and missregulations in Zn^{2+} homeostasis are linked to diabetes, cancers and neurodegenerative disease such as Alzheimer's disease. With FFC-MRI the change of the slope in the R_1 NMRD profile upon activation is quantified, rather than the absolute difference of R_1 for a fixed B_0. This enables the detection of zinc levels down to 60 μM at 3 T with FFC-MRI, while detection with conventional MRI

is not possible at all. Moreover, the phantom study showed a linear increase of $\Delta R_1/\Delta B_0$ with increasing zinc concentration. These findings might provide unprecedented opportunities for the quantification of zinc and will be subject of further investigations beyond the scope of this thesis.

Signal to noise ratio considerations are an important issue for FFC-MRI. Low field systems operate with typical acquisition fields of 0.2 T limiting the SNR compared to conventional clinical fields [16]. Nevertheless, the inherently pronounced R_1 dispersion of biological tissues and reported endogenous biomarkers for a variety of pathologies below 0.2 T [14, 15, 147–149], may be a worthwhile compromise for higher SNR provided by clinical acquisition fields. The step from 1.5 T to 3 T theoretically comes along with a twofold increase in SNR for the individual images. Since FFC-MRI at high fields predominantly relies on the NMRD characteristics of contrast agents, the potential benefit of increased SNR may be compensated by a reduced R_1 dispersion at 3 T. Whether an acquisition field of 1.5 T or 3 T is more advantageous for FFC-MRI images strongly depends on the respective contrast agent in use. As already mentioned, current dispersive contrast agents display their maximum R_1 in the intermediate field range. Shifting this peak towards higher fields would also lead to an increased R_1 dispersion at 3 T. Moreover, a R_1 dispersion weighted image in dreMR is obtained by subtracting two images with different evolution fields and the magnitude of the dreMR signal is rather small (e.g. about 2.5% in Figure 3.7) in comparison to the individual images. Therefore, FFC-MRI may benefit from dedicated denoising approaches to increase the SNR. For instance, dreMR imaging bears strong resemblance with arterial spin labeling (ASL) perfusion imaging which is also based on image subtraction. In ASL a perfusion weighted image is generated by calculating the difference between label and control image. To overcome the SNR limitation, Spann et al. proposed a spatial-temporal filtering approach based on variational regularization [150]. The inherent information of both label and control images is exploited simultaneously for denoising. This can be directly transfered to the problem of dreMR image denoising by replacing label and control pairs with image pairs acquired at $B_0 \pm \Delta B_0$. Thereby, spatial similarities of the field-shifted images may be jointly integrated in the denoising algorithm. Preliminary unpublished results suggest that joint TGV denoising of field-shifted images may serve as a promising means to increase SNR for dreMR imaging. Whether such denoising approaches could aid a more sensitive detection of biomarkers, e.g. below the 60 μM detection limit of Zn^{2+} reported in this thesis, shall be subject of future studies. The application of joint TGV denoising of field-shifted images is not limited to dreMR imaging, but may also be adapted to improve the detection of endogenous biomarkers accessible with low field FFC-MRI.

All studies presented in this thesis were conducted in vitro. Translating the potential of these proof-of-concept experiments to preclincial small animal trials, is a crucial step towards the establishment of FFC-MRI as a molecular imaging modality. In vivo applications of FFC-MRI may be impaired by prolonged scan times to ensure sufficient SNR. Accel-

erating image acquisition is therefore necessary to reduce the duration of the FFC-MRI imaging protocol to reasonable levels. Extensive research is devoted to speed up acquisition time for conventional MRI, however, not all acceleration methods are directly applicable to FFC-MRI due to additional hardware constraints. With our system, the TR of a pulse sequence is constrained by the enable time of the GPA blanking (i.e. 20 ms). Magnetization prepared spin echo sequences require TRs of about 5 T_1 to guarantee full relaxation to the equilibrium magnetization. This timing constraint is therefore not a limiting factor with such sequences. Repetition times in the range of the GPA enable time would require other strategies to cope with random phase fluctuations during k-space acquisition [29, 41]. Faster imaging modules like RARE have been applied to FFC-MRI with echo train lengths of up to 4 without image degradation [46, 47]. The adaptation of a turbo spin echo (TSE) sequence is subject of ongoing work and crucial to reduce the scan time to reasonable levels for future in vivo experiments with our FFC-MRI system. The imaging volume provided by our specifically designed RF coil is suitable for small animals; it only has to be supplemented with dedicated small animal equipment like mouse cradle or life support and monitoring systems. The amplifier duty-cycle is not expected to be a limiting factor as it is specified for a continuous operation of the B_0 insert coil with 100 mT field shifts. In vivo imaging artefacts associated with free breathing motion of the anesthetized small animal and partial volume effects have to be considered as well. Despite these additional constraints compared to conventional MRI, the feasibility of in vivo FFC-MRI has already been shown at 1.5 T [45, 47, 77] and should be directly applicable to 3 T.

Molecular probes utilizing quadrupolar relaxation enhancement are regarded as a novel idea compared to state-of-the-art MRI contrast agents. QRE based probes may lead the way from rather smooth NMRD profiles, as provided by paramagnetic and superparamagnetic relaxation enhancement, towards frequency-selective NMRD characteristics in the clinical field range of 1.5 T to 3 T. The project CONQUER focused on the investigation of aryl-bismuth derivatives with ^{209}Bi as quadrupole nucleus. ^{209}Bi offers favorable properties for the targeted field strength of 3 T such as a high spin quantum number of $I = 9/2$, high quadrupole coupling constant, high gyromagnetic ratio, promising biocompatibility and well-known chemistry. FFC-NMR relaxometry studies of several compounds have indicated the feasibility of QRE in the solid and liquid state with distinguishable QRE peaks in the clinical field range. These results demonstrate the first proof-of-principle of QRE as a central mechanism for the design of novel frequency-selective contrast agents. Despite these promising results, the observed QRE features in liquids were, due to suboptimal particle properties, below the detection limit of the FFC-MRI system. Optimizing nanoparticle design, or the carrier system of the core compounds in general, is mandatory to increase the QRE efficiency to feasible levels for imaging. Essential aspects that should be considered for efficient QRE are: (1) an appropriate ligand selection to tune the QN-transition bands for the targeted Larmor frequency given by the MRI system, (2) a close approach of water protons to the QN,

(3) slow particle dynamics and sufficient water exchange with bulk water protons, and (4) the structural order of the QN ensemble should provide a narrow distribution of the EFG to yield sharp QRE peaks. The deficient properties of the current nanoparticles, such as wide size distribution and inefficient surface/volume ratio, require a complete re-design of the carrier system. It is anticipated that by taking into account the aforementioned key aspects, the optimization of the carrier system will eventually lead to feasible imaging experiments, which shall be subject of future work in follow-up projects.

In conclusion, this thesis contributes to advance the field of molecular MRI. We have shown the first application of fast field-cycling within a clinical MRI system operating at field strength of 3 T. This enables access to field-dependent MRI contrast which would be otherwise hidden for conventional MRI. It can potentially add value to the detection of various biomarkers as was shown here for the specific case of zinc detection. Moreover, quadrupole relaxation enhancement has been proposed as a fundamentally new approach for the design of MRI contrast agents, ushering the way towards unprecedented frequency-selective nuclear magnetic relaxation dispersion in the clinical field range.

A

List of Acronyms

ASL	arterial spin labeling
BW	bandwidth
CA	contrast agent
CI	confidence intervall
CNR	contrast-to-noise ratio
CONQUER	contrast by quadrupole enhanced relaxation
CPMG	Carr-Purcell-Meiboom-Gill
DPA	bis(pyridinylmethyl)amine
dreMR	delta relaxation enhanced magnetic resonance
eDREAM	eddy current compensation by dynamic reference phase modulation
EFG	electric field gradient
FFC	fast field-cycling
FFC-MRI	fast field-cycling magnetic resonance imaging
FFC-NMR	fast field-cycling nuclear magnetic resonance
FID	free induction decay
FLASH	fast low-angle shot
FOV	field of view
GPA	gradient power amplifier
GRE	gradient echo
HEPES	4-(2-hydroxyethyl)-1-piperazineethanesulfonic acid
HRMS	high resolution mass spectrometry
HSA	human serum albumin
ICP-MS	Inductively Coupled Plasma - Mass Spectrometry
IOMNP	iron oxide magnetic nanoparticle
IR	inversion recovery

IS	inner-sphere
MI	molecular imaging
MR	magnetic resonance
MRI	magnetic resonance imaging
NMR	nuclear magnetic resonance
NMRD	nuclear magnetic relaxation dispersion
NQR	nuclear quadrupole resonance
NQRS	nuclear quadrupole resonance spectroscopy
OS	outer-sphere
PI	parallel imaging
PRE	paramagnetic relaxation enhancement
QN	quadrupole nuclei
QRE	quadrupole relaxation enhancement
RARE	Rapid Acquisitions with Refocused Echos
RF	radio frequency
ROI	region of interest
SE	spin echo
SNR	signal-to-noise ratio
SQUID	superconducting quantum interference device
SR	saturation recovery
SS	second-sphere
TE	echo time
TEM	transmission electron microscopy
TFA	trifluoroacetic acid
TGV	total generalized variation
THF	tetrahydrofuran
TR	repetition time
TSE	turbo spin echo

B

List of Publications

Peer-Reviewed Journal Publications

1. **M. Bödenler**, K. P. Malikidogo, J.-F. Morfin, C. S. Aigner, É. Tóth, C. S. Bonnet, and H. Scharfetter. High-Field Detection of Biomarkers with Fast Field-Cycling MRI: The Example of Zinc Sensing. *Chemistry - A European Journal* 25 (2019) 8236-8239, https://doi.org/10.1002/chem.201901157

2. **M. Bödenler**, L. de Rochefort, P. J. Ross, N. Chanet, G. Guillot, G. R. Davies, C. Gösweiner, H. Scharfetter, D. J. Lurie, and L. M. Broche. Comparison of fast field-cycling magnetic resonance imaging methods and future perspectives. *Molecular Physics* 117 (2019) 832-848, https://doi.org/10.1080/00268976.2018.1557349

3. **M. Bödenler**, M. Basini, M. F. Casula, E. Umut, C. Gösweiner, A. Petrovic, D. Kruk, and H. Scharfetter. R_1 dispersion contrast at high field with fast field-cycling MRI. *Journal of Magnetic Resonance* 290 (2018) 68-75, https://doi.org/10.1016/j.jmr.2018.03.010

4. C. Gösweiner, D. Kruk, E. Umut, E. Masiewicz, **M. Bödenler**, and H. Scharfetter. Predicting quadrupole relaxation enhancement peaks in proton R_1-NMRD profiles in solid Bi-aryl compounds from NQR parameters. *Molecular Physics* 117 (2019) 910-920, https://doi.org/10.1080/00268976.2018.1519201

5. C. Gösweiner, P. Lantto, R. Fischer, C. Sampl, E. Umut, P.-O. Westlund, D. Kruk, **M. Bödenler**, S. Spirk, A. Petrovic, and H. Scharfetter. Tuning Nuclear Quadrupole Resonance: A Novel Approach for the Design of Frequency-Selective MRI Contrast Agents. *Phys. Rev. X* 8 (2018) 021076, https://link.aps.org/doi/10.1103/PhysRevX.8.021076

6. H. Scharfetter, **M. Bödenler**, and D. Narnhofer. A cryostatic, fast scanning, wideband NQR spectrometer for the VHF range. *Journal of Magnetic Resonance* 286 (2018) 148-157, https://doi.org/10.1016/j.jmr.2017.12.004

Peer-Reviewed Conference Proceedings

1. **M. Bödenler**, M. Basini, M. F. Casula, E. Umut, D. Kruk, and H. Scharfetter. Implementation and validation of delta relaxation enhanced MRI at 3T: A system for quadrupole enhanced relaxation imaging. In *Proc. Intl. Soc. Mag. Reson. Med.* 26 (2018)

2. **M. Bödenler**, M. Basini, M. F. Casula, E. Umut, and H. Scharfetter. High Field FFC-MRI: System Validation with Iron Oxide Magnetic Nanoparticles. In *Conference on NMR Relaxometry and Related Methods* (2018)

3. C. Gösweiner, D. Kruk, P.-O. Westlund, R. Fischer, M. Schlögl, **M. Bödenler**, A. Petrovic, S. Spirk, and H. Scharfetter. Extrinsic MRI Contrast Agents Based on Nuclear Quadrupole Enhanced Relaxation: Principle, Requirements and Characterization of Promising Compounds. In *Proc. Intl. Soc. Mag. Reson. Med.* 25 (2017)

4. **M. Bödenler** and H. Scharfetter. High Field FFC-MRI - A First System for 3T. In *Proceedings of the 34th Annual Meeting of ESMRMB* (2017)

5. **M. Bödenler** and H. Scharfetter. High Field FFC-MRI - A System for 3T: Initial Experience. In *1st Workshop on Nuclear Magnetic Resonance Relaxometry* (2017)

6. **M. Bödenler**, M. Botta, and H. Scharfetter. High Field FFC-MRI with Citrate-Coated GdF3 Nanoparticles: Preliminary Results at 3T. In 1*0th Conference on Fast Field-Cycling NMR Relaxometry* (2017)

7. **M. Bödenler**, C. S. Aigner, A. Rund, and R. Stollberger. Fast Optimization of RF Excitation. In *Proceedings of the 33th Annual Meeting of ESMRMB* (2016)

Oral Presentations

1. **M. Bödenler**, M. Basini, M. F. Casula, E. Umut, and H. Scharfetter. High Field FFC-MRI: System Validation with Iron Oxide Magnetic Nanoparticles. *Conference on NMR Relaxometry and Related Methods*, Turin, Italy, January, 2018

2. **M. Bödenler** and H. Scharfetter. High Field FFC-MRI - A First System for 3T. *34th Annual Meeting of ESMRMB*, Barcelona, Spain, October, 2017

3. **M. Bödenler** and H. Scharfetter. High Field FFC-MRI - A System for 3T: Initial Experience. *1st Workshop on NMR Relaxometry*, Olsztyn, Poland, February, 2017

4. **M. Bödenler**, M. Botta, and H. Scharfetter. High Field FFC-MRI with Citrate-Coated GdF3 Nanoparticles: Preliminary Results at 3T. *10th Conference on Fast Field-Cycling NMR Relaxometry*, Mikolajki, June, 2017

5. **M. Bödenler**, C. S. Aigner, A. Rund, and R. Stollberger. Fast Optimization of RF Excitation. *33th Annual Meeting of ESMRMB*, Vienna, Austria, October, 2016

Bibliography

[1] M. L. James and S. S. Gambhir. A Molecular Imaging Primer: Modalities, Imaging Agents, and Applications. *Physiological Reviews*, 92(2):897–965, 2012, https://doi.org/10.1152/physrev.00049.2010. (page 1)

[2] H. R. Herschman. Molecular Imaging: Looking at Problems, Seeing Solutions. *Science*, 302(5645):605–608, 2003, https://science.sciencemag.org/content/302/5645/605. (page 1)

[3] M. M. J. Modo and J. W. M. Bulte, editors. *Molecular and Cellular MR Imaging*. CRC Press Taylor & Francis Group, 2007. (page 1)

[4] J. Wahsner, E. M. Gale, A. Rodríguez-Rodríguez, and P. Caravan. Chemistry of MRI Contrast Agents: Current Challenges and New Frontiers. *Chemical Reviews*, 119(2):957–1057, jan 2019, https://doi.org/10.1021/acs.chemrev.8b00363. (page 1, 51, 63, 65, 66)

[5] G.-L. Davies, I. Kramberger, and J. J. Davis. Environmentally responsive MRI contrast agents. *Chem. Commun.*, 49(84):9704–9721, 2013, http://dx.doi.org/10.1039/C3CC44268C. (page 2)

[6] A. Louie. MRI biosensors: A short primer. *Journal of Magnetic Resonance Imaging*, 38(3):530–539, 2013, https://onlinelibrary.wiley.com/doi/abs/10.1002/jmri.24298. (page)

[7] D. V. Hingorani, A. S. Bernstein, and M. D. Pagel. A review of responsive MRI contrast agents: 2005-2014. *Contrast Media & Molecular Imaging*, 10(4):245–265, 2015, https://onlinelibrary.wiley.com/doi/abs/10.1002/cmmi.1629. (page 2)

[8] E. Vinogradov. Imaging molecules. *Journal of Magnetic Resonance*, jul 2019, https://www.sciencedirect.com/science/article/pii/S1090780719301399?via{%}3Dihub{#}b0210. (page 2)

[9] P. C. van Zijl, W. W. Lam, J. Xu, L. Knutsson, and G. J. Stanisz. Magnetization Transfer Contrast and Chemical Exchange Saturation Transfer MRI. Features and analysis of the field-dependent saturation spectrum. *NeuroImage*, 168:222–241, mar 2018, https://www.sciencedirect.com/science/article/pii/S1053811917303403?via{%}3Dihub. (page 2)

[10] D. Kruk. Chapter 2 Essentials of the Theory of Spin Relaxation as Needed for Field-cycling NMR. In *Field-cycling NMR Relaxometry: Instrumentation{,} Model Theories and Applications*, pages 42–66. The Royal Society of Chemistry, 2019, http://dx.doi.org/10.1039/9781788012966-00042. (page 2, 63)

[11] J.-P. Korb. Multiscale nuclear magnetic relaxation dispersion of complex liquids in bulk and confinement. *Progress in Nuclear Magnetic Resonance Spectroscopy*, 104:12–55, feb 2018, https://www.sciencedirect.com/science/article/pii/S0079656517300353. (page 2)

[12] L. M. Broche, S. R. Ismail, N. A. Booth, and D. J. Lurie. Measurement of fibrin concentration by fast field-cycling NMR. *Magnetic Resonance in Medicine*, 67(5):1453–1457, oct 2011, https://doi.org/10.1002/mrm.23117. (page 2, 23)

[13] L. M. Broche, G. P. Ashcroft, and D. J. Lurie. Detection of osteoarthritis in knee and hip joints by fast field-cycling NMR. *Magnetic Resonance in Medicine*, 68(2):358–362, 2012. (page 7, 23, 37)

[14] M. R. Ruggiero, S. Baroni, S. Pezzana, G. Ferrante, S. Geninatti Crich, and S. Aime. Evidence for the Role of Intracellular Water Lifetime as a Tumour Biomarker Obtained by In Vivo Field-Cycling Relaxometry. *Angewandte Chemie International Edition*, 57(25):7468–7472, jun 2018, https://doi.org/10.1002/anie.201713318. (page 27, 75)

[15] E. Di Gregorio, G. Ferrauto, S. Lanzardo, E. Gianolio, and S. Aime. Use of FCC-NMRD relaxometry for early detection and characterization of ex-vivo murine breast cancer. *Scientific Reports*, 9(1):4624, 2019, https://doi.org/10.1038/s41598-019-41154-9. (page 2, 75)

[16] L. M. Broche, P. J. Ross, G. R. Davies, M.-J. MacLeod, and D. J. Lurie. A whole-body Fast Field-Cycling scanner for clinical molecular imaging studies. *Scientific Reports*, 9(1):10402, 2019, https://doi.org/10.1038/s41598-019-46648-0. (page 2, 75)

[17] J. K. Alford, B. K. Rutt, T. J. Scholl, W. B. Handler, and B. A. Chronik. Delta relaxation enhanced mr: Improving activation - Speeificity of molecular probes through R 1 dispersion imaging. *Magnetic Resonance in Medicine*, 61(4):796–802, 2009. (page 2, 24, 30, 46, 65)

[18] U. C. Hoelscher, S. Lother, F. Fidler, M. Blaimer, and P. Jakob. Quantification and localization of contrast agents using delta relaxation enhanced magnetic resonance at 1.5 T. *Magnetic Resonance Materials in Physics, Biology and Medicine*, 25(3):223–231, 2012. (page 2, 7, 9, 10, 11, 24, 30, 32, 34, 36, 42, 43, 46, 51, 70, 74)

[19] R. W. Brown, Y. C. N. Cheng, E. M. Haacke, M. R. Thompson, and R. Venkatesan. *Magnetic Resonance Imaging: Physical Principles and Sequence Design: Second Edition*. Wiley Blackwell, 2014. (page 6)

[20] F. Noack. NMR field-cycling spectroscopy: principles and applications. *Progress in Nuclear Magnetic Resonance Spectroscopy*, 18(3):171–276, jan 1986, https://www.sciencedirect.com/science/article/pii/0079656586800048. (page 6)

[21] R. Kimmich and E. Anoardo. Field-cycling NMR relaxometry. *Progress in Nuclear Magnetic Resonance Spectroscopy*, 44(3-4):257–320, jul 2004, https://www.sciencedirect.com/science/article/pii/S0079656504000196. (page 7)

[22] D. Kruk, A. Herrmann, and E. Rössler. Field-cycling NMR relaxometry of viscous liquids and polymers. *Progress in Nuclear Magnetic Resonance Spectroscopy*, 63:33–64, may 2012, https://www.sciencedirect.com/science/article/pii/S0079656511000586. (page)

[23] F. Barberon, J. P. Korb, D. Petit, V. Morin, and E. Bermejo. Probing the Surface Area of a Cement-Based Material by Nuclear Magnetic Relaxation Dispersion. *Physical Review Letters*, 90(11):4, 2003. (page)

[24] R. M. Steele, J. P. Korb, G. Ferrante, and S. Bubici. New applications and perspectives of fast field cycling NMR relaxometry. *Magnetic Resonance in Chemistry*, 54(6):502–509, 2016. (page 7)

[25] Y. Wang, H. Cooperman, V. Rao, M. Nino-Murcia, S. Koenig, and R. Brown. A nuclear magnetic relaxation dispersion profile of normal breast and tumor tissues. *Magnetic Resonance Imaging*, 2(3):235, jan 1984, https://www.sciencedirect.com/science/article/pii/0730725X84900110. (page 7)

[26] S. H. Koenig and R. D. Brown. Field-cycling relaxometry of protein solutions and tissue: Implications for MRI. *Progress in Nuclear Magnetic Resonance Spectroscopy*, 22(6):487–567, jan 1990, https://www.sciencedirect.com/science/article/pii/0079656590800086. (page)

[27] E. Rössler, C. Mattea, and S. Stapf. Feasibility of high-resolution one-dimensional relaxation imaging at low magnetic field using a single-sided NMR scanner applied to articular cartilage. *Journal of Magnetic Resonance*, 251:43–51, feb 2015, https://www.sciencedirect.com/science/article/pii/S1090780714002948. (page 7)

[28] D. J. Lurie, S. Aime, S. Baroni, N. A. Booth, L. M. Broche, C. H. Choi, G. R. Davies, S. Ismail, D. O'Hógáin, and K. J. Pine. Fast Field-Cycling Magnetic Resonance Imaging. *Comptes Rendus Physique*, 11(2):136–148, 2010. (page 7, 8, 20, 30, 46, 62)

[29] C. T. Harris, W. B. Handler, Y. Araya, F. Martínez-Santiesteban, J. K. Alford, B. Dalrymple, F. Van Sas, B. A. Chronik, and T. J. Scholl. Development and optimization of hardware for delta relaxation enhanced MRI. *Magnetic Resonance in Medicine*, 72(4):1182–1190, oct 2014, http://doi.wiley.com/10.1002/mrm.25014. (page 9, 10, 11, 14, 18, 19, 30, 32, 33, 37, 74, 76)

[30] L. de Rochefort, E. Lee, M. Polello, L. Durrasse, G. Ferrante, and B. K. Rutt. Characterization and Compensation of Eddy Current Induced by Insertable dreMR Magnet. In *Proc. Intl. Soc. Mag. Reson. Med. 20*, 2012. (page 9, 10, 11, 14, 26, 33, 74)

[31] M. Bödenler, M. Basini, M. F. Casula, E. Umut, C. Gösweiner, A. Petrovic, D. Kruk, and H. Scharfetter. R1 dispersion contrast at high field with fast field-cycling MRI. *Journal of Magnetic Resonance*, 290:68–75, 2018. (page 7, 9, 10, 11, 12, 13, 14, 18, 19, 20, 24, 26, 49, 57, 70)

[32] G. FERRANTE and S. SYKORA. TECHNICAL ASPECTS OF FAST FIELD CYCLING. *Advances in Inorganic Chemistry*, 57:405–470, 2005. (page 8)

[33] M. Espy, A. Matlashov, and P. Volegov. SQUID-detected ultra-low field MRI. *Journal of Magnetic Resonance*, 229:127–141, apr 2013, `https://www.sciencedirect.com/science/article/pii/S1090780713000499?via{%}3Dihub`. (page 8)

[34] D. J. Lurie, M. A. Foster, D. Yeung, and J. M. S. Hutchison. Design, construction and use of a large-sample field-cycled PEDRI imager. *Physics in Medicine & Biology*, 43(7):1877, 1998, `http://stacks.iop.org/0031-9155/43/i=7/a=008`. (page 8, 9, 28)

[35] P. J. Ross, L. M. Broche, G. R. Davies, and D. J. Lurie. A new human-scale fast field-cycling MRI system for clinical applications. In *Proc. Intl. Soc. Mag. Reson. Med. 25*, 2017. (page 9, 12, 26, 28, 37)

[36] K. J. Pine, F. Goldie, and D. J. Lurie. In vivo field-cycling relaxometry using an insert coil for magnetic field offset. *Magnetic Resonance in Medicine*, 72(5):1492–1497, 2014. (page 9, 11)

[37] L. M. Broche, P. James Ross, K. J. Pine, and D. J. Lurie. Rapid multi-field T1 estimation algorithm for Fast Field-Cycling MRI. *Journal of Magnetic Resonance*, 238:44–51, jan 2014, `https://www.sciencedirect.com/science/article/pii/S1090780713002656?via{%}3Dihub`. (page 8, 20)

[38] J. K. Alford, T. J. Scholl, W. B. Handler, and B. A. Chronik. Design and construction of a prototype high-power B0 insert coil for field-cycled imaging in superconducting MRI systems. *Concepts in Magnetic Resonance Part B: Magnetic Resonance Engineering*, 35B(1):1–10, 2009, `https://onlinelibrary.wiley.com/doi/abs/10.1002/cmr.b.20132`. (page 10, 32)

[39] C. T. Harris, J. K. Alford, W. B. Handler, T. J. Scholl, and B. A. Chronik. Bo coil designs for in vivo delta relaxation enhanced MR in humans. In *Proc. Intl. Soc. Mag. Reson. Med. 18*, 2010. (page 11, 37)

[40] C. T. Harris, W. B. Handler, T. J. Scholl, and B. A. Chronik. A practical insert design for dreMR imaging in the human head. In *Proc. Intl. Soc. Mag. Reson. Med. 19*, 2011. (page 11, 37)

[41] L. M. Broche, P. J. Ross, G. R. Davies, and D. J. Lurie. Simple algorithm for the correction of MRI image artefacts due to random phase fluctuations. *Magnetic Resonance Imaging*, 44:55–59, 2017, https://doi.org/10.1016/j.mri.2017.07.023. (page 13, 14, 32, 37, 76)

[42] D. Hoult and R. Richards. The signal-to-noise ratio of the nuclear magnetic resonance experiment. *Journal of Magnetic Resonance*, 213(2):329–343, dec 2011, https://www.sciencedirect.com/science/article/pii/S1090780711003302. (page 15)

[43] G. Guillot, L. Jourdain, N. Chanet, R.-M. Dubuisson, M. Poirier-Quinot, and L. de Rochefort. R1, R2 and B1 mapping with an inhomogeneous T/R coil by QuICS. *Magnetic Resonance Materials in Physics, Biology and Medicine*, 30(Suppl 1):316, 2017, https://doi.org/10.1007/s10334-017-0633-0. (page 16, 17)

[44] D. J. Larkman and R. G. Nunes. Parallel magnetic resonance imaging. *Physics in Medicine and Biology*, 52(7):R15–55, 2007. (page 17)

[45] U. C. Hoelscher and P. M. Jakob. Eddy current compensation for delta relaxation enhanced MR by dynamic reference phase modulation. *Magnetic Resonance Materials in Physics, Biology and Medicine*, 26(2):249–259, 2013. (page 18, 30, 33, 38, 58, 74, 76)

[46] P. J. Ross, L. M. Broche, and D. J. Lurie. Rapid field-cycling MRI using fast spin-echo. *Magnetic Resonance in Medicine*, 73(3):1120–1124, 2015. (page 20, 32, 76)

[47] Y. T. Araya, F. Martínez-Santiesteban, W. B. Handler, C. T. Harris, B. A. Chronik, and T. J. Scholl. Nuclear magnetic relaxation dispersion of murine tissue for development of T ₁ (R ₁) dispersion contrast imaging. *NMR in Biomedicine*, 30(12):e3789, dec 2017, http://doi.wiley.com/10.1002/nbm.3789. (page 20, 24, 30, 51, 70, 71, 76)

[48] J. Hennig, A. Nauerth, and H. Friedburg. RARE imaging: A fast imaging method for clinical MR. *Magnetic Resonance in Medicine*, 3:823–833, jun 1986, https://doi.org/10.1002/mrm.1910030602. (page 20)

[49] A. Haase, J. Frahm, D. Matthaei, W. Hanicke, and K.-D. Merboldt. FLASH imaging. Rapid NMR imaging using low flip-angle pulses. *Journal of Magnetic Resonance (1969)*, 67(2):258–266, apr 1986, https://www.sciencedirect.com/science/article/pii/0022236486904336?via{%}3Dihub. (page 21)

[50] D. C. Look and D. R. Locker. Time Saving in Measurement of NMR and EPR Relaxation Times. *Review of Scientific Instruments*, 41(2):250–251, feb 1970, https://doi.org/10.1063/1.1684482. (page 21)

[51] G. Brix, L. R. Schad, M. Deimling, and W. J. Lorenz. Fast and precise T1 imaging using a TOMROP sequence. *Magnetic Resonance Imaging*, 8(4):351–356, jan 1990, https://www.sciencedirect.com/science/article/pii/0730725X9090041Y?via{%}3Dihub. (page 21)

[52] N. Chanet and L. de Rochefort. Contrast optimization using Fast Field Cycling techniques and fast low angle sequences. In *Proc. Intl. Soc. Mag. Reson. Med. 24*, 2016. (page 21)

[53] N. Chanet, G. Guillot, and L. de Rochefort. Measurement of R2 dispersion profiles using Fast Field Cycling MRI. In *Proc. Intl. Soc. Mag. Reson. Med. 25*, 2017. (page 22)

[54] J. Vymazal, R. A. Brooks, O. Zak, C. Mcrill, C. Shen, and D. G. Chiro. T1 and t2 of ferritin at different field strengths: effect on mri. *Magnetic Resonance in Medicine*, 27(2):368–374, jun 1992, https://doi.org/10.1002/mrm.1910270218. (page 22)

[55] R. Kimmich, W. Nusser, and F. Winter. In vivo NMR field-cycling relaxation spectroscopy reveals 14 N 1 H relaxation sinks in the backbones of proteins. *Physics in Medicine & Biology*, 29(5):593, 1984, http://stacks.iop.org/0031-9155/29/i=5/a=011. (page 22)

[56] P. H. Fries and E. Belorizky. Simple expressions of the nuclear relaxation rate enhancement due to quadrupole nuclei in slowly tumbling molecules. *The Journal of Chemical Physics*, 143(4):44202, jul 2015, https://doi.org/10.1063/1.4926827. (page 23)

[57] X. Jiao and R. G. Bryant. Noninvasive measurement of protein concentration. *Magnetic Resonance in Medicine*, 35:159–161, jun 1996, https://doi.org/10.1002/mrm.1910350205. (page 23)

[58] K. J. Pine, G. R. Davies, and D. J. Lurie. Field-cycling NMR relaxometry with spatial selection. *Magnetic Resonance in Medicine*, 63(6):1698–1702, 2010. (page 23, 28)

[59] E. Rössler, C. Mattea, and S. Stapf. NMR dispersion investigations of enzymatically degraded bovine articular cartilage. *Magnetic Resonance in Medicine*, 73(5):2005–2014, may 2014, https://doi.org/10.1002/mrm.25292. (page 23)

[60] S. Aime, M. Botta, D. Esteban-Gómez, and C. Platas-Iglesias. Characterisation of magnetic resonance imaging (MRI) contrast agents using NMR relaxometry.

Molecular Physics, 117:898–909, 2018, https://www.tandfonline.com/doi/full/10.1080/00268976.2018.1516898. (page 23, 25, 46, 63)

[61] J. R. Morrow and É. Tóth. Next-Generation Magnetic Resonance Imaging Contrast Agents. *Inorganic Chemistry*, 56(11):6029–6034, 2017. (page)

[62] M. W. Rotz, K. S. Culver, G. Parigi, K. W. Macrenaris, C. Luchinat, T. W. Odom, and T. J. Meade. High relaxivity Gd(III)-DNA gold nanostars: Investigation of shape effects on proton relaxation. *ACS Nano*, 9(3):3385–3396, 2015. (page 23)

[63] D. Ó Hógáin, G. R. Davies, S. Baroni, S. Aime, and D. J. Lurie. The use of contrast agents with fast field-cycling magnetic resonance imaging. *Physics in Medicine and Biology*, 56(1):105–115, 2011. (page 23, 32, 35)

[64] P. A. Bottomley, T. H. Foster, R. E. Argersinger, and L. M. Pfeifer. A review of normal tissue hydrogen NMR relaxation times and relaxation mechanisms from 1-100 MHz: Dependence on tissue type, NMR frequency, temperature, species, excision, and age. *Medical Physics*, 11(4):425–448, jun 1984, https://doi.org/10.1118/1.595535. (page 23)

[65] S. F. Akber. NMR relaxation data of water proton in normal tissues. *Physiological chemistry and physics and medical NMR*, 28:205–238, 1996. (page 23)

[66] G. Diakova, J. Korb, and R. G. Bryant. The magnetic field dependence of water T1 in tissues. *Magnetic Resonance in Medicine*, 68(1):272–277, 2012, http:https://doi.org/10.1002/mrm.23229. (page 23)

[67] Z. Zhou and Z.-R. Lu. Gadolinium-based contrast agents for magnetic resonance cancer imaging. *Wiley Interdisciplinary Reviews: Nanomedicine and Nanobiotechnology*, 5(1):1–18, 2013, http://doi.wiley.com/10.1002/wnan.1198. (page 24)

[68] P. Caravan, N. J. Cloutier, M. T. Greenfield, S. A. McDermid, S. U. Dunham, J. W. M. Bulte, Amedio John C., R. J. Looby, R. M. Supkowski, Horrocks William DeW., T. J. McMurry, and R. B. Lauffer. The Interaction of MS-325 with Human Serum Albumin and Its Effect on Proton Relaxation Rates. *Journal of the American Chemical Society*, 124(12):3152–3162, mar 2002, https://doi.org/10.1021/ja017168k. (page 24)

[69] D. Bell and M. Morgan. Gadofosveset trisodium, 2018, https://radiopaedia.org/articles/gadofosveset-trisodium-1. (page 25)

[70] G. B. Toth, C. G. Varallyay, A. Horvath, M. R. Bashir, P. L. Choyke, H. E. Daldrup-Link, E. Dosa, J. P. Finn, S. Gahramanov, M. Harisinghani, I. Macdougall, A. Neuwelt, S. S. Vasanawala, P. Ambady, R. Barajas, J. S. Cetas, J. Ciporen, T. J.

DeLoughery, N. D. Doolittle, R. Fu, J. Grinstead, A. R. Guimaraes, B. E. Hamilton, X. Li, H. L. McConnell, L. L. Muldoon, G. Nesbit, J. P. Netto, D. Petterson, W. D. Rooney, D. Schwartz, L. Szidonya, and E. A. Neuwelt. Current and potential imaging applications of ferumoxytol for magnetic resonance imaging. *Kidney International*, 92(1):47–66, jul 2017, https://www.sciencedirect.com/science/article/abs/pii/S0085253817301199. (page 25)

[71] S. S. Vasanawala, K. Nguyen, M. D. Hope, M. D. Bridges, T. A. Hope, S. B. Reeder, and M. R. Bashir. Safety and technique of ferumoxytol administration for MRI. *Magnetic Resonance in Medicine*, 75(5):2107–2111, 2016, http:https://doi.org/10.1002/mrm.26151. (page 25)

[72] D. Kruk, A. Kubica, W. Masierak, A. F. Privalov, M. Wojciechowski, and W. Medycki. Quadrupole relaxation enhancement - application to molecular crystals. *Solid State Nuclear Magnetic Resonance*, 40(3):114–120, oct 2011, http://linkinghub.elsevier.com/retrieve/pii/S0926204011000816. (page 25, 30, 31, 67, 68, 69)

[73] D. Kruk, E. Umut, E. Masiewicz, C. Sampl, R. Fischer, S. Spirk, C. Goesweiner, and H. Scharfetter. 209Bi quadrupole relaxation enhancement in solids as a step towards new contrast mechanisms in magnetic resonance imaging. *Physical Chemistry Chemical Physics*, 20(18):12710–12718, 2018, http://dx.doi.org/10.1039/C8CP00993G. (page 25, 69)

[74] R. Kubo. Stochastic Liouville Equations. *Journal of Mathematical Physics*, 4(2):174–183, feb 1963, https://doi.org/10.1063/1.1703941. (page 25, 68)

[75] P.-O. Westlund and H. Wennerstrom. Spin-lattice relaxation of a Spin-12 nucleus coupled to a quadrupolar spin-1 nucleus. The quadrupolar dip. *Journal of Magnetic Resonance (1969)*, 63(2):280–286, jun 1985, https://www.sciencedirect.com/science/article/pii/0022236485903178. (page 25, 68)

[76] C. Gösweiner, P. Lantto, R. Fischer, C. Sampl, E. Umut, P.-O. Westlund, D. Kruk, M. Bödenler, S. Spirk, A. Petrovic, and H. Scharfetter. Tuning Nuclear Quadrupole Resonance : A Novel Approach for the Design of Frequency-Selective MRI Contrast Agents. *Phys. Rev. X*, 8(2):021076, 2018, https://link.aps.org/doi/10.1103/PhysRevX.8.021076. (page 26, 67, 69, 71)

[77] N. Chanet, G. Guillot, I. Leguerney, R.-M. Dubuisson, C. Sebrié, A. Ingels, N. Assoun, E. Daudigeos-Dubus, B. Geoerger, N. Lassau, L. Broche, and L. de Rochefort. In vivo measurements of T1-dispersion maps in a kidney tumor mouse model using FFC-MRI around 1.5 T. In *Proc. Intl. Soc. Mag. Reson. Med. 26*, 2018. (page 27, 74, 76)

[78] E. Lee, L. de Rochefort, G. Ferrante, and B. K. Rutt. Next generation delta relaxation enhanced MRI with 0.36T ΔB. *20th Annual Meeting of ISMRM*, 20:8081, 2012. (page 30, 70, 74)

[79] C. Gösweiner, D. Kruk, P.-O. Westlund, R. Fischer, M. Schlögl, M. Bödenler, A. Petrovic, S. Spirk, and H. Scharfetter. Extrinsic MRI Contrast Agents Based on Nuclear Quadrupole Enhanced Relaxation: Principle, Requirements and Characterization of Promising Compounds. In *Proc. Intl. Soc. Mag. Reson. Med. 25*, 2017. (page 30)

[80] G. Voigt and R. Kimmich. Quadrupolar dip in proton relaxation dispersion of poly(vinyl chloride). *Journal of Magnetic Resonance (1969)*, 1976. (page 30)

[81] F. Winter and R. Kimmich. Spin lattice relaxation of dipole nuclei (I= 1/2) coupled to quadrupole nuclei (S=1). *Molecular Physics*, 1982. (page 30)

[82] S. E. Ungersma, N. I. Matter, J. W. Hardy, R. D. Venook, A. Macovski, S. M. Conolly, and G. C. Scott. Magnetic resonance imaging with T1 dispersion contrast. *Magnetic Resonance in Medicine*, 55(6):1362–71, 2006, `http://www.ncbi.nlm.nih.gov/pubmed/16673360`. (page 30, 35, 62)

[83] P.-O. Westlund. The quadrupole enhanced 1H spin-lattice relaxation of the amide proton in slow tumbling proteins. *Physical Chemistry Chemical Physics*, 12(13):3136, 2010, `http://xlink.rsc.org/?DOI=b922817a`. (page 30)

[84] M. Basini, T. Orlando, P. Arosio, M. F. Casula, D. Espa, S. Murgia, C. Sangregorio, C. Innocenti, and A. Lascialfari. Local spin dynamics of iron oxide magnetic nanoparticles dispersed in different solvents with variable size and shape: A (1)H NMR study. *The Journal of chemical physics*, 146(3):34703, 2017, `http://aip.scitation.org/doi/10.1063/1.4973979{%}0Ahttp://www.ncbi.nlm.nih.gov/pubmed/28109242`. (page 34, 41, 43)

[85] M. A. Bernstein, K. F. King, and X. J. Zhou. Handbook of MRI Pulse Sequences. In *Handbook of MRI Pulse Sequences*, chapter 14.2, pages 606–630. 2004. (page 35)

[86] V. Zampetoulas, L. M. Broche, G. I. Murray, and D. J. Lurie. The T1-Dispersion Curve as a Biomarker of Colorectal Cancer. In *Proc. Intl. Soc. Mag. Reson. Med. 25*, 2017. (page 37)

[87] M. Rohrer, H. Bauer, J. Mintorovitch, M. Requardt, and H. J. Weinmann. Comparison of magnetic properties of MRI contrast media solutions at different magnetic field strengths. *Investigative Radiology*, 2005. (page 38, 49)

[88] U. C. Hoelscher, S. Lother, F. Fidler, M. Blaimer, and P. Jakob. Unambiguous Localization of Contrast Agents via B0 -Field-Cycling. In *Proc. Intl. Soc. Mag. Reson. Med. 18*, 2010. (page 42)

[89] M. Ramalho, V. Herédia, M. Tsurusaki, E. Altun, and R. C. Semelka. Quantitative and qualitative comparison of 1.5 and 3.0 tesla MRI in patients with chronic liver diseases. *Journal of Magnetic Resonance Imaging*, 29(4):869–879, 2009. (page 43)

[90] V. C. Pierre, S. M. Harris, and S. L. Pailloux. Comparing Strategies in the Design of Responsive Contrast Agents for Magnetic Resonance Imaging: A Case Study with Copper and Zinc. *Accounts of Chemical Research*, 51(2):342–351, 2018. (page 46, 47, 65, 74)

[91] C. S. Bonnet and É. Tóth. Molecular Magnetic Resonance Imaging Probes Based on Ln3Â + Complexes. *Advances in Inorganic Chemistry*, 68:43–96, jan 2016, `https://www.sciencedirect.com/science/article/pii/S0898883815000161`. (page 46, 65)

[92] M. Bödenler, L. de Rochefort, P. J. Ross, N. Chanet, G. Guillot, G. R. Davies, C. Gösweiner, H. Scharfetter, D. J. Lurie, and L. M. Broche. Comparison of fast field-cycling magnetic resonance imaging methods and future perspectives. *Molecular Physics*, 117(7-8):832–848, apr 2019, `https://doi.org/10.1080/00268976.2018.1557349`. (page 46, 51)

[93] J. K. Alford, C. T. Farrar, Y. Yang, W. B. Handler, B. A. Chronik, T. J. Scholl, G. Madan, and P. Caravan. Direct albumin imaging in mouse tumour model. In *Proc Intl Soc Mag Reson Med 19*, 2011. (page 46, 51)

[94] J. K. Alford, A. G. Sorensen, T. Brenner, B. A. Chronik, W. B. Handler, T. J. Scholl, G. Madan, and P. Caravan. Direct protein imaging of inflammation in the human hand. In *Proc Intl Soc Mag Reson Med 19*, 2011. (page 46, 51)

[95] W. Maret. Zinc Biochemistry: From a Single Zinc Enzyme to a Key Element of Life. *Advances in Nutrition*, 4(1):82–91, jan 2013, `http://dx.doi.org/10.3945/an.112.003038`. (page 47)

[96] N. Wijesekara, F. Chimienti, and M. B. Wheeler. Zinc, a regulator of islet function and glucose homeostasis. *Diabetes, Obesity and Metabolism*, 11(s4):202–214, oct 2009, `https://doi.org/10.1111/j.1463-1326.2009.01110.x`. (page 47)

[97] C. Hogstrand, P. Kille, R. Nicholson, and K. Taylor. Zinc transporters and cancer: a potential role for ZIP7 as a hub for tyrosine kinase activation. *Trends in Molecular Medicine*, 15(3):101–111, mar 2009, `https://www.sciencedirect.com/science/article/pii/S1471491409000355?via{%}3Dihub`. (page 47)

[98] G. Lyubartseva, J. L. Smith, W. R. Markesbery, and M. A. Lovell. Alterations of Zinc Transporter Proteins ZnT-1, ZnT-4 and ZnT-6 in Preclinical Alzheimer's Disease Brain. *Brain Pathology*, 20(2):343–350, feb 2010, `https://doi.org/10.1111/j.1750-3639.2009.00283.x`. (page 47)

[99] C. S. Bonnet. Zn2+detection by MRI using Ln3+-based complexes: The central role of coordination chemistry. *Coordination Chemistry Reviews*, 369:91–104, 2018. (page 47, 65)

[100] S. Aime, M. Botta, M. Fasano, S. G. Crich, and E. Terreno. Gd(III) complexes as contrast agents for magnetic resonance imaging: a proton relaxation enhancement study of the interaction with human serum albumin. *JBIC Journal of Biological Inorganic Chemistry*, 1(4):312–319, 1996, https://doi.org/10.1007/s007750050059. (page 47)

[101] C. S. Bonnet, F. Buron, F. Caillé, C. M. Shade, B. Drahoš, L. Pellegatti, J. Zhang, S. Villette, L. Helm, C. Pichon, F. Suzenet, S. Petoud, and É. Tóth. Pyridine-Based Lanthanide Complexes Combining MRI and NIR Luminescence Activities. *Chemistry - A European Journal*, 18(5):1419–1431, 2012, https://doi.org/10.1002/chem.201102310. (page 48)

[102] J. K. Romary, J. D. Barger, and J. E. Bunds. New multidentate .alpha.-pyridyl ligand. Coordination of bis(2-pyridylmethyl)amine with transition metal ions. *Inorganic Chemistry*, 7(6):1142–1145, jun 1968, https://doi.org/10.1021/ic50064a018. (page 48)

[103] K. Hanaoka, K. Kikuchi, Y. Urano, and T. Nagano. Selective sensing of zinc ions with a novel magnetic resonance imaging contrast agent. *Journal of the Chemical Society, Perkin Transactions 2*, (9):1840–1843, 2001, http://dx.doi.org/10.1039/B100994J. (page 48)

[104] C. Rivas, G. J. Stasiuk, M. Sae-Heng, and N. J. Long. Towards understanding the design of dual-modal MR/fluorescent probes to sense zinc ions. *Dalton Transactions*, 44(11):4976–4985, 2015, http://dx.doi.org/10.1039/C4DT02981J. (page)

[105] A. C. Esqueda, J. A. Lo, G. Andreu-de riquer, J. Ratnakar, A. J. M. Lubag, A. D. Sherry, and L. M. D. Leo. A New Gadolinium-Based MRI Zinc Sensor. *J. Am. Chem. Soc.*, 131(12):11387, 2009. (page 51)

[106] J. Yu, A. F. Martins, C. Preihs, V. Clavijo Jordan, S. Chirayil, P. Zhao, Y. Wu, K. Nasr, G. E. Kiefer, and A. D. Sherry. Amplifying the Sensitivity of Zinc(II) Responsive MRI Contrast Agents by Altering Water Exchange Rates. *Journal of the American Chemical Society*, 137(44):14173–14179, 2015. (page 48, 50)

[107] L. M. Matosziuk, J. H. Leibowitz, M. C. Heffern, K. W. MacRenaris, M. A. Ratner, and T. J. Meade. Structural Optimization of Zn(II)-Activated Magnetic Resonance Imaging Probes. *Inorganic Chemistry*, 52(21):12250–12261, nov 2013, https://doi.org/10.1021/ic400681j. (page 50)

[108] M. Regueiro-Figueroa, S. Gündüz, V. Patinec, N. K. Logothetis, D. Esteban-Gómez, R. Tripier, G. Angelovski, and C. Platas-Iglesias. Gd3+-Based Magnetic Resonance Imaging Contrast Agent Responsive to Zn2+. *Inorganic Chemistry*, 54(21):10342–10350, nov 2015, https://doi.org/10.1021/acs.inorgchem.5b01719. (page 50)

[109] A. J. M. Lubag, L. M. De Leon-Rodriguez, S. C. Burgess, and A. D. Sherry. Noninvasive MRI of β-cell function using a Zn²⁺-responsive contrast agent. *Proceedings of the National Academy of Sciences*, 108(45):18400 LP – 18405, nov 2011, http://www.pnas.org/content/108/45/18400.abstract. (page 50)

[110] M. V. Clavijo Jordan, S.-T. Lo, S. Chen, C. Preihs, S. Chirayil, S. Zhang, P. Kapur, W.-H. Li, L. M. De Leon-Rodriguez, A. J. M. Lubag, N. M. Rofsky, and A. D. Sherry. Zinc-sensitive MRI contrast agent detects differential release of Zn(II) ions from the healthy vs. malignant mouse prostate. *Proceedings of the National Academy of Sciences*, 113(37):E5464 LP – E5471, sep 2016, http://www.pnas.org/content/113/37/E5464.abstract. (page 50)

[111] A. F. Martins, V. Clavijo Jordan, F. Bochner, S. Chirayil, N. Paranawithana, S. Zhang, S.-T. Lo, X. Wen, P. Zhao, M. Neeman, and A. D. Sherry. Imaging Insulin Secretion from Mouse Pancreas by MRI Is Improved by Use of a Zinc-Responsive MRI Sensor with Lower Affinity for Zn2+ Ions. *Journal of the American Chemical Society*, 140(50):17456–17464, dec 2018, https://doi.org/10.1021/jacs.8b07607. (page 50)

[112] K. P. Malikidogo, I. Da Silva, J.-F. Morfin, S. Lacerda, L. Barantin, T. Sauvage, J. Sobilo, S. Lerondel, É. Tóth, and C. S. Bonnet. A cocktail of 165Er(iii) and Gd(iii) complexes for quantitative detection of zinc using SPECT and MRI. *Chemical Communications*, 54(55):7597–7600, 2018, http://dx.doi.org/10.1039/C8CC03407A. (page 50)

[113] L. De Leon-Rodriguez, A. J. M. Lubag Jr, and A. D. Sherry. Imaging free zinc levels in vivo - what can be learned? *Inorganica chimica acta*, 393:12–23, dec 2012, https://www.ncbi.nlm.nih.gov/pubmed/23180883https://www.ncbi.nlm.nih.gov/pmc/PMC3501686/. (page 51)

[114] C. Gösweiner, D. Kruk, E. Umut, E. Masiewicz, M. Bödenler, and H. Scharfetter. Predicting quadrupole relaxation enhancement peaks in proton R1-NMRD profiles in solid Bi-aryl compounds from NQR parameters. *Molecular Physics*, 117(7-8):910–920, apr 2019, https://doi.org/10.1080/00268976.2018.1519201. (page)

[115] L. M. De León-Rodríguez, A. F. Martins, M. C. Pinho, N. M. Rofsky, and A. D. Sherry. Basic MR relaxation mechanisms and contrast agent design. *Journal of Magnetic Resonance Imaging*, 42(3):545–565, 2015, https://onlinelibrary.wiley.com/doi/abs/10.1002/jmri.24787. (page 63, 66)

[116] J. Kowalewski and D. Kruk. *Paramagnetic Relaxation in Solution.* American Cancer Society, 2011, https://onlinelibrary.wiley.com/doi/abs/10.1002/9780470034590.emrstm0375.pub2. (page 63)

[117] E. Belorizky, P. H. Fries, L. Helm, J. Kowalewski, D. Kruk, R. R. Sharp, and P.-O. Westlund. Comparison of different methods for calculating the paramagnetic relaxation enhancement of nuclear spins as a function of the magnetic field. *The Journal of Chemical Physics*, 128(5):52315, 2008, https://doi.org/10.1063/1.2833957. (page 64)

[118] C. Henoumont, L. Vander Elst, R. N. Muller, and S. Laurent. Chapter 17 Paramagnetic Complexes and Superparamagnetic Systems. In *Field-cycling NMR Relaxometry: Instrumentation{,} Model Theories and Applications*, pages 427–447. The Royal Society of Chemistry, 2019, http://dx.doi.org/10.1039/9781788012966-00427. (page 65, 66)

[119] X. Zhou, P. Caravan, R. B. Clarkson, and P. O. Westlund. On the philosophy of optimizing contrast agents. An analysis of1H NMRD profiles and ESR lineshapes of the Gd(III)complex MS-325 + HSA. *Journal of Magnetic Resonance*, 167(1):147–160, 2004. (page)

[120] X. Zhou and P.-O. Westlund. 1H NMRD profiles and ESR lineshapes of Gd(III) complexes: a comparison between the generalized SBM and the stochastic Liouville approach. *Journal of Magnetic Resonance*, 173(1):75–83, mar 2005, https://www.sciencedirect.com/science/article/pii/S1090780704003556. (page 63)

[121] P. Caravan, C. T. Farrar, L. Frullano, and R. Uppal. Influence of molecular parameters and increasing magnetic field strength on relaxivity of gadolinium- and manganese-based T1 contrast agents. *Contrast Media & Molecular Imaging*, 4(2):89–100, 2009, https://onlinelibrary.wiley.com/doi/abs/10.1002/cmmi.267. (page 63)

[122] M. Botta. Second Coordination Sphere Water Molecules and Relaxivity of Gadolinium(III) Complexes: Implications for MRI Contrast Agents. *European Journal of Inorganic Chemistry*, 2000(3):399–407, mar 2000, https://doi.org/10.1002/(SICI)1099-0682(200003)2000:3{%}3C399::AID-EJIC399{%}3E3.0.COhttp://2-b. (page 63)

[123] L. Hwang and J. H. Freed. Dynamic effects of pair correlation functions on spin relaxation by translational diffusion in liquids. *The Journal of Chemical Physics*, 63(9):4017–4025, 1975, https://aip.scitation.org/doi/abs/10.1063/1.431841. (page 64)

[124] J. H. Freed. Dynamic effects of pair correlation functions on spin relaxation by translational diffusion in liquids. II. Finite jumps and independent T1 processes. *The*

Journal of Chemical Physics, 68(9):4034–4037, 1978, https://doi.org/10.1063/1.436302. (page 64, 66)

[125] I. Solomon. Relaxation Processes in a System of Two Spins. *Phys. Rev.*, 99(2):559–565, jul 1955, https://link.aps.org/doi/10.1103/PhysRev.99.559. (page 64)

[126] I. Solomon and N. Bloembergen. Nuclear Magnetic Interactions in the HF Molecule. *The Journal of Chemical Physics*, 25(2):261–266, 1956, https://doi.org/10.1063/1.1742867. (page)

[127] N. Bloembergen. Proton Relaxation Times in Paramagnetic Solutions. *The Journal of Chemical Physics*, 27(2):572–573, 1957, https://doi.org/10.1063/1.1743771. (page)

[128] N. Bloembergen and L. O. Morgan. Proton Relaxation Times in Paramagnetic Solutions. Effects of Electron Spin Relaxation. *The Journal of Chemical Physics*, 34(3):842–850, 1961, https://doi.org/10.1063/1.1731684. (page 64)

[129] E. Belorizky and P. H. Fries. Simple analytical approximation of the longitudinal electronic relaxation rate of Gd(iii) complexes in solutions. *Phys. Chem. Chem. Phys.*, 6(9):2341–2351, 2004, http://dx.doi.org/10.1039/B316249D. (page 64)

[130] E. L. Que and C. J. Chang. Responsive magnetic resonance imaging contrast agents as chemical sensors for metals in biology and medicine. *Chem. Soc. Rev.*, 39(1):51–60, 2010, http://dx.doi.org/10.1039/B914348N. (page 65)

[131] M. Bödenler, K. P. Malikidogo, J.-F. Morfin, C. S. Aigner, É. Tóth, C. S. Bonnet, and H. Scharfetter. High-Field Detection of Biomarkers with Fast Field-Cycling MRI: The Example of Zinc Sensing. *Chemistry - A European Journal*, 25(35):8236–8239, jun 2019, https://doi.org/10.1002/chem.201901157. (page 66)

[132] J. Dulińska-Litewka, A. Łazarczyk, P. Hałubiec, O. Szafrański, K. Karnas, and A. Karewicz. Superparamagnetic Iron Oxide Nanoparticles-Current and Prospective Medical Applications. *Materials*, 12(4), 2019, https://www.mdpi.com/1996-1944/12/4/617. (page 66)

[133] A. Roch, R. N. Muller, and P. Gillis. Theory of proton relaxation induced by superparamagnetic particles. *The Journal of Chemical Physics*, 110(11):5403–5411, 1999, https://doi.org/10.1063/1.478435. (page 66)

[134] G. Strijkers, W. M. Mulder, G. F. van Tilborg, and K. Nicolay. MRI Contrast Agents: Current Status and Future Perspectives. *Anti-Cancer Agents in Medicinal Chemistry*, 2008. (page 66)

[135] S. Laurent, D. Forge, M. Port, A. Roch, C. Robic, L. Vander Elst, and R. N. Muller. Magnetic Iron Oxide Nanoparticles: Synthesis, Stabilization, Vectorization, Physicochemical Characterizations, and Biological Applications. *Chemical Reviews*, 108(6):2064–2110, jun 2008, https://doi.org/10.1021/cr068445e. (page 66)

[136] G. G. Briand and N. Burford. Bismuth Compounds and Preparations with Biological or Medicinal Relevance. *Chemical Reviews*, 99(9):2601–2658, sep 1999, https://doi.org/10.1021/cr980425s. (page 69)

[137] Y. Fujiwara, M. Mitani, S. Yasuike, J. Kurita, and T. Kaji. An Organobismuth Compound that Exhibits Selective Cytotoxicity to Vascular Endothelial Cells in Vitro. *Journal of Health Science*, 51(3):333–340, 2005. (page 69)

[138] M. A. McGuigan. Chronic Poisoning: Trace Metals and Others. In *Goldman's Cecil Medicine*, pages 88–95. Elsevier, New York, 2012. (page 69)

[139] P. C. Naha, A. Al Zaki, E. Hecht, M. Chorny, P. Chhour, E. Blankemeyer, D. M. Yates, W. R. T. Witschey, H. I. Litt, A. Tsourkas, and D. P. Cormode. Dextran coated bismuth-iron oxide nanohybrid contrast agents for computed tomography and magnetic resonance imaging. *J. Mater. Chem. B*, 2(46):8239–8248, 2014, http://dx.doi.org/10.1039/C4TB01159G. (page 69)

[140] D. Kruk, E. Masiewicz, E. Umut, A. Petrovic, R. Kargl, and H. Scharfetter. Estimation of the magnitude of quadrupole relaxation enhancement in the context of magnetic resonance imaging contrast. *Journal of Chemical Physics*, 2019. (page xviii, 69, 70)

[141] H. Scharfetter, C. Gösweiner, E. Umut, C. Sampl, R. Fischer, S. Spirk, A. Petrovic, and D. Kruk. Quadrupolar relaxation enhancement in selected Bismuth-Aryl compounds: Promising precursors for novel T1 MRI contrast agents. In *Proc. Intl. Soc. Mag. Reson. Med. 26*, 2018. (page xviii, 69, 70)

[142] H. Scharfetter. Quadrupole enhanced proton relaxation: Proof of principle for a novel extrinsic MRI contrast mechanism. In *Abstracts of the EUROMAR 2018*, 2018. (page xviii, 69, 70)

[143] A. Akbarzadeh, R. Rezaei-Sadabady, S. Davaran, S. W. Joo, N. Zarghami, Y. Hanifehpour, M. Samiei, M. Kouhi, and K. Nejati-Koshki. Liposome: classification, preparation, and applications. *Nanoscale Research Letters*, 8(1):102, 2013, https://doi.org/10.1186/1556-276X-8-102. (page 71)

[144] A. Chemelli, M. Maurer, R. Geier, and O. Glatter. Optimized Loading and Sustained Release of Hydrophilic Proteins from Internally Nanostructured Particles. *Langmuir*, 28(49):16788–16797, dec 2012, https://doi.org/10.1021/la303373q. (page)

[145] A. Chemelli, B. Conde-Valentín, F. Uhlig, and O. Glatter. Amino Acid Induced Modification of Self-Assembled Monoglyceride-Based Nanostructures. *Langmuir*, 31(38):10377–10381, sep 2015, https://doi.org/10.1021/acs.langmuir.5b02139. (page 71)

[146] L. E. Cole, R. D. Ross, J. M. R. Tilley, T. Vargo-Gogola, and R. K. Roeder. Gold nanoparticles as contrast agents in x-ray imaging and computed tomography. *Nanomedicine*, 10(2):321–341, 2015, https://doi.org/10.2217/nnm.14.171. (page 71)

[147] M. R. Ruggiero, S. Baroni, S. Aime, and S. G. Crich. Relaxometric investigations addressing the determination of intracellular water lifetime: a novel tumour biomarker of general applicability. *Molecular Physics*, 117(7-8):968–974, 2019, https://doi.org/10.1080/00268976.2018.1527045. (page 75)

[148] E. Rössler, C. Mattea, S. Saarakkala, P. Lehenkari, M. Finnilä, L. Rieppo, S. Karhula, M. T. Nieminen, and S. Stapf. Correlations of low-field NMR and variable-field NMR parameters with osteoarthritis in human articular cartilage under load. *NMR in Biomedicine*, 30(8):e3738, 2017, https://onlinelibrary.wiley.com/doi/abs/10.1002/nbm.3738. (page)

[149] O. V. Petrov and S. Stapf. Multicomponent analysis of T1 relaxation in bovine articular cartilage at low magnetic fields. *Magnetic Resonance in Medicine*, 81(5):2858–2868, 2019, https://onlinelibrary.wiley.com/doi/abs/10.1002/mrm.27624. (page 75)

[150] S. M. Spann, K. S. Kazimierski, C. S. Aigner, M. Kraiger, K. Bredies, and R. Stollberger. Spatio-temporal TGV denoising for ASL perfusion imaging. *NeuroImage*, 157:81–96, aug 2017, https://www.sciencedirect.com/science/article/pii/S1053811917304536?via{%}3Dihub. (page 75)